

Skolkovo Institute of Science and Technology

UNRAVELING BULK AND INTERFACIAL DEGRADATION MECHANISMS IN  
PEROVSKITE SOLAR CELLS

*Doctoral Thesis*

by

ALEKSANDRA BOLDYREVA

DOCTORAL PROGRAM IN MATERIALS SCIENCE AND ENGINEERING

Supervisor

Professor Pavel Troshin

Moscow - 2020

© Aleksandra Boldyreva 2020

I hereby declare that the work presented in this thesis was carried out by myself at Skolkovo Institute of Science and Technology, Moscow, except where due acknowledgment is made and has not been submitted for any other degree.

Candidate (Aleksandra Boldyreva)

Supervisor (Pavel Troshin)

## Abstract

Solar cells based on complex lead halides with the perovskite structure have attracted particular attention of material scientists and engineers all over the world. It is believed that perovskite solar cells (PSCs) can replace more expensive and complex Si-based solar cells on a market. However, the main obstacle on the way to successful perovskite solar cell commercialization is the poor stability of complex lead halides. There are many factors that influence perovskite solar cell operation stability. Among them, the degradation occurring at the interfaces between adjacent functional layers and in the bulk of perovskite material.

At the first stage of the performed study, we focused on exploring the interfacial degradation pathways induced at the interfaces between the methylammonium lead iodide ( $\text{MAPbI}_3$ ) and the commonly used charge transport layer (CTL) materials. Importantly, we explored two principally different sample geometries and showed that placing CTL as substrate under the perovskite films induced completely different interfacial chemistry as compared to the samples when CTL is deposited atop the  $\text{MAPbI}_3$  films as encapsulating coating. We have shown that any specific interactions between the CTL and perovskite decomposition products strongly accelerate the light-induced aging effects.

At the second stage of the work, we performed a systematic study of a series of four commonly used hole-transport layer materials (HTLs) in combination with five different lead halide perovskite absorbers. We demonstrated that the interfacial degradation effects depend not only on the composition and properties of the HTL materials but are also largely affected by the perovskite formulation. Surprisingly, the most simple perovskite structures such as  $\text{MAPbI}_3$  and  $\text{Cs}_{0.15}\text{FA}_{0.85}\text{PbI}_3$  showed superior photostability if properly encapsulated.

At the final stage of this work, while having identified stable interfaces between the lead halide absorbers and the charge transport layers, we explored the potential of space applications for PSCs. While analyzing the radiation stability of different

perovskite films we revealed several new degradation pathways, particularly, the unusual halide phase segregation induced by gamma rays. Among all explored perovskite absorbers the MAPbI<sub>3</sub> formulation showed the best radiation stability, which makes a good parallel with the results of the light-induced stability tests. Using the most stable absorber materials and charge transport layers we demonstrated impressive radiation stability of PSCs featuring their potential for space applications.

To summarize, we performed a systematic study starting from individual thin films and going all the way to completed devices and analysis of their radiation stability. This study shed light for the first time on numerous interfacial degradation pathways, leading to operation failure in PSCs. The most stable material combinations were identified and potential for further stability improvement was outlined, thus paving a way to design efficient and stable perovskite photovoltaics.

## Publications

1. **A. G. Boldyreva**, A. F. Akbulatov, M. Elnaggar, S. Yu Luchkin, A. V. Danilov, I. S. Zhidkov, O. R. Yamilova, Yu S. Fedotov, S. I. Bredikhin, E. Z. Kurmaev, K. J. Stevenson and P. A. Troshin "Impact of charge transport layers on the photochemical stability of MAPbI<sub>3</sub> in thin films and perovskite solar cells" *Sustain. Energy Fuels*, **2019**, 3, 2705-2716. <https://doi.org/10.1039/C9SE00493A>
2. **A. G Boldyreva**, I. S. Zhidkov, S. Tsarev, A. F. Akbulatov, M. M. Tepliakova, Y. S. Fedotov, S. I. Bredikhin, E. Yu. Postnova, S. Yu. Luchkin, E. Z. Kurmaev, K. J. Stevenson and P. A. Troshin "Unraveling the impact of hole-transport materials on photostability of perovskite films and p-i-n solar cells" *ACS Appl. Mater. Interfaces* **2020**, 12, 16, 19161–19173. <https://doi.org/10.1021/acsami.0c01027>
3. **A.G. Boldyreva**, A.F. Akbulatov, S.A. Tsarev, S.Yu. Luchkin, K. J. Stevenson, V. Petrov, and Pavel A. Troshin, "γ-Ray-Induced Degradation in the Triple-Cation Perovskite Solar Cells" *J. Phys. Chem. Lett.* **2019**, 10, 4, 813–818. <https://doi.org/10.1021/acs.jpcclett.8b03222>
4. **A. G. Boldyreva**, L. Frolova, I. S. Zhidkov, E. Z. Kurmaev, Vladimir G. Petrov and P. A. Troshin, "Unraveling the Material Composition Effects on Gamma Ray Stability of Lead Halide Perovskite Solar Cells: MAPbI<sub>3</sub> breaks the records" *J. Phys. Chem. Lett.* **2020**, 11, 7, 2630-2636. <https://doi.org/10.1021/acs.jpcclett.0c00581>
5. S. Tsarev, **A. G. Boldyreva**, S.Yu. Luchkin, M. Elshobaki, M. I Afanasov, K.J. Stevenson and Pavel. A. Troshin, "Hydrazinium-assisted stabilisation of methylammonium tin iodide for lead-free perovskite solar cells", *J. Mater. Chem. -A.*, **2018**, 6, 21389-21395 <https://doi.org/10.1039/C8TA07699E>
6. M. Elnaggar, **A. G. Boldyreva**, M. Elshobaki, S. A. Tsarev, A. V. Danilov, Y. S. Fedotov, O. R. Yamilova, S. I. Bredikhin, K. J. Stevenson and P. A. Troshin "Decoupling Contributions of Charge-Transport Interlayers to Light-Induced Degradation of p-i-n Perovskite Solar Cells" *RRL Solar*. <https://doi.org/10.1002/solr.202000191>

## Author's Contribution

**Publication 1:** Impact of charge transport layers on the photochemical stability of MAPbI<sub>3</sub> in thin films and perovskite solar cells.

The author is mainly responsible for this work. The author performed all the experiments, prepared samples for photostability tests, analyzed them with UV-vis spectroscopy and X-ray diffraction analysis and finalized the results in a manuscript.

**Publication 2:** Unraveling the impact of hole-transport materials on photostability of perovskite films and p-i-n solar cells.

The author is mainly responsible for this work. The author performed all the experiments, prepared samples for the photostability tests, analyzed them with a UV-vis and PL spectroscopy, X-ray diffraction analysis, and atomic force microscopy.

**Publication 3:**  $\gamma$ -Ray-Induced Degradation in the Triple-Cation Perovskite Solar Cells.

The author is mainly responsible for this work. The author prepared all samples for gamma-ray exposure, fabricated solar cells, and evaluated their characteristics, investigated the behavior of thin films with various analytical tools, including UV-vis, XRD, and PL.

**Publication 4:** Unraveling the Material Composition Effects on Gamma Ray Stability of Lead Halide Perovskite Solar Cells: MAPbI<sub>3</sub> breaks the records.

The author is mainly responsible for this work. The author prepared thin films and solar cells based on MAPbI<sub>3</sub>, MAPbBr<sub>3</sub>, Cs<sub>0.15</sub>FA<sub>0.85</sub>PbI<sub>3</sub>, Cs<sub>0.1</sub>MA<sub>0.15</sub>FA<sub>0.75</sub>PbI<sub>3</sub> materials, analyzed optical properties of thin films and JV characteristics of the devices after gamma exposure, performed numerical data analysis and prepared a manuscript.

**Publication 5:** Hydrazinium-assisted stabilisation of methylammonium tin iodide for lead-free perovskite solar cells.

The author prepared samples of methylammonium tin iodide with and without hydrazinium for degradation experiments. The author performed a photodegradation test and measured UV-vis for degraded samples.

**Publication 6:** Decoupling Contributions of Charge-Transport Interlayers to Light-Induced Degradation of p-i-n Perovskite Solar Cells.

The author prepared samples: ITO/PTAA/perovskite and ITO/NiO<sub>x</sub>/perovskite for ToF-SIMS analysis. The author contributed to the manuscript preparation.

## **Acknowledgments**

I would like to thank the whole research group of the center of Energy System Technologies in Skoltech. This thesis would not be accomplished without great support from my lab colleagues. Thanks to Azat Akbulatov for teaching me how to fabricate my first perovskite solar cells, thanks to Sergey Tsarev for answering my endless questions and helping out on any situation in the lab. Thanks to Moneim Ismail, Marina Ustinova, Marina Tepliakova, Mayuri Mangrulkar, Mohamed Elnaggar, Artyom Novikov, Olga Yamilova, Lyubov Frolova, Veronika Khalchenia, Ruslan Timerbulatov, Sergey Luchikin, Artem Zaikin for a wonderful team spirit and round-the-clock support. A special thanks go to my PhD supervisor professor Pavel Troshin who was extremely patient while reviewing my research results and highly responsive to all my inquiries. I also would like to acknowledge the contribution of Professor Keith Stevenson who inspired all of us for fruitful research work and was an outstanding leader of our center. Moreover, I thank Professor Alexey Buchachenko who made all the PhD thesis preparation and defense process very smooth and trouble-free. I am grateful to my husband and my family for always believing in me and supporting in the most difficult periods of my life.

My PhD journey has come to an end. I will never forget these wonderful 4 years that made me stronger and wiser. Thanks again to all the people who were around during this time.

## Table of Contents

Abstract .....	3
Publications .....	5
Author's Contribution .....	6
Acknowledgments .....	8
List of Symbols, Abbreviations.....	11
Chapter 1. Introduction .....	13
1.1 Evolution of Photovoltaics .....	13
1.2 Perovskite solar cells as an emerging PV technology .....	16
1.3 Operation stability issues in perovskite solar cells.....	19
1.3.1 Extrinsic stability .....	20
1.3.2 Intrinsic stability: photochemical and thermal.....	22
1.3.3 Interfacial stability .....	23
1.3.4 Radiation stability .....	26
1.4 Research goal.....	28
1.5 Thesis outline.....	29
Chapter 2. Impact of CTL material on photochemical stability of MAPbI <sub>3</sub> in thin films and perovskite solar cells .....	30
2. Motivation .....	30
2.2 Materials and methods.....	30
2.3 Photostability of MAPbI <sub>3</sub> .....	34
2.4 Impact of CTL underlayers on the photochemical stability of MAPbI <sub>3</sub> .....	35
2.5 Effect of CTLs as top coatings for MAPbI <sub>3</sub> thin films.....	45
2.6 Effect of CTLs on device stability.....	49
2.7 Summary.....	56
Chapter 3. Unraveling the impact of perovskite and HTL composition on the interfacial photostability of the multilayered stacks and p-i-n solar cells.....	57
3.1 Motivation .....	57
3.2 Materials and methods.....	57

3.3 The impact of HTL material on MAPbI <sub>3</sub> photostability .....	60
3.4 The impact of HTL materials on the operational stability of a series of complex lead halides .....	64
3.5 Impact of PC <sub>61</sub> BM upper coating on the photostability of lead halide perovskites in ITO/HTL/perovskite/PC <sub>61</sub> BM sample configuration.....	76
3.6 Impact of absorber material on the operational stability of PSCs .....	83
3.7 Summary.....	84
Chapter 4. Gamma rays induced halide phase segregation in the triple-cation perovskite solar cells .....	86
4.1 Motivation .....	86
4.2 Materials and methods.....	86
4.3 Gamma rays induced halide phase segregation in perovskite solar cells and thin films .....	89
4.4 Summary.....	103
Chapter 5. Unraveling the material composition effects on gamma ray stability of lead halide perovskite solar cells .....	104
5.1 Motivation .....	104
5.2 Materials and methods.....	104
5.3 Gamma ray stability of perovskite materials in thin films .....	105
5.4 Gamma ray stability of perovskite materials in solar cells.....	112
5.4 Summary.....	123
Conclusions .....	125
Bibliography.....	129

## List of Symbols, Abbreviations

ALD – Atomic Layer Deposition  
AM-KPFM – Amplitude Modulated Kelvin Probe Force Microscopy  
AM 1.5G – Air Mass 1.5 Global  
a-Si – Amorphous Silicon  
ATS -1 - Applications Technology Satellite  
BHJ – Bulk Heterojunction  
CdTe – Cadmium Telluride  
CIGS - Copper Indium Gallium Selenide  
CSSCs – Crystalline Silicon Solar Cells  
c-Si – Crystalline Silicon  
DMF – Dimethylformamide  
DMSO – Dimethylsulfoxide  
DSSCs – Dye-Sensitized Solar Cells  
EDX – Energy-Dispersive X-ray  
EQE – External Quantum Efficiency  
ETL – Electron Transport Layer  
ETM – Electron Transport Material  
FA – Formamidinium  
FAI – Formamidinium Iodide  
FF – Fill Factor (%)  
FWHM – Full Width at Half Maximum  
GaAs – Gallium Arsenide  
Gy – Grey (1 Gy = 0.1 kRad)  
HBL – Hole Blocking Layer  
HOMO – Highest Occupied Molecular Orbital  
HTL – Hole Transport Layer  
HTM – Hole Transport Material  
InP – Indium Phosphide  
ISS – International Space Station  
ITO – Indium Tin Oxide  
 $J_{sc}$  – Short Circuit Current Density  
LEO - Low Equatorial Orbit  
LiTFSI - Lithium bis(trifluoromethylsulfonyl)imide  
MA – Methylammonium

MAI – Methylammonium Iodide  
MAPbI<sub>3</sub> - Methylammonium Lead Iodide  
NASA – National Aerospace Agency  
NDI – Naphthalene Diimide  
NiO<sub>x</sub> – Nickel Oxide  
NREL – National Renewable Energy Laboratory  
NTS -2 – Navigation Technology Satellite  
PCBA - Phenyl-C<sub>61</sub>-butyric acid  
PC<sub>61</sub>BM - Phenyl-C<sub>61</sub>-butyric acid methyl ester  
PC<sub>71</sub>BM - Phenyl-C<sub>71</sub>-butyric acid methyl ester  
PCE – Power Conversion Efficiency  
PDI – Perylene Diimide  
PEDOT:PSS – Poly(3,4-ethylenedioxythiophene) polystyrene sulfonate  
PL – Photoluminescence  
PSCs – Perovskite Solar Cells  
p-Si - Polycrystalline silicon  
PTAA – Poly[bis(4-phenyl)(2,4,6-trimethylphenyl)amine]  
PTA - Poly[bis(4-phenyl)(4 -trimethylphenyl)amine]  
PV – Photovoltaic  
OPVs – Organic Photovoltaics  
QDs – Quantum Dots  
SEM – Scanning Electron Microscopy  
Spiro-OMeTAD – 2,2',7,7'-Tetrakis[N,N-di(4-methoxyphenyl)amino]-9,9' Spirobifluorene  
tBP - 4-tert-butylpyridine  
TF - Tolerance Factor  
TID – Total Ionizing Dose  
ToF-SIMS - Time of Flight Secondary Ion Mass Spectrometry  
V<sub>oc</sub> – Open Circuit Voltage  
XPS – X-ray Photoelectron Spectroscopy  
XRD – X-ray Diffraction

## Chapter 1. Introduction

### 1.1 Evolution of Photovoltaics

Solar energy being the most available energy source on our planet started to be used for power generation only in the last century. Nowadays it is the fastest-growing energy market that occupies about 3% of globally produced electric power.<sup>1</sup> According to BP Energy Outlook 2019, by 2040 solar power will make over 12% of the total generated power worldwide (Figure 1).<sup>1</sup> The growth in solar energy is dominated by China, India, and EU markets.

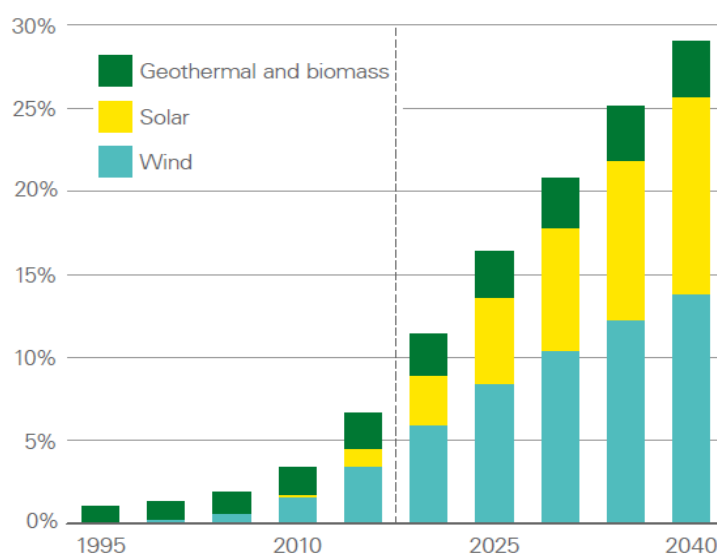


**Figure 1.** Global renewables: share of power generation by source.<sup>1</sup>

Most of the solar cell market is occupied by the crystalline silicon solar cells (CSSC), which were developed as early as in the 1950s. At that time solar cells were used mainly for space shuttles and satellites due to inexcusably high cost. Later, driven by the world oil crisis in 1973 they found a terrestrial application.

Single-crystal Si or c-Si solar panel consists of wafers cut from the same large Si crystal painstakingly grown under carefully controlled conditions. This process is time-consuming and energy-intensive and has a big impact on the final cost of the solar cell. However, in the last decade due to the massive production of photovoltaics (PV) in

China, the cost of c-Si PV module decreased from 3.5 to 0.45\$ per peak watt (Figure 2).<sup>2</sup>

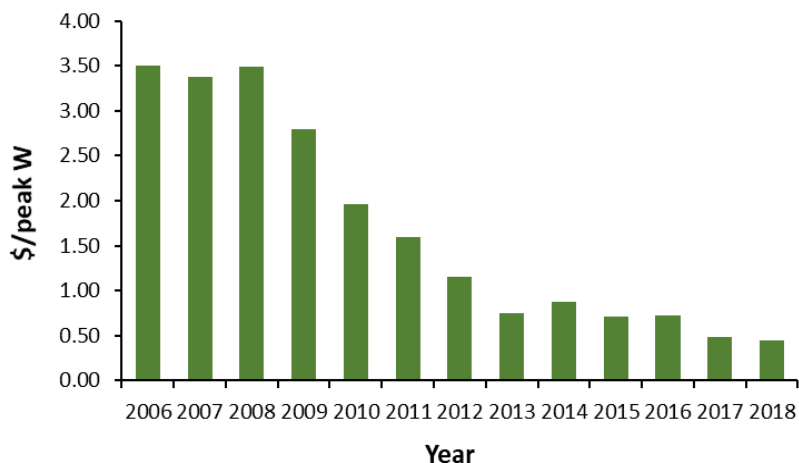


**Figure 2.** The average cost of PV c-Si module (U.S. Energy Information Administration, EIA).<sup>2</sup>

C-Si solar cells are also one of the leading solar cell technologies in terms of power conversion efficiency (PCE). According to the NREL efficiency chart<sup>3</sup> presented in Figure 3, for decades scientists could not produce single-crystalline Si solar cells with PCE over 24%. Until 2014, when Masuko K. et al. reported 25.6% efficient heterojunction crystalline SSC.<sup>4</sup> Recently this record was broken by Yoshikawa K. et al. exceeding 26% efficiency.<sup>5</sup> Even though c-Si PV technology has achieved a remarkable cost/efficiency ratio, it still has some drawbacks which are needed to be solved. C-Si solar cells are heavy and bulky and can hardly be fabricated on flexible substrates. Moreover, monocrystalline silicon is challenging to produce and it has very high embodied energy, which might be an obstacle for further cost reduction. Later on, a polycrystalline Si (p-Si) solar cell technology was developed. P-Si wafers are produced from multiple Si crystals growing together. In this way, the process does not need to be as strictly controlled as in c-Si cells and it gets cheaper. However, PCE is lower with a record of 22.04% achieved by Junco Solar.<sup>3</sup>

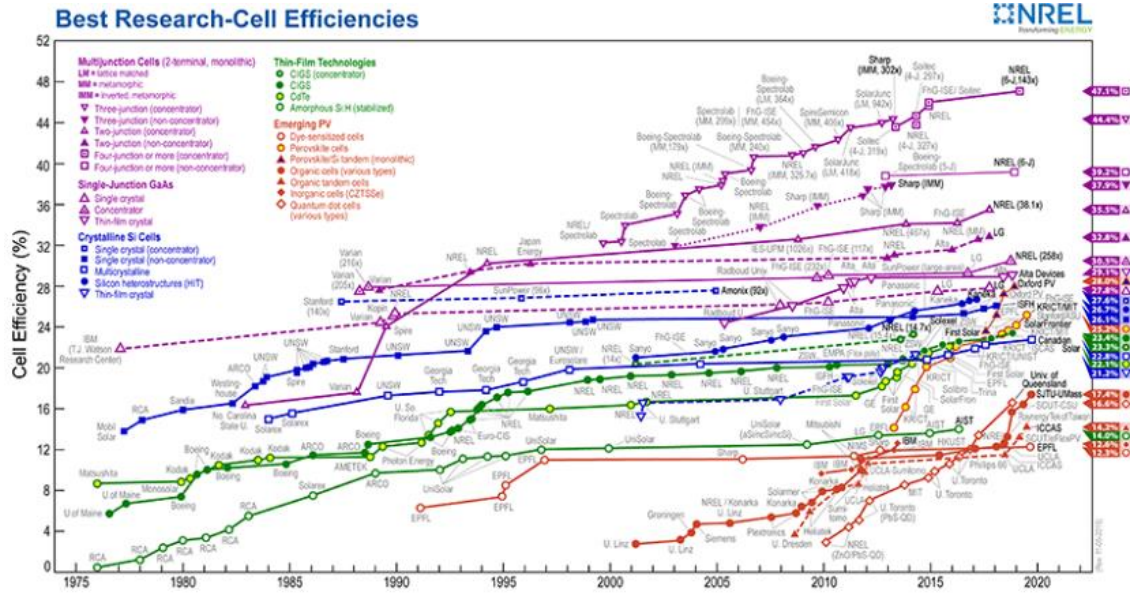


Figure 3. NREL best research - cell efficiencies chart.<sup>3</sup>

In the 1970s, a group of thin-film technologies raised on a market aiming at reducing solar cell production cost. These are mainly represented by amorphous Si (a-Si), Cadmium Telluride (CdTe) and Copper Indium Gallium Selenide (CIGS). Amorphous Si is deposited in a very thin layer on top of a conductive glass or metal substrate. Such technology has the lowest embodied energy among all the Si-based ones, but the efficiency is twice less than in polycrystalline solar cells. A-Si solar cells are quite popular in portable electronics, where the amount of generated power is not that important.

CdTe is one of the most successful thin-film technologies that can compete with c-Si cells. The current record is 22.1% achieved by the largest CdTe cell producer First Solar.<sup>3</sup> This technology is cheaper than c-Si and can be applied to flexible substrates, however some concerns about operation stability and material toxicity pushes it back. CIGS solar cells are even more efficient going beyond 23%<sup>3</sup> and not as toxic as CdTe, however, the production cost is higher than that of c-Si solar cells.

In the late 90s, the interest in solar cell development was recommenced after a long break. Scientists continued looking for cheaper materials that can revolutionize the power generation market. A new group of solar cells called Emerging PVs appeared in

the field. Dye-sensitized solar cells (DSSCs), organic photovoltaics (OPVs), quantum dot solar cells (QDSs) and PSCs are typically considered in this group. All of them allow producing solar cells using simple and cheap roll-to-roll technology on any required substrates including flexible ones. Unfortunately, the first three mentioned technologies so far were not able to reach efficiencies comparable to PCE of single-crystal SSCs. Only PSCs demonstrated rapid growth from an initial 3% to world record 25.2% within 11 years of development.<sup>3</sup> Such results along with cheap and simple fabrication processes make PSCs one of the strongest competitors of Si-based solar cells.

### 1.2 Perovskite solar cells as an emerging PV technology

Named after Russian mineral collector Lev Perovskiy, perovskite was first found in 1839 in the Ural Mountains by Gustav Rose. Later this mineral of  $\text{CaTiO}_3$  composition gave the name for the whole class of semiconductors which have the same cubic crystal structure with general formula  $\text{ABX}_3$  where X is an anion and A and B are cations of different sizes. The crystal structure of perovskite is depicted in Figure 4.

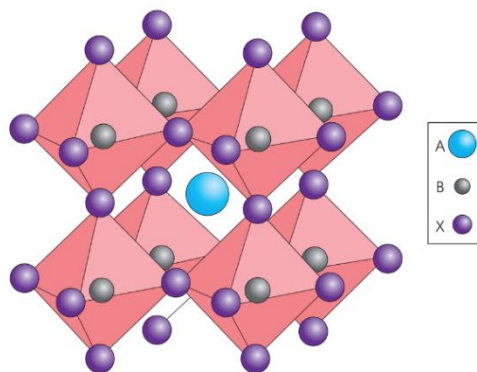


**Figure 4.** Schematic representation of perovskite crystal structure, where A, B are cations and X is an anion.<sup>6</sup>

In lead halide perovskites, the largest cation A in the middle of the cube is typically methylammonium ( $\text{CH}_3\text{NH}_3^+$ ) or formamidinium ( $\text{NH}_2\text{CHNH}_2^+$ ) but also can be inorganic such as  $\text{Cs}^+$  or  $\text{Rb}^+$ . Small anions X in the angles of the octahedron are halogen anions I<sup>-</sup>, Br<sup>-</sup>, Cl<sup>-</sup>. Cation B is the most commonly represented by  $\text{Pb}^{2+}$  but also can be  $\text{Sn}^{2+}$  or  $\text{Ge}^{2+}$ .

In 1926, Goldschmidt formulated the tolerance factor (TF) concept for inorganic solid-state perovskites; the relationship between the ionic radius of the A-site cation ( $r_A$ ), B-site cation ( $r_B$ ) and X-site anion ( $r_x$ ) is given in equation (1):

$$TF = (r_A + r_x) / \sqrt{2(r_B + r_x)}. \quad (eq.1)$$

Later on, this approach was extended for hybrid perovskite materials.<sup>7,8</sup> Thus, for both inorganic and hybrid perovskites the optimized TF lies in the range of 0.8 to 1.<sup>9,10</sup> It means that materials with such TF are expected to have a stable photoactive cubic phase.

Most studied MAPbI<sub>3</sub> perovskite has TF in this window ( $\approx 0.95$ )<sup>8</sup>, therefore it is widely used for PSCs fabrication. Notably, Formamidinium lead iodide (FAPbI<sub>3</sub>) perovskite has TF slightly above 1, therefore cubic perovskite structure is less stable than e.g. hexagonal polymorph at room temperature. CsPbI<sub>3</sub> with its small-sized Cs<sup>+</sup> cation has TF below 0.8, so orthorhombic structure becomes most favorable at room temperature. However, by mixing these cations in a certain proportion one can obtain Cs<sub>(1-x)</sub>FA<sub>x</sub>PbI<sub>3</sub> with an effective TF value between 0.8 and 1 and stable cubic phase suitable for PV applications (Figure 5). The same result can be achieved by mixing CsPbI<sub>3</sub> and CsPbBr<sub>3</sub>. CsPbBr<sub>3</sub> has TF of about 0.9 but due to a very wide bandgap, it is rarely used in solar cells in pure form. Adding a small amount of CsPbBr<sub>3</sub> to CsPbI<sub>3</sub> will give CsPbI<sub>2</sub>Br which has a decent combination of the relatively low bandgap and reasonably stable cubic phase.<sup>11</sup>

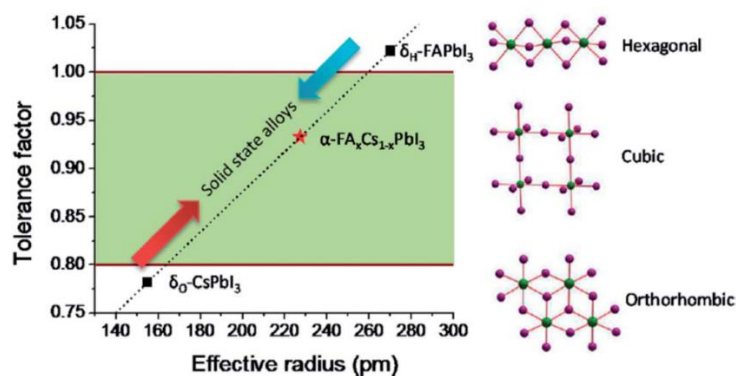


**Figure 5.** Schematic showing how TF can be used to stabilize the metastable phases of FAPbI<sub>3</sub> and CsPbI<sub>3</sub> with the formation of Cs<sub>(1-x)</sub>FA<sub>x</sub>PbI<sub>3</sub> with a stable cubic phase.<sup>12</sup>

Complex lead halides with  $ABX_3$  cubic structure showed unique optoelectronic properties that boosted scientific interest all around the world. Within 10 years the number of publications dedicated to PSCs has raised to 3600 and PCE of fabricated solar cells reached 25.2% in 2019 (Figure 6).<sup>3</sup>

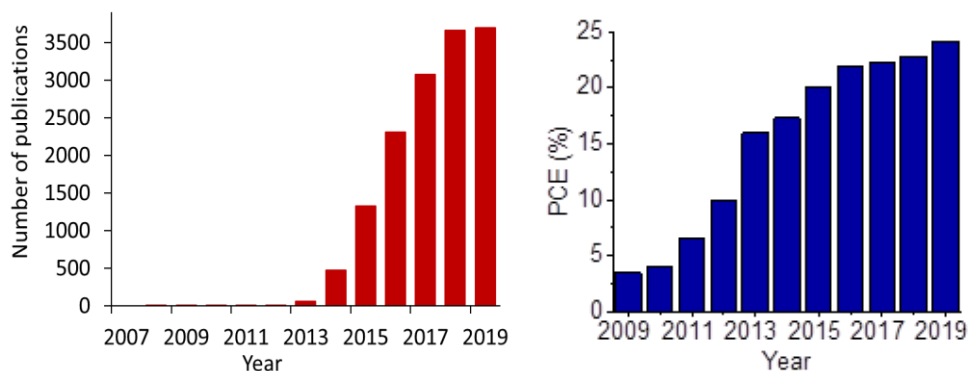


**Figure 6.** Publication activity on the topic “Perovskite solar cells” (left) and the evolution of PCE in PSCs (right).

T. Miyasaka’s research group became the first who reported the photovoltaic performance of PSCs.<sup>13</sup> They modified DSSCs by depositing  $CH_3NH_3PbBr_3$  and  $CH_3NH_3PbI_3$  perovskite nanocrystals on  $TiO_2$  achieving 2.8%<sup>13</sup> and later 3.6%.<sup>14</sup> In 2011 using the same approach the efficiency was increased to 6.5% by Park et. al.<sup>15</sup> Non-sensitized perovskite solar cells were first fabricated by the Snaith group with 10.9% efficiency.<sup>16</sup> A year after a group of S. Seok obtained 12% efficient solar cells with the configuration  $FTO/bl-TiO_2/mp-TiO_2/CH_3NH_3PbI_3/HTM/Au$ .<sup>17</sup> They investigated multiple hole-transport materials (HTM) with the best results reached for poly[bis(4-phenyl)(2,4,6-trimethylphenyl) amine (PTAA). Later on, it was found that complex lead halides with perovskite structure have ambipolar transport behavior which allowed to fabricate not only solar cells on mesoporous  $TiO_2$  but also with planar structure. Snaith et al.<sup>18</sup> obtained 15.4% efficient devices by co-evaporation of  $CH_3NH_3I$  and  $PbCl_2$ . Instead of the  $TiO_2$  scaffold, they used a compact solution-processed  $TiO_2$  layer as an electron transport material (ETM). Such rapid improvement in terms of efficiency resulted in a fact that in 2013 The Science magazine included perovskites in

the list of Top-10 breakthroughs of the year.<sup>19</sup> Variation of cations in the perovskite structure boosted device efficiency even further. In 2016 Grätzel et al.<sup>20</sup> demonstrated 21.1% efficient triple cation perovskite solar cell with complex structure  $\text{Cs}_x(\text{MA}_{0.17}\text{FA}_{0.83})_{(1-x)}\text{Pb}(\text{I}_{0.83}\text{Br}_{0.17})_3$ . The current world record reached 25.2% according to National Renewable Energy Laboratory and this number is continuously going up.<sup>3</sup>

### 1.3 Operation stability issues in perovskite solar cells

Even though the efficiency of PSCs is high enough to compete on a solar cell market, there is a big problem with operational stability. For the successful commercialization of any new solar cell technology, one should look at the factors of the golden triangle: cost, efficiency, and lifetime (Figure 7a).<sup>21</sup> As mentioned above, PSCs and CSSCs have very comparable PCEs. In 2018 the production of PSCs was estimated twice cheaper than of CSSCs (Figure 7b), however, the massive production of c-Si wafers, as well as updated power conversion efficiency, pushes the price down below 0.3 \$/W<sup>22</sup> (Figure 7c) and makes Si technology highly competitive. Nevertheless, the cost of PSCs potentially also can go down with massive production.

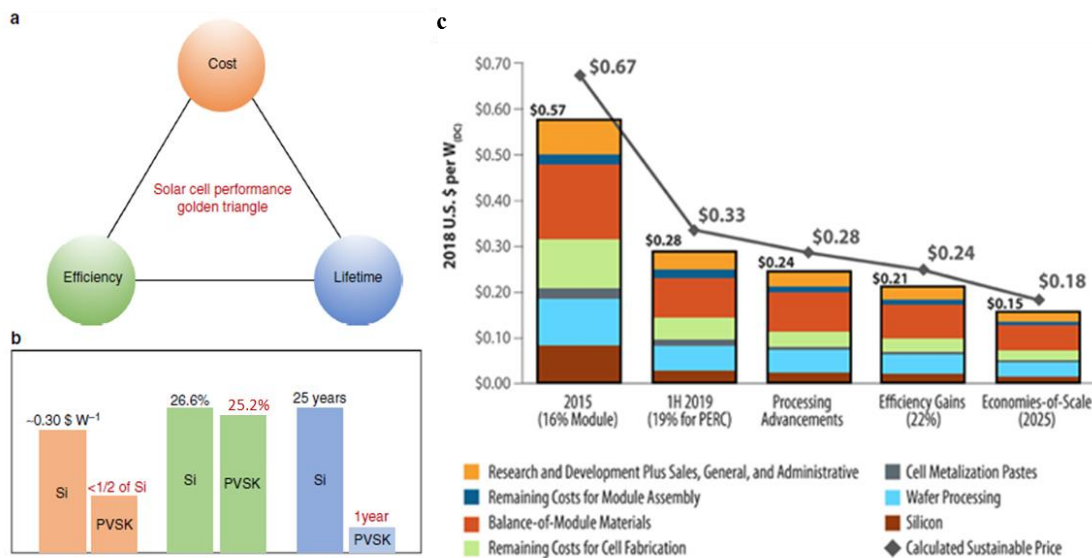


**Figure 7.** Comparison of c-Si and PSC - Golden triangle: cost, efficiency, and lifetime (a,b)<sup>21</sup> and historical, current, and projected cost of c-Si panels (c)<sup>22</sup>.

The only weak point of PSCs on the golden triangle is an operation lifetime. The best lifetime obtained for PSCs is about 10 000 h (around 1 year), but the PCE of such solar cells is only 12%.<sup>23</sup> If we set an efficiency threshold of 20% the best light-soaking stability is only 1000-2000 h.<sup>24,25</sup> Nowadays, the whole world is struggling to produce more stable PSCs varying material composition, looking for good encapsulating layers and stable CTLs. This issue becomes fundamental and should be prioritized over attempts to achieve higher PCEs.

Among the main factors affecting long term stability of perovskite material, one can name extreme sensitivity to moisture,<sup>26-30</sup> oxidation in the air in presence of light,<sup>31,32</sup> thermal<sup>33-35</sup>, and photochemical degradation<sup>36,37</sup> in the bulk and at the interfaces. Moisture and oxygen-induced processes are extrinsic factors, while temperature and light affect mainly the intrinsic stability of PSCs.

### 1.3.1 Extrinsic stability

Complex lead halides with perovskite structure (particularly MAPbI<sub>3</sub>) were found to be moisture sensitive which was revealed at the early stages of the research development. Many publications are dedicated to the degradation mechanisms induced by direct contact of perovskite material with water, as well as with humid air.<sup>26,29,30,38</sup> Extensive research in this area resulted in a determination of the veritable degradation mechanism: exposure to moisture leads to the formation of PbI<sub>2</sub> and monohydrate phase according to the reaction<sup>26</sup>:



Figure 8 shows the phase transition of perovskite material in the presence of moisture.

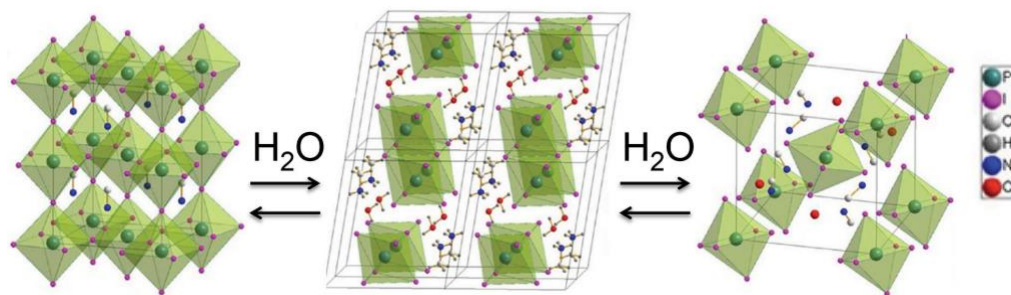


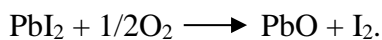
**Figure 8.** Change of perovskite crystal structure under the impact of moisture.<sup>38</sup>

In the formed phase,  $\text{MA}^+$  cation is no longer bonded to  $\text{I}^-$  and interacts with water molecules. Some researchers claim that this reaction is reversible if the material is exposed to dry air. However, if perovskite material contacts humid air in the presence of heat, methylamine irreversibly evaporates from the surface. To prevent hydration, perovskite material should be properly encapsulated.

Another degradation process in perovskite thin films intensively studied by researchers is oxidation in the presence of light.<sup>31,32</sup> Photoexcited electrons bond with oxygen molecules forming reactive species. This results in photo-oxidation of the perovskite layer following reaction<sup>31</sup>:



Lead Iodide gets further oxidized on with the formation of  $\text{PbO}$ . Due to the higher electronegativity of oxygen compared to iodine, the O atoms prefer to replace adjacent I atoms and bond to two Pb atoms:<sup>39</sup>



It was found, that  $\text{PbO}$  forms mostly on a surface and works as a protective layer for further oxidation of  $\text{PbI}_2$ .<sup>39</sup> It should be noted that the proposed oxidation mechanism is valid only in the presence of light.  $\text{MAPbI}_3$  films left in the air in the dark remain stable. Moreover, such a process was observed on the pristine perovskite layer, directly exposed to the environment while in completed solar cell stacks photooxidation is a problem of a much lower extent and depends on electron extraction properties of charge transfer layers.<sup>31</sup> To suppress photooxidation, the generated electrons should be extracted from perovskite material before they bond with oxygen by adjacent electron-

transporting layer, collected at the negative electrode, and pushed to the external circuit. For example, electron transfer to mesoporous TiO<sub>2</sub> outcompetes oxidation reaction slowing down the solar cell degradation.<sup>31,38</sup> However, even if the formation of superoxide O<sub>2</sub><sup>-</sup> was prevented by effective electron extraction, oxygen still can react with I<sup>-</sup> ions under the light. This reaction can be excluded only by a proper solar cell encapsulation.

### 1.3.2 Intrinsic stability: photochemical and thermal

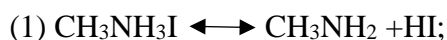
The main factors that influence material stability intrinsically are sunlight,<sup>36,37,40</sup> electric bias,<sup>41,42</sup> and temperature.<sup>33-35</sup> Depending on material composition, these factors can affect stability at a different rate. MAPbI<sub>3</sub> is the most popular material used in PSCs and also the most vulnerable to the mentioned stress factors. Due to the high mobility of MA<sup>+</sup> ions, MAPbI<sub>3</sub> rapidly decomposes at elevated temperatures starting from 45-50 °C<sup>36,43</sup>:



Lead iodide under light further decomposes to metallic lead and iodine vapor<sup>44</sup>:



While MAI can decompose mainly by two paths:<sup>33,35,45,46</sup>



There are still active debates about the role of each reaction in MAPbI<sub>3</sub> decomposition. It is believed that the higher is the temperature, the more the equilibrium is shifted towards the 2<sup>nd</sup> reaction.<sup>46</sup> In both cases, volatile components can penetrate through CTLs and irreversibly leave the system.<sup>47,48</sup>

MA<sup>+</sup> cation makes the perovskite deposition process very reproducible and simple, but at the same time, it makes solar cells extremely sensitive to operating conditions. Since the temperature of solar panels in sunny days in hot regions can reach 80-100°C, the usage of MAPbI<sub>3</sub> in PSCs is under big question, unless efficient encapsulation layers preventing the loss of volatile components are found. Nowadays many publications are dedicated to the search of cations that can replace MA<sup>+</sup> in

complex lead halides. Different combinations of cations and halides were studied in the last 5 years to find the most stable configuration. Recently MA-free systems such as  $\text{Cs}_x\text{FA}_{(1-x)}\text{PbI}_3$  and  $\text{Cs}_x\text{FA}_{(1-x)}\text{PbBr}_x\text{I}_{(1-x)}$  have attracted particular attention showing remarkably high PCE and enhanced thermal stability. Saliba et. al have shown that it is possible to produce efficient PSC (20.35%)<sup>49</sup> without  $\text{MA}^+$  cation and with improved stability. However, the absence of  $\text{MA}^+$  cation significantly worsens phase stability and requires more careful film preparation: annealing temperature should be optimized to exclude the formation of the beta phase and  $\text{PbI}_2$ .<sup>50</sup>

### 1.3.3 Interfacial stability

Along with the stability issues of absorber material, researchers are struggling to find suitable CTLs that will accomplish a stable solar cell configuration. Chemical processes occurring at the interfaces between CTLs and perovskite material are often the most crucial for solar cell operation stability. CTLs have to be uniform, compact and non-permeable for the volatile perovskite degradation products to achieve the desired stabilization and isolation characteristics.<sup>35</sup>

Depending on CTLs, different interfacial degradation mechanisms can occur. Fullerene derivatives (e.g.  $\text{PC}_{61}\text{BM}$ ) commonly used as ETLs in p-i-n solar cells were found to facilitate the decomposition of  $\text{MAPbI}_3$  by absorbing MAI in the cavities between the fullerene spheres.<sup>51</sup> Introducing additional ZnO nanoparticles as a hole blocking layer (HBL) placed atop the  $\text{PC}_{61}\text{BM}$  films helps to mitigate the problem of the metal electrode corrosion, but can hardly prevent the perovskite decomposition.<sup>52</sup>  $\text{TiO}_2$  being one of the most popular ETLs for n-i-p PSCs was also found to be reactive with the perovskite layer. Applied bias induces a reversible oxygen migration from  $\text{TiO}_2$  to the  $\text{MAPbI}_3$  layer even in the absence of other stress factors. Oxygen migration affected the perovskite phase crystallinity and facilitated the formation of  $\text{PbI}_2$ .<sup>53</sup> The degradation at the perovskite/ETL interface was suppressed by the insertion of a diffusion barrier interlayer of  $\text{Sb}_2\text{S}_3$  between the  $\text{TiO}_2$  and  $\text{MAPbI}_3$  layers.<sup>54</sup> The operation stability of PSCs utilizing mesoporous oxide scaffold was enhanced by replacing  $\text{TiO}_2$  with  $\text{Al}_2\text{O}_3$ .<sup>38</sup>

The contact between the HTL and the perovskite material is also crucial for stable solar cell operation. Spiro-OMeTAD (2,2',7,7'-Tetrakis[N,N-di(4-methoxyphenyl)amino]-9,9'-spirobifluorene) commonly used as an HTL in PSCs with the n-i-p architecture was shown to be the main cause of device degradation by many researchers.<sup>55-57</sup> The main reactive species are 4-tert-butylpyridine (tBP) and lithium bis(trifluoromethylsulfonyl)imide (LiTFSI) - typical modifying additives for HTLs with low hole mobility.<sup>58,59</sup> tBP was shown to be dissolving PbI<sub>2</sub>,<sup>60</sup> LiTFSI salt is hygroscopic and attracts moisture from the environment and it can also react with some perovskite decomposition products.<sup>37</sup> The cation-radical of spiro-OMeTAD might oxidize I<sup>-</sup> with the formation of I<sub>2</sub>, which represents an important degradation pathway at the perovskite/doped HTL interface.<sup>56</sup> At the same time, spiro-OMeTAD molecules tend to crystallize at elevated temperatures, which is another mechanism of the device failure.<sup>55</sup>

PEDOT:PSS was extensively studied within the last decade as HTL material for p-i-n PSCs.<sup>56-63</sup> Many publications reported high reactivity of PEDOT:PSS with adjacent layers: semitransparent electrode and absorber material.<sup>62,63,56,48</sup> PEDOT:PSS has acidic nature since it represents a salt of a weak organic base and strong polystyrene sulfonic acid (PSS). Therefore, PEDOT:PSS can react with In<sub>2</sub>O<sub>3</sub> and etch ITO with the release of mobile In<sup>3+</sup> ions. This kind of chemistry negatively impacts both device efficiency and stability.<sup>62,63</sup> It was also revealed by Time of Flight Secondary Ionic Mass Spectroscopy (ToF-SIMS) analysis the appearance of S-ions at the PC<sub>61</sub>BM/Ag interface.<sup>56</sup> Nevertheless, a great number of methods to improve PEDOT:PSS performance and device stability were developed in the last years, including solvent post-treatment,<sup>64,65</sup> the addition of graphene oxide protective layer<sup>66,67</sup> or HTL doping.<sup>68</sup>

Along with PEDOT:PSS, big attention was given to p-type metal oxides such as NiO<sub>x</sub> and CuO as they normally provide higher open-circuit voltage (V<sub>OC</sub>) values and better energy alignment. First time PEDOT:PSS was replaced with NiO<sub>x</sub> in polymer bulk heterojunction solar cells (BHJs).<sup>69</sup> Soon it became popular in PSCs giving efficiencies as high as 18-20%.<sup>70-73</sup> NiO<sub>x</sub> layer properties can vary depending on the deposition method: the easiest and most common way is solution processing,<sup>62,74</sup> but

spattering,<sup>75</sup> and atomic layer deposition (ALD)<sup>76</sup> also quite popular techniques. Along with improved efficiencies the researchers claim superior air stability of PSCs based on NiO<sub>x</sub>.<sup>73,77,78</sup> However, very few if any papers are dedicated to the photostability of such systems.

The best efficiencies ever obtained in inverted PSCs were gained from devices using PTAA<sup>58,59,79,80</sup> as an HTL. PTAA is also a popular HTL in n-i-p architectures. It has rather low hole mobility and, therefore, is usually doped and/or modified using certain additives such as LiTFSI and tBP. However, as was mentioned earlier, these compounds are highly reactive and, therefore, badly influence PSCs stability. Recently, it was shown that non-doped PTAA can provide device efficiencies of up to 18.2% if appropriate HTL thickness is used.<sup>79,80</sup> However, the photostability of the PTAA/perovskite interface was not thoroughly investigated until now.

Recently it was shown that polytriphenylamine derivative (named PTA in the literature) with only one methyl group in each repeating unit is even more promising HTL in PSCs.<sup>81</sup> It was first synthesized by I. K. Yakushchenko et al.<sup>82</sup> and used as HTL in electroluminescent devices. The main advantages of PTA over PTAA is deeper-lying HOMO and Fermi energy levels which effectively minimize interface recombination. Moreover, PTA has better charge transport properties due to the more compact molecular structure.

Quite often the researchers use hybrid HTL layers, trying to obtain improved solar cell characteristics. Combination of PEDOT:PSS/PTAA on flexible substrates resulted in a competitive 14.23%, which is higher than in the absence of PTAA.<sup>83</sup> NiO<sub>x</sub>/PTAA system is quite a common combination, as PTAA smoothens NiO<sub>x</sub> surface and enhances charge transport.<sup>84,85</sup> Best obtained efficiency in single junction PSCs with such HTL is 17.1%.<sup>85</sup>

The list of CTL/interfaces is endless and some of them enable chemical reactions that destabilize solar cell performance. The current trend in the PSC research field is to reveal such CTLs that can form a stable interface with adjacent layers and minimize interfacial degradation processes in realistic solar cell operational conditions.

#### *1.3.4 Radiation stability*

Since the emergence of the space industry, different types of solar cells have been used as the main electrical energy source to power spacecrafts and satellites. Solar irradiation in space is substantially stronger than on Earth, and it has no disturbance in a form of clouds, which makes it a more consistent and reliable energy source to convert photons to electrical energy. However, high-energy particles and radiation sources, such as protons, electrons, X-rays and gamma rays from such entities as Sun flares and galactic radiation can damage and even destroy conventional semiconductor materials. One of the first pioneering works published in 1963 reported the rate of the degradation of a silicon solar cell caused by electron damage:<sup>86</sup> at short circuit current the device degrades by 25% within 45 days in Circular equatorial orbit. Another report on solar cell degradation in space was presented in *Nature*.<sup>87</sup> Different types of solar cells available at that time were fixed on NTS-2, a Navigation Technology Satellite, that spent 223 days on a geocentric orbit (20000 km). The experiment showed a reduction in the device efficiency by 8 to 47%, depending on the type of the cell, while the origin of aging effects and the doses of radiation affecting the solar cells in space were unknown. Some reports were dedicated to the radiation stability of the solar cells based on A3B5 materials such as GaAs alone or in tandems with other absorbers such as InP.<sup>88-90</sup> Developing methodology for suppressing a severe impact of high-energy particles on conventional semiconductor materials became one of the main tasks for the space industry.

A number of reports are dedicated to the modeling of the solar cell device degradation in space.<sup>91-93</sup> However, predicting the degradation behavior is a complicated task considering the flared nature of the solar radiation and a strong dependence of the absorbed radiation dose over the orbit distance. The total ionizing dose (TID) is used to determine the radiation tolerance of the space equipment. For satellites, working at low equatorial orbit (LEO), TID should be within 100-1000 Gy.<sup>94</sup> Electrons, protons, and photons with energies below 1 MeV could be partially stopped by shielding. NASA reported results of a shielding experiment performed on the ATS-

1 spacecraft, which spent 416 days at the distance of 35792 km.<sup>95</sup> Non-covered Si-based solar cells showed a power reduction by 90%, while the cells protected by 0.15 mm shielding degraded by 8.5% only. Indeed, 100  $\mu\text{m}$  thick glass can stop 3 MeV protons.<sup>96</sup> Recent progress in this field has shown that Si-based solar cells with good glass encapsulation can work in space for years without significant degradation. It was declared that Si solar cells installed at the International Space Station (ISS) from December 2000 to February 2003 degraded only by 0.45%.<sup>97</sup>

The main disadvantage of the glass encapsulation is a reduced solar cell power per unit mass. Conventional solar panels are quite heavy, so their deployment on satellites and spacecrafts is very costly. This aspect is the main reason why researchers are continuously looking for alternative absorber materials, which could decrease the weight of solar cells substantially while being at least as efficient as silicon. In this way, PSCs which currently deliver power conversion efficiencies of up to 25.2%<sup>3</sup> can be a good candidate. At the same time, PSCs seem hardly suitable for a severe space environment if one considers the current operational stability of such devices.

Nevertheless, PSCs were found to have superior radiation stability compared to the conventional types of solar cells. It was shown that PSCs based on  $\text{Cs}_x\text{FA}_{0.85}\text{MA}_{0.15}\text{Pb}(\text{I}_{0.85}\text{Br}_{0.15})_3$  ( $x < 0.05$ ) and Cl-doped  $\text{MAPbI}_{(3-x)}\text{Cl}_x$  can withstand  $10^{16}$ - $10^{15}$   $\text{p}/\text{cm}^2$  of electrons (1 MeV) and protons (50 KeV)<sup>98</sup>, respectively, which are known to completely destroy crystalline Si, GaAs, and InGaP/GaAs-based solar cell.<sup>99</sup> Another work reported decent stability of  $\text{MAPbI}_3$ -based solar cells under proton irradiation of  $10^{13}$   $\text{p}/\text{cm}^2$  leading to a decrease in short circuit current density ( $J_{\text{SC}}$ ) by 20%.<sup>100</sup> However, the solar cells were able to recover to nearly initial performance upon continuous storage thus featuring a remarkable self-healing effect.<sup>100</sup> Later, the solar cells based on the  $\text{Cs}_{0.05}\text{MA}_{0.17}\text{FA}_{0.83}\text{Pb}(\text{Br}_{0.17}\text{I}_{0.83})_3$  perovskite formulation were shown to maintain 95% of their initial efficiency after proton irradiation of 68 MeV with a total proton dose of  $\phi = 1.02 \times 10^{13}$   $\text{p}/\text{cm}^2$ .<sup>101</sup>

Gamma ray stability of PSCs should be explored along with the effects induced by electron/proton irradiation exposure. Gamma rays have the highest penetrating

ability and cannot be stopped by regular encapsulation materials. For over 20 years of exploitation in space, solar cells can accumulate a big gamma ray dose (e.g. 1000 Gy)<sup>94</sup>, which can significantly affect the solar cell performance. Recently, it was shown that  $\text{Cs}_{0.05}\text{FA}_{0.81}\text{MA}_{0.14}\text{PbI}_{2.55}\text{Br}_{0.45}$  perovskite is more resistant to gamma rays than a glass substrate used for PSC fabrication.<sup>102</sup> Indeed, glass substrates exposed to high energy particles undergo darkening due to color defect formation.<sup>103</sup> The decrease in the substrate transmittance led to a decay of photocurrent density and efficiency of the solar cell. However, the absorber material itself and the overall photovoltaic stack did not degrade under radiation exposure. Another work reported very similar results for  $\text{FA}_{0.945}\text{MA}_{0.025}\text{Cs}_{0.03}\text{Pb}(\text{I}_{0.975}\text{Br}_{0.025})_3$  perovskite exposed to gamma-rays with a dose of 500 kRad.<sup>104</sup> A further research in this field is required to reveal the promising perovskite solar cell configurations suitable for space applications.

#### **1.4 Research goal**

There is a strong need for a new generation of PSCs with long operational lifetimes enabled by appropriate choice of all functional materials forming stable and inert interfaces in the device stack. A systematic and comparative study of multiple interfaces under the effect of light and/or ionizing radiation is missing in the field. In this work we tried to fill this gap by solving the following tasks:

- Revealing the impact of different charge-transport interlayers on the photostability of  $\text{MAPbI}_3$  films and solar cells with a focus on the interface-induced degradation mechanisms;
- Investigation of the interface-induced degradation processes for a broad range of lead halide perovskites combined with different HTLs in order to reveal possible relationships between the materials composition, structure, and the operational stability of these multicomponent systems. As one of the anticipated outcomes, revealing the most stable combinations of perovskite absorbers and HTLs can be envisioned.

- Identifying the mechanisms of the revealed bulk (within the absorber layer) and interfacial degradation processes using a set of complementary analytical techniques;
- Performing a comparative radiation stability study for a series of lead halide perovskites in thin films and solar cells and evaluate their potential for space applications.

### **1.5 Thesis outline**

In the first chapter, a literature review on solar cell technologies in general and PSCs, in particular, is presented. The main approaches to improving device operational stability required for successful perovskite solar cell commercialization were analyzed. The second chapter is dedicated to the interface-induced degradation pathways involving the most popular perovskite material  $\text{MAPbI}_3$  and various charge-transport interlayers. The third chapter is focused on the systems with p-i-n configuration, where interface degradation effects occurring between 4 different HTLs and 5 perovskite materials were analyzed. The potential of PSCs for space applications is assessed in the fourth and fifth chapters of this work. The radiation hardness was studied for various perovskite materials including mixed halide and pure iodide perovskite formulations.

## **Chapter 2. Impact of CTL material on photochemical stability of MAPbI<sub>3</sub> in thin films and perovskite solar cells**

### **2. Motivation**

There is growing evidence that MAPbI<sub>3</sub> thin films have poor intrinsic stability.<sup>33,27,36,100,101</sup> In particular, it was revealed that MAPbI<sub>3</sub> starts to decompose under the elevated temperature of 50 °C.<sup>33</sup> Fortunately, all chemical reactions involved in MAPbI<sub>3</sub> decomposition are reversible. To prevent this kind of degradation one needs to encapsulate perovskite absorber films between the adjacent charge transport layers. These layers have to be uniform, compact, and non-permeable for the volatile perovskite degradation products to achieve the desired isolation characteristics.<sup>47</sup> In this chapter, we systematically explored a series of CTLs in combination with MAPbI<sub>3</sub> in order to reveal those with good encapsulation characteristics.

### **2.2 Materials and methods**

The detailed experimental protocol is presented in Figure 9. It was developed following the recommendations of ISOS L-2 stability testing protocol initially proposed for organic photovoltaics (OPVs)<sup>107</sup> and later adjusted for PSCs.<sup>108</sup> ISOS L-2 protocol suggests performing a light soaking aging experiment in an inert atmosphere at 65-85 °C, with light power within 80-100 mW/cm<sup>2</sup> for at least 1000 h. Device measurement is recommended to perform in MPP or OC mode. In our experiment light power was 50 mW/cm<sup>2</sup> (with the reduction to 40 mW/cm<sup>2</sup> in the exp. described in Chapter 3) and temperature 45 °C, which is less than recommended, but sufficient to reveal important heat- or light-induced degradation mechanisms.

In the 1<sup>st</sup> stage of the experiment, Glass/CTL/MAPbI<sub>3</sub> systems were exposed to light soaking (50 mW/cm<sup>2</sup>, 45 °C). In the 2<sup>nd</sup> stage, the same CTLs were deposited on top of MAPbI<sub>3</sub> and these samples were exposed to light soaking. In the 3<sup>d</sup> stage, ITO/CTL<sub>1</sub>/MAPbI<sub>3</sub>/CTL<sub>2</sub> samples were subjected to the light for 100 h and afterward completed for solar cell characterization.

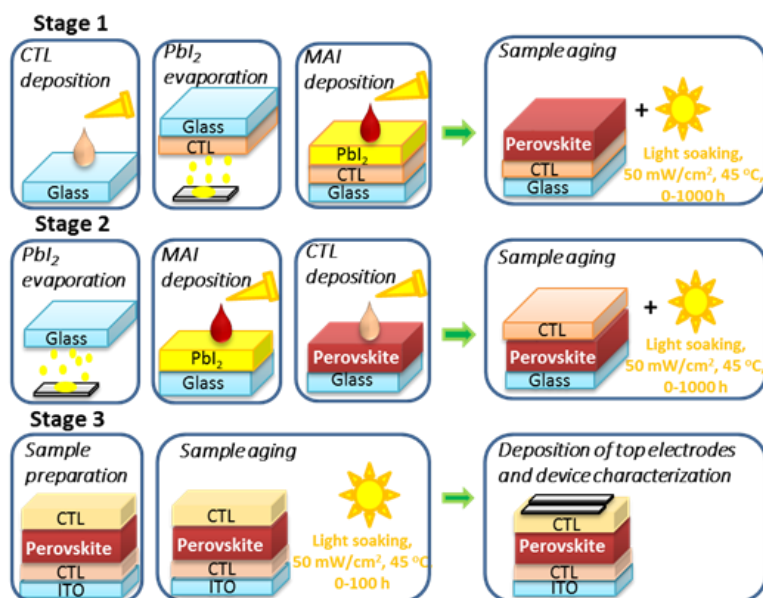


**Figure 9.** Schematic representation of the experimental methodology.

### *Film deposition and sample preparation*

Glass substrates were cleaned by sonication in deionized water, acetone and isopropyl alcohol (IPA) for 10 min each, dried with air and subjected to a plasma cleaning for 300 s. While preparing glass/CTL/MAPbI<sub>3</sub> stacks, a CTL film was first deposited on glass (Figure 9, stage 1). NDI and PDI powders were dissolved in chloroform (10 mg/ml) and spin-coated at 1000 rpm. PC<sub>61</sub>BM and PC<sub>71</sub>BM were dissolved in chlorobenzene (20 mg/mL) and spin-coated at 2000 rpm. Spiro-OMeTAD solution in chlorobenzene (40 mg/mL) was deposited at 3000 rpm. Next, PbI<sub>2</sub> films (100 nm) were evaporated atop glass/CTL samples in a high vacuum ( $5 \cdot 10^{-6}$  mbar) chamber installed inside a nitrogen glove box. The solution of MAI in isopropanol (25 mg/mL) was spin-coated at 3000 rpm dynamically on air. All substrates were annealed for 3 hours at 85 °C inside the nitrogen glove box until the formation of the perovskite phase was virtually complete and absorption spectra of the films were saturated (i.e. stopped changing). While preparing glass/MAPbI<sub>3</sub>/CTL samples, the MAPbI<sub>3</sub> layer was grown first on glass substrates and then CTL films were deposited following the same

procedures as described above (Figure 9, stage 2). The best CTLs revealed after stages 1 and 2 were tested further in completed solar cell stacks (Figure 9, stage 3).

#### *Aging experiment*

All prepared samples were placed in a specially designed aging chamber integrated into MBraun glove box. White light with  $50 \text{ mW/cm}^2$  intensity was provided by metal-halide lamps, which usually give a decent match with the solar AM1.5G spectra. For perovskite material, the mismatch of  $J_{\text{SC}}$  gained from AM1.5 G and metal halide lamp spectra is 22%. The sample temperature during the experiments was  $45 \pm 3$  °C.

#### *Device fabrication*

The n-i-p ITO/SnO<sub>2</sub>/MAPbI<sub>3</sub>/spiro-OMeTAD and p-i-n ITO/PEDOT:PSS/MAPbI<sub>3</sub>/ETL (ETL: PC<sub>61</sub>BM or PC<sub>71</sub>BM) samples were prepared following standard procedures.<sup>51</sup> The SnO<sub>2</sub> nanoparticle ink was purchased from Alfa Aesar, while spiro-OMeTAD was doped with LiTFSI and tBuPy following standard procedures.<sup>57</sup> The aforementioned multilayered stacks without top electrodes were exposed to light soaking under the same conditions as specified above. After completion of the aging period, the samples were processed to complete solar cell architectures by depositing Mg/Ag (20/80 nm) electrodes for p-i-n structures and Au/Ag (20/80 nm) electrodes for n-i-p structures. Electrodes were evaporated in high vacuum ( $10^{-5}$ - $10^{-6}$  mbar) through a shadow mask defining the active area of each device as  $0.16 \text{ cm}^2$ .

#### *Solar cell characterization*

The current-voltage characteristics of the devices were measured using Advantest 6240A source-measurement unit under the simulated  $100 \text{ mW/cm}^2$  AM1.5G solar irradiation provided Newport Verasol AAA class solar simulator. The intensity of the illumination was adjusted using a reference silicon diode of a known spectral response.  $J_{\text{SC}}$  values were reconfirmed by integrating the external quantum efficiency (EQE) spectra against the standard AM1.5G spectrum. The EQE spectra were measured using a PV Instruments system integrated with MBraun glove box.

### *Characterization techniques:*

#### UV-visible spectroscopy

Each sample was analyzed with UV-vis spectroscopy measurements to observe the evolution of the film absorbance due to some degradation, e.g. photobleaching effects. UV-vis spectra were measured in the range of 350-900 nm in an inert atmosphere using AvaSpec-2048-2UV-VIS fiber spectrometer integrated with MBraun glove box. UV-vis spectroscopy is a useful tool for quick estimation of film stability and a rough estimation of the presence of the perovskite phase. However, it does not provide sufficient data to understand the chemical composition of the degraded samples.

#### X-ray powder diffraction

X-ray diffraction analysis is a useful tool that allows observing crystal phases present in the studied systems. X-ray diffraction patterns were collected using a Bruker D8 instrument with a Cu K $\alpha$  source. Thin-film measurements were carried out in a fixed illumination mode with no sample stage rotation in the range of 5-60 2 $\Theta$  degrees. Based on the XRD data, we could make a conclusion on the presence and amount of different perovskite phases, PbI<sub>2</sub>, and metallic Pb in degraded samples. Note that amorphous phases cannot be confidently registered with XRD.

#### Atomic force microscopy

Cypher ES microscope (Asylum Research, CA) was used to measure the topography and surface potential of the samples in a tapping mode under dry inert Ar atmosphere in an MBraun glovebox with O<sub>2</sub> and H<sub>2</sub>O concentrations <0.1 ppm. The samples were grounded through the ITO with conductive silver paint. With the help of AFM, we could observe the change in grain size over aging time as well as the formation of light-induced defects.

#### X-ray photoelectron spectroscopy

X-ray photoelectron spectroscopy (XPS) measurements were carried out using a PHI XPS 5000 Versaprobe spectrometer (ULVAC Physical Electronics, USA) with a spherical quartz monochromator and an energy analyzer working in the range of binding energies (BE) from 0 to 1500 eV. The energy resolution  $\Delta E$  was  $\leq 0.5$  eV. The samples

were kept in the vacuum chamber for 24 h prior to the experiments and were measured at a pressure of  $10^{-7}$  Pa.<sup>37</sup>

#### ToF-SIMS analysis

ToF-SIMS measurements were performed using ToF-SIMS 5-100P Instrument (ION-TOF GmbH, Germany, 2007). The profiles were gained with  $\text{Cs}^+$  (positive ion detection mode) and  $\text{O}_2^-$  (negative ion mode) ion beams at 2000 eV ion energy and 480 nA measured sample current with the mass resolution  $>7000$  ( $m/\delta m$ ). The scanning was performed in the area of  $500 \times 500 \mu\text{m}^2$ . The collected data was analyzed and represented in a form of images with resolution 256x256 pixels.

### **2.3 Photostability of MAPbI<sub>3</sub>**

Before studying the perovskite/CTL interfaces, we explored the photochemical stability of the reference bare glass/MAPbI<sub>3</sub> samples. MAPbI<sub>3</sub> was used as a benchmark absorber material, which allows for a relatively fast assessment of the degradation effects occurring in the system, particularly, at the perovskite/CTL interfaces. We assumed that the glass substrate is mostly chemically inert with respect to the perovskite films and does not affect their stability under light exposure. The performed experiments allowed us to evaluate the MAPbI<sub>3</sub> degradation rate in the absence of any adjacent charge-transport layer. Both UV-vis and XRD data revealed that MAPbI<sub>3</sub> film undergoes a rapid decomposition under light exposure. In particular, the characteristic perovskite band at 750 nm is disappearing in optical spectra. XRD data (Figure 10b) evidenced that light induces the decomposition of MAPbI<sub>3</sub> into PbI<sub>2</sub> with further decay to metallic Pb. Figure 10c shows a diagram, which visualizes the evolution of the phase composition of the films in the course of aging. The percentage of each phase was estimated by considering a relative contribution of the analyzed component to the total integral peak intensity at the XRD pattern. This method might be not fully precise with respect to the real quantitative composition of the samples since it does not account for the presence of amorphous components. However, it provides very valuable qualitative information on the aging behavior of perovskite films. It was not possible to perform quantitative analysis using the Rietveld method, which works well for crystalline

powders. However, analyzing degraded thin lead halide perovskite films with this method leads to significant inaccuracies due to high texture factors, the overlap of some peaks, and a considerable amount of amorphous components.

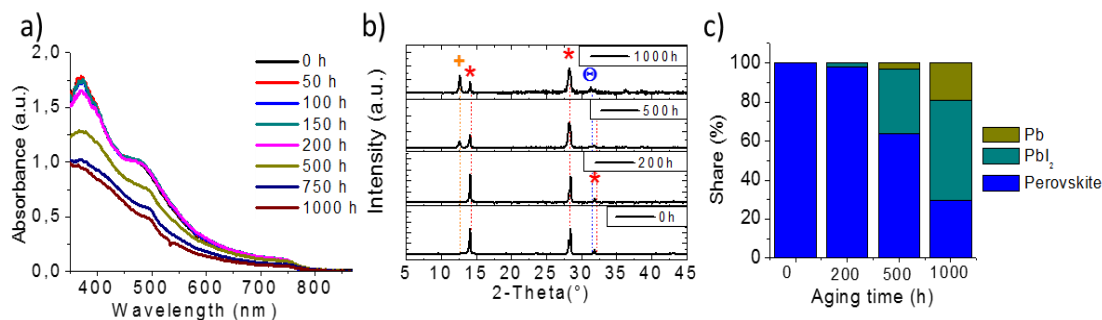


**Figure 10.** Evolution of the UV-vis spectra (a), XRD patterns (b), and phase composition (c) of the glass/ MAPbI<sub>3</sub> samples under continuous light soaking. ( $50\pm 2$  mW/cm<sup>2</sup>,  $45\pm 1$  °C). Symbols at XRD patterns denote the peaks of PbI<sub>2</sub> (+), MAPbI<sub>3</sub> (\*), and Pb0 (⊖) phase.

Figure 10c shows that the amount of MAPbI<sub>3</sub> is gradually decaying, while the formation of PbI<sub>2</sub> and metallic Pb is observed after 200 h and 500 h of light soaking, respectively.

Notably, ~70% of the crystalline material is represented by the perovskite decomposition products after 1000 h, which illustrates poor photochemical stability of MAPbI<sub>3</sub>. The obtained results are fully consistent with the previous publication reporting low intrinsic thermal and photochemical stability of MAPbI<sub>3</sub>.<sup>35</sup>

## 2.4 Impact of CTL underlayers on the photochemical stability of MAPbI<sub>3</sub>

Organic CTL material deposited between the perovskite film and glass substrate can affect significantly the degradation rate of MAPbI<sub>3</sub> under light soaking. Our choice of the model CTL materials for this study was motivated by the following. Among hundreds of HTLs reported for PSCs, spiro-OMeTAD is the most frequently used one since it delivers high efficiencies in devices.<sup>20,109</sup> Common ETL materials for p-i-n PSCs are based on C<sub>60</sub> and C<sub>70</sub> fullerene derivatives such as phenyl-C<sub>61</sub>-butyric acid methyl ester (PC<sub>61</sub>BM)<sup>110,111</sup> and phenyl-C<sub>71</sub>-butyric acid methyl ester (PC<sub>71</sub>BM).<sup>48,112</sup> They

have relatively good charge carrier mobilities, optimally aligned frontier energy levels with respect to the perovskite absorber and excellent film formation properties. At the same time, a great success was achieved in organic photovoltaics by using rylene diimides, such as perylene diimide (PDI)s<sup>113,114</sup> and naphthalene diimide (NDI)s<sup>115,116</sup> derivatives as non-fullerene acceptors (NFAs). It is reasonable to assume that many of the NFAs working well in organic solar cells can be also successfully utilized as ETLs in PSCs. Recent examples of using ITIC derivatives in PSCs support this conclusion.<sup>117</sup> The aforementioned arguments justify the choice of 5 different CTL materials involved in this study: PC<sub>61</sub>BM, PC<sub>71</sub>BM, NDI, PDI, and spiro-OMeTAD (Figure 11).

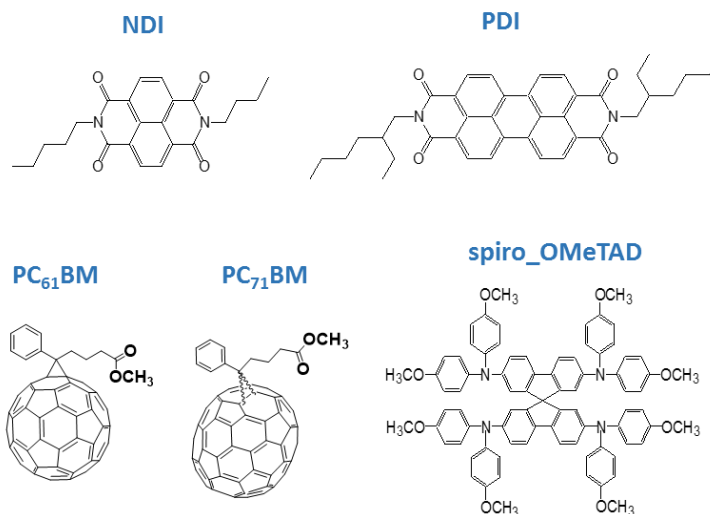


**Figure 11.** CTL chemical formulas: NDI, PDI, PC<sub>61</sub>BM, PC<sub>71</sub>BM, Spiro-OMeTAD.

There are some reports suggesting that the stability of perovskite films depends on the grain size, i.e. the larger the grains, the more stable is the film of the material.<sup>118</sup> Such a trend is fully justified with respect to the ambient stability since a decrease in the size of the grains increases significantly the material's surface area, where perovskite is in contact with aggressive species such as oxygen and moisture. In contrast, we found no significant impact of the grain size on the kinetics of the intrinsic light-induced perovskite decomposition.<sup>119</sup> AFM and SEM analysis showed that pristine MAPbI<sub>3</sub> films grown on different substrates have a uniform structure with an average grain size of 0.1–0.15  $\mu\text{m}$  and an RMS roughness of 10 nm (Figure 12 and Figure 13). Therefore,

some specific interfacial interactions between the perovskite and CTLs provide the strongest contribution to the films' degradation kinetics rather than the perovskite film morphology itself.

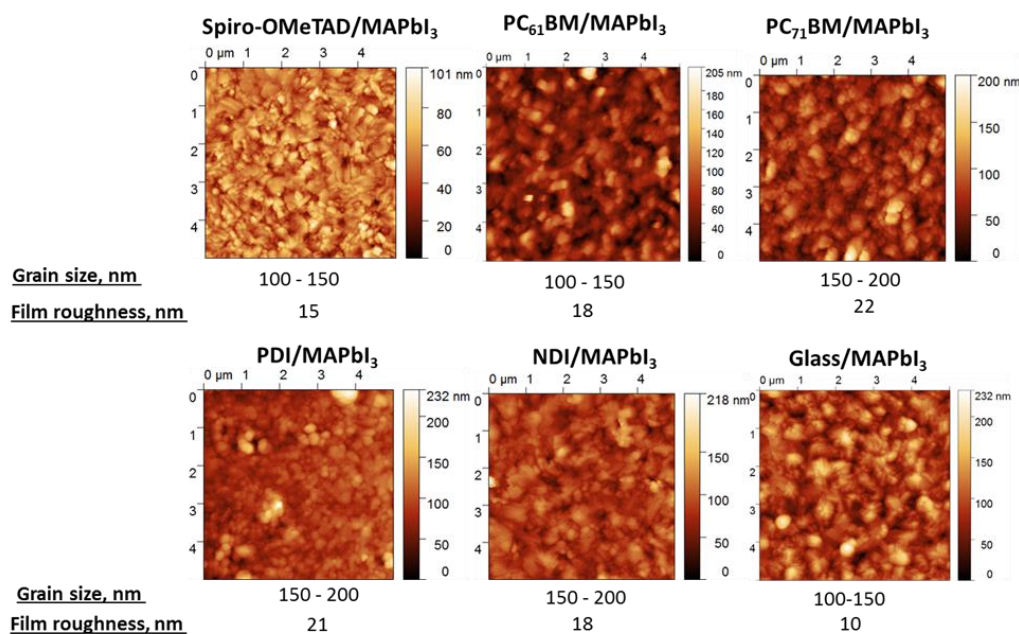


**Figure 12.** Surface topography for the samples with CTL/MAPbI<sub>3</sub> configuration before light soaking.

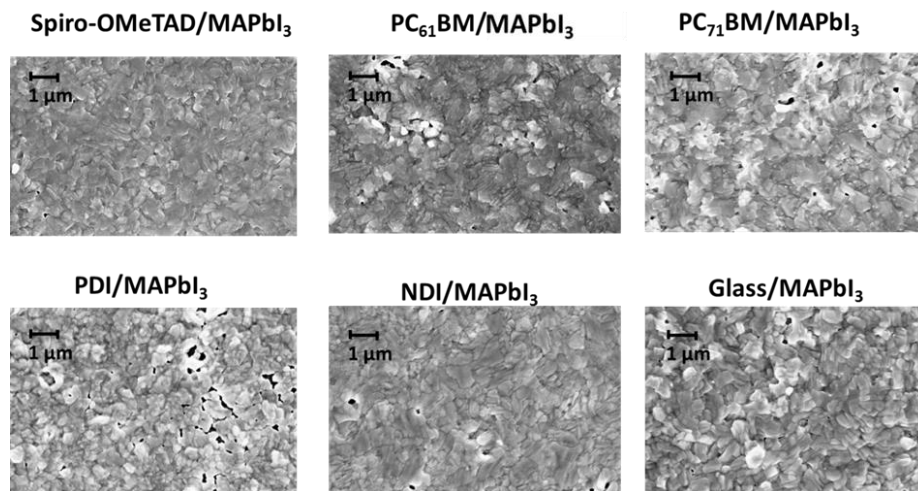


**Figure 13.** SEM images of the samples with CTL/MAPbI<sub>3</sub> configuration before light soaking.

Figure 14 gives an overview of the evolution of the absorption spectra, XRD patterns, and phase compositions of all studied CTL/perovskite systems. All samples

were subjected to the light soaking ( $50\pm 2$  mW/cm<sup>2</sup>) in the inert atmosphere. Interestingly, some charge transport layers accelerate perovskite degradation, while others slow down the photodecomposition of MAPbI<sub>3</sub>.

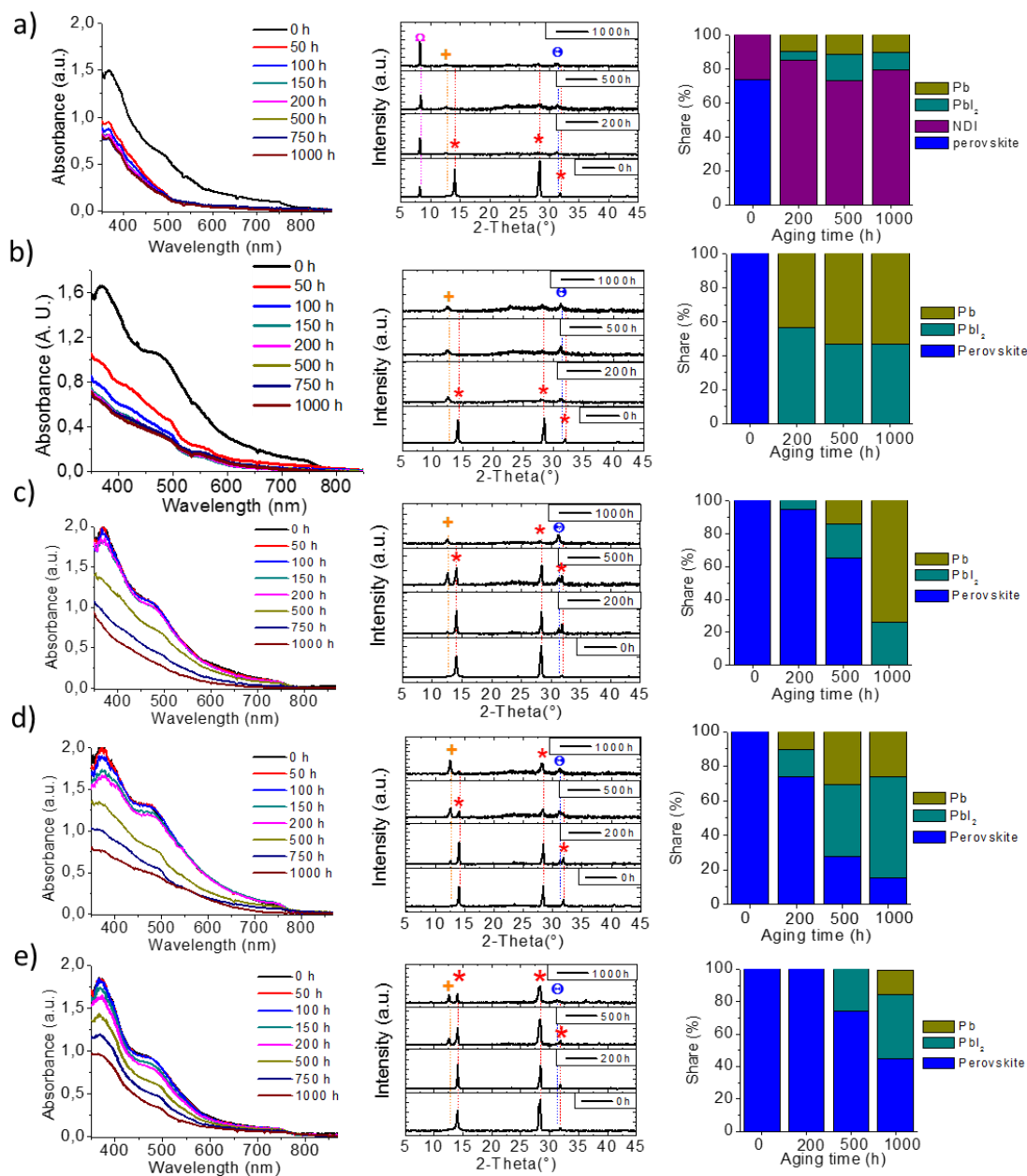
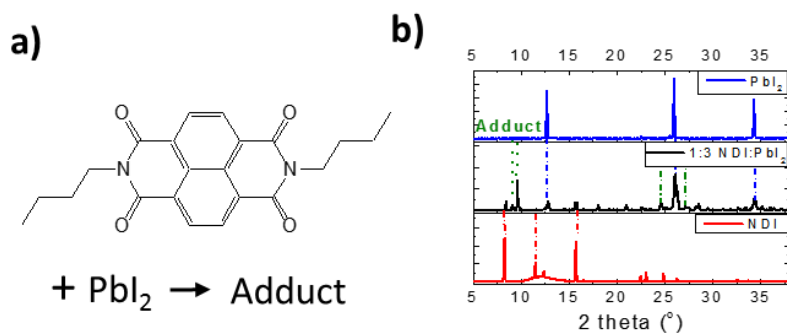


**Figure 14.** Absorption spectra (left), XRD patterns (middle) and phase composition diagrams (right) for glass/NDI/MAPbI<sub>3</sub> (a), glass/PDI/MAPbI<sub>3</sub> (b), glass/PC<sub>61</sub>BM/MAPbI<sub>3</sub> (c), glass/PC<sub>71</sub>BM/MAPbI<sub>3</sub> (d) and glass/spiro-OMeTAD/MAPbI<sub>3</sub> (e) stacks. ( $50\pm 2$  mW/cm<sup>2</sup>,  $45\pm 1$  °C). Symbols at XRD patterns denote the peaks of PbI<sub>2</sub> (+), MAPbI<sub>3</sub> (\*), Pb<sup>0</sup> (⊕), and NDI (⊖) phase.

Among the first group, PDI and NDI were the strongest promoters of perovskite degradation. Glass/NDI/perovskite stacks show no perovskite phase already after 20 h of light soaking according to the UV-vis data (Figure 14a). XRD analysis of this system provided very interesting results. NDI phase (peak at  $8.5^\circ$ ) becomes dominating while increasing the exposure time, which might be suggesting either crystallization of this material or, most probably, amorphization of the perovskite film. Surprisingly, NDI strongly suppressed the formation of crystalline phases of  $\text{PbI}_2$  or metallic Pb so typical for  $\text{MAPbI}_3$  photodecomposition. Such unusual behavior indicates the presence of some specific interactions between NDI and the perovskite degradation products. Most likely, a part of NDI reacts with  $\text{PbI}_2$  forming some mostly amorphous adduct (Scheme 1), which is not detectable by XRD. In order to verify this hypothesis, we dissolved NDI and  $\text{PbI}_2$  (1:3 ratio) in DMF and then evaporated the solvent. XRD analysis of the dried powder (Scheme 1) showed the presence of both NDI and  $\text{PbI}_2$  phases along with a number of other peaks, which can be tentatively assigned to the  $\text{PbI}_2$ -NDI adduct.



**Scheme 1.** Schematic illustration of some chemical interactions between NDI and  $\text{PbI}_2$  leading to an adduct formation (a) and the XRD pattern for a powder of NDI- $\text{PbI}_2$  blend (b).

The co-existence of the adduct with the pure components ( $\text{PbI}_2$  and NDI) did not allow us to obtain single crystals of the adduct and identify its structure by x-ray diffraction analysis. However, with respect to understanding the perovskite aging behavior, identifying an exact structure of this adduct is much less important than the

fact of its formation. It is known that MAPbI<sub>3</sub> has low formation energy and, therefore, can easily dissociate to MAI and PbI<sub>2</sub> under elevated temperatures or light soaking.<sup>63</sup>

Binding of PbI<sub>2</sub> to NDI with the adduct formation shifts the thermodynamic equilibrium in the system and accelerates the decomposition of the perovskite films. Considering the fact that PDI has the same functional groups as NDI, it is reasonable to assume that it can also form some adducts with PbI<sub>2</sub>. Indeed, the glass/PDI/MAPbI<sub>3</sub> system (Figure 14b) shows essentially the same degradation behavior as glass/NDI/MAPbI<sub>3</sub> stacks (Figure 14a). These two examples reveal the importance of specific interactions between the CTL molecules and perovskite or its decomposition products. In this particular case, these interactions strongly promote the light-induced breakdown of MAPbI<sub>3</sub>. However, we believe that careful (supra)molecular engineering might help to develop CTLs, which stabilize the perovskite phase via some specific interactions.

The CTLs based on the fullerene derivatives did not affect the stability of MAPbI<sub>3</sub> as dramatically as it was observed in the case of using NDI and PDI. Glass/PC<sub>61</sub>BM/MAPbI<sub>3</sub> and glass/PC<sub>71</sub>BM/MAPbI<sub>3</sub> stacks showed relatively slow degradation kinetics under continuous light soaking.

For instance, ca. 60% of perovskite phase survived in glass/PC<sub>61</sub>BM/MAPbI<sub>3</sub> samples after 500 h of light exposure. However, complete decomposition of MAPbI<sub>3</sub> to PbI<sub>2</sub> and Pb(0) was observed after 1000 h (Figure 14c). The glass/PC<sub>71</sub>BM/MAPbI<sub>3</sub> system showed better stability demonstrating the presence of ~15% of crystalline MAPbI<sub>3</sub> after 1000 h under the same aging conditions (Figure 14d).

It should be emphasized that glass/spiro-OMeTAD/MAPbI<sub>3</sub> stacks represent the only system that showed somewhat similar stability than the reference samples based on perovskite films deposited directly on bare glass (Figure 14e). Over 40% of the crystalline MAPbI<sub>3</sub> phase survived after 1000 h of light soaking, while the reference samples showed only 30% of this phase remaining. This observation suggests that spiro-OMeTAD films provide even more inert substrate interface for the perovskite films than the bare glass. The comparison of all five glass/CTL/MAPbI<sub>3</sub> systems based on the

photobleaching kinetics of their films is presented in Figure 15. These results also support the conclusion that spiro-OMeTAD underlayer slows down the perovskite degradation as compared to the reference films, while all other CTLs promote the MAPbI<sub>3</sub> decomposition.

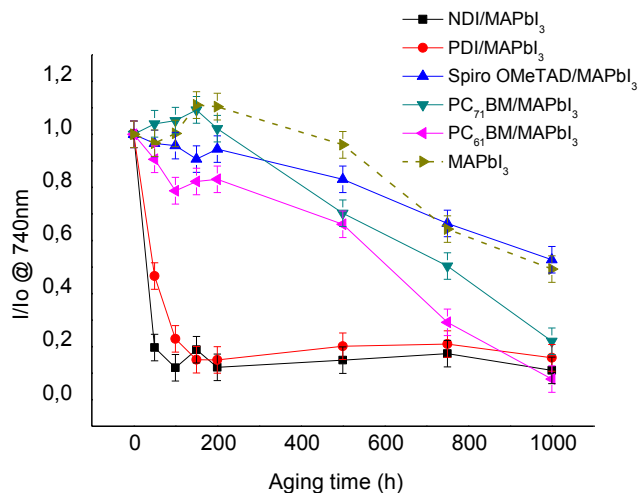


**Figure 15.** Evolution of the optical density of glass/CTL/MAPbI<sub>3</sub> stacks at 700 nm ( $I_0$  stands for initial optical density at this wavelength).

Additional insight into the degradation behavior of all glass/CTL/perovskite stacks was gained with the use of x-ray photoelectron spectroscopy (XPS). The XPS survey spectra of glass/CTL/MAPbI<sub>3</sub> samples before and after light soaking are presented in Table 1 and Figure 16e, f. Pristine MAPbI<sub>3</sub> rapidly degrades and already after 200 h of light soaking N content and N:Pb ratio drops down to 0. I/Pb ratio also goes down with more than twice a reduction in iodine content after 1000h of light soaking. A similar trend was observed for the glass/Spiro-OMeTAD/MAPbI<sub>3</sub> sample with a slightly lower iodine loss rate. Moreover, this system demonstrates the smallest high-energy shift of the Pb 4f<sub>7/2</sub> band in the course of light-induced aging within up to 1000 h, which indicates suppressed formation of the PbI<sub>2</sub> phase (Figure 16c, d).

Surface composition for the glass/PC<sub>61</sub>BM/MAPbI<sub>3</sub> and glass/PC<sub>71</sub>BM/MAPbI<sub>3</sub> stacks are nearly the same as for pristine MAPbI<sub>3</sub> considering the complete absence of nitrogen and ~3-fold reduction in the I:Pb ratio after 1000 h of light soaking. An interesting comparison can be also drawn from the full width of Pb 4f<sub>7/2</sub> band measured

at half of the intensity maximum (FWHM) and the energy position of this band (Figure 16c, d). Importantly, there was no change in the FWHM for glass/PC<sub>61</sub>BM/MAPbI<sub>3</sub> samples up to 200 h of light exposure, while after 1000 h of light soaking it increased only by ~10% (Figure 16c). However, there is a high-energy shift of the Pb 4f<sub>7/2</sub> band by ~0.19-0.20 eV after 200 h and by ~0.34-0.40 eV after 1000 h of aging, which clearly indicates the formation of PbI<sub>2</sub> phase.

**Table 1.** Surface composition (in at.%) of glass/CTL/MAPbI<sub>3</sub> samples estimated from XPS spectra.

Configuration	Aging time (h)	Surface composition (at. %)			Element ratio	
		N	Pb	I	I:Pb	N:Pb
MAPbI <sub>3</sub>	0	6.8	9.5	25.3	2.7	0.7
	200	6.2	11	26.5	2.4	0.6
	500	0	14.8	21.1	1.4	0
	1000	0	15.5	19.9	1.2	0
Spiro-OMeTAD/ MAPbI <sub>3</sub>						0.8
MAPbI <sub>3</sub>	0	7.7	9.6	25.1	2.6	
	200	7.8	10.8	24.4	2.3	0.7
	500	0	15.2	24.7	1.6	0
	1000	0	13.2	19.1	1.4	0
PC <sub>61</sub> BM/MAPbI <sub>3</sub>	0	4.1	4.3	11.9	2.8	0.9
	200	3.8	15.6	32.2	2.1	0.2
	500	0	0.1	0.2	1.0	0
	1000	0	6.8	6.7	0.9	0
PC <sub>71</sub> BM/MAPbI <sub>3</sub>	0	3.8	5.7	12.7	2.2	0.7
	200	5.7	11.8	24.0	2.0	0.5
	500	0	13.5	19.1	1.4	0
	1000	0	7.3	6.4	0.9	0
NDI/MAPbI <sub>3</sub>	0	6.1	9.7	23.8	2.4	0.6
	200	3.1	12	14.3	1.2	0.3
	500	1.7	7.4	16.3	2.2	0.2
	1000	0.9	11.1	14.4	1.3	0.1
PDI/MAPbI <sub>3</sub>	0	7.5	8.6	21.7	2.5	0.9
	200	0	16.1	17.2	1.1	0
	500	0	10.3	13.1	1.3	0
	1000	0	8.6	12.5	1.4	0

A similar trend was observed for glass/PC<sub>71</sub>BM/MAPbI<sub>3</sub> stacks. These results suggest that fullerene derivatives somehow suppress the formation of metallic lead (at

least on film surface) from MAPbI<sub>3</sub> under light soaking conditions, while PbI<sub>2</sub> becomes a predominant decomposition product.

In the case of glass/NDI/MAPbI<sub>3</sub> stacks, the nitrogen content on the film surface gradually decreases from 6.1% to 0.9% (note that NDI also has nitrogen) with the aging time going up to 1000 h. At the same time, I:Pb atomic ratio for this system also decreases from ~2.45 for fresh films down to 1.29 for the samples after 1000 h of light soaking. XPS data suggest that glass/PDI/MAPbI<sub>3</sub> undergoes even faster degradation upon light exposure.

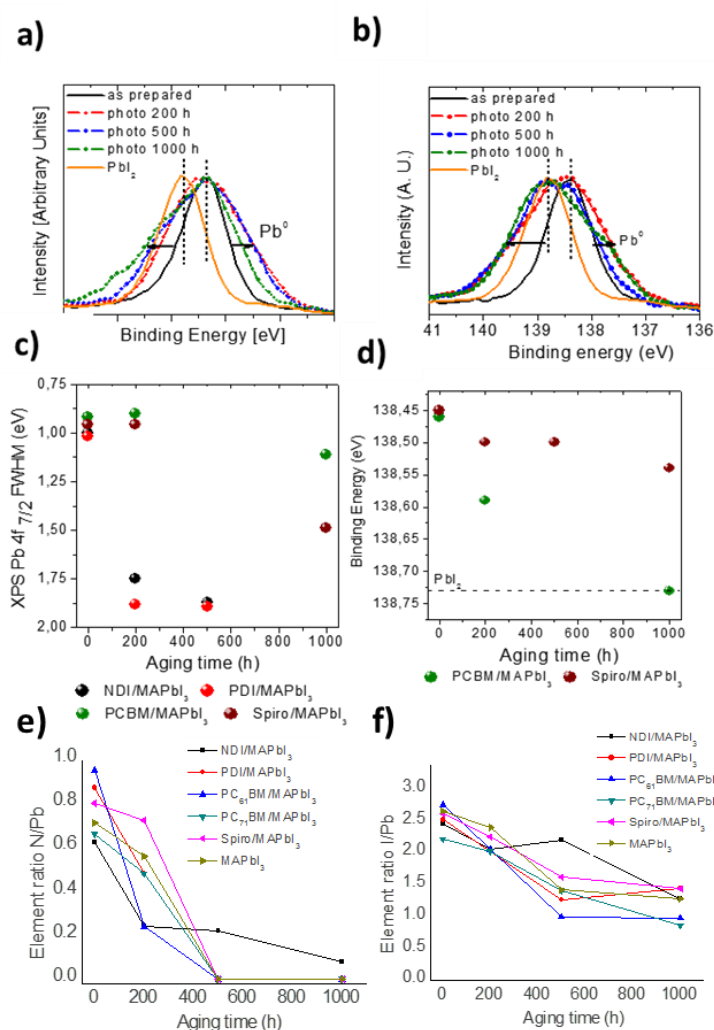
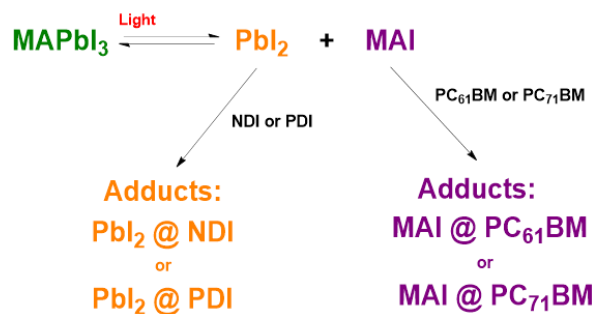


**Figure 16.** XPS Pb 4f7/2 bands for NDI/MAPbI<sub>3</sub>(a) and PDI/MAPbI<sub>3</sub>(b) samples. The comparison of XPS Pb 4f7/2 band FWHM (b) and binding energy (c) evolution under aging for different systems. I/Pb (e) and N/Pb (f) element ratio of CTL/MAPbI<sub>3</sub> samples estimated from XPS spectra.

The nitrogen content decreases to zero already after 200 h of light soaking, while the I:Pb ratio falls from 2.52 to 1.45. It should be noticed that XPS Pb 4f<sub>7/2</sub> spectra of the glass/NDI/MAPbI<sub>3</sub> and glass/PDI/MAPbI<sub>3</sub> (Figure 16a, b) samples show strong band broadening in two directions: towards the high energies to match the PbI<sub>2</sub> band and towards the low energies thus featuring the formation of metallic lead. Thus, the obtained XPS data confirm that MAPbI<sub>3</sub> films deposited atop of NDI or PDI underlayers undergo facile light-induced degradation while losing organic cations and forming PbI<sub>2</sub> and metallic Pb.

To summarize this part, we want to emphasize that the nature of the CTL underlayer significantly affects the photostability of the perovskite films. Some materials such as rylene diimides severely accelerate MAPbI<sub>3</sub> decomposition due to their specific interactions with the PbI<sub>2</sub> formed as perovskite aging products. Fullerene derivatives PC<sub>61</sub>BM and PC<sub>71</sub>BM also promote decomposition of MAPbI<sub>3</sub> since they form adducts with MAI, which is another perovskite decomposition product.<sup>51</sup> This behavior can be understood considering the fact that bonding of MAI with PbI<sub>2</sub> within the perovskite lattice is rather weak and MAPbI<sub>3</sub> can reversibly dissociate to MAI and PbI<sub>2</sub>. If one of the decomposition products is absorbed by CTL or forms some adducts, the equilibrium shifts to the right, and perovskite undergo massive decomposition (Scheme 2). Note, that the experiment was performed under light soaking conditions at 45 °C. The same test in the dark did not reveal any decomposition of MAPbI<sub>3</sub>, thus we can conclude that MAPbI<sub>3</sub> degradation followed by adduct formation has a photochemical nature.



**Scheme 2.** Impact of specific interactions between PbI<sub>2</sub> or MAI with CTL material on the decomposition of MAPbI<sub>3</sub>.

On the contrary, other materials such as spiro-OMeTAD do not react with either MAI or  $\text{PbI}_2$  and, therefore, provide the most stable interface with the deposited above the perovskite layer while slowing down its decomposition. Thus, a careful design of the CTL/perovskite interfaces is a crucial point to deliver the desired operation lifetimes required for the practical implementation of perovskite photovoltaics.

## 2.5 Effect of CTLs as top coatings for $\text{MAPbI}_3$ thin films

The charge transport materials discussed in the previous section were also explored as coatings atop the perovskite films in the glass/ $\text{MAPbI}_3$ /CTL configuration. The obtained results are summarized in Figure 17. It was not surprising that NDI and PDI coatings accelerated the perovskite decomposition. These highly crystalline materials did not provide uniform coatings above the perovskite layer (Figure 18), which suggests that they can hardly block the evaporation of the volatile components from the  $\text{MAPbI}_3$  films in the course of their light-induced aging. At the same time, both NDI and PDI tend to form some adducts with  $\text{PbI}_2$ , which facilitates the decomposition of the perovskite under light soaking.

All other investigated CTLs formed uniform coatings above the perovskite films and increased substantially the lifetime of the  $\text{MAPbI}_3$  absorber under continuous light soaking conditions (Figure 19, Figure 20, Figure 21). Rather interesting results were obtained for the glass/ $\text{MAPbI}_3$ /spiro-OMeTAD system (Figure 17). According to the XRD data, the amount of  $\text{MAPbI}_3$  phase after 1000 h of light soaking was nearly the same as in the case of glass/spiro-OMeTAD/ $\text{MAPbI}_3$  samples with CTL underlayer.

Importantly, the degradation pathway has changed in favor of the formation of metallic lead rather than  $\text{PbI}_2$  observed in the case of glass/spiro-OMeTAD/ $\text{MAPbI}_3$  systems discussed above. The formation of metallic lead might be a consequence of the direct contact of the  $\text{MAPbI}_3$  degradation products, e.g.  $\text{PbI}_2$ , with spiro-OMeTAD. It is known that  $\text{PbI}_2$  can undergo photochemical decomposition to  $\text{I}_2$  and  $\text{Pb}(0)$ <sup>120</sup>, while electron-rich aromatic amines such as spiro-OMeTAD can absorb  $\text{I}_2$  and undergo doping. The proposed here  $\text{I}_2$  absorption by spiro-OMeTAD might be a driving force accelerating the decomposition of  $\text{MAPbI}_3$  to metallic lead.

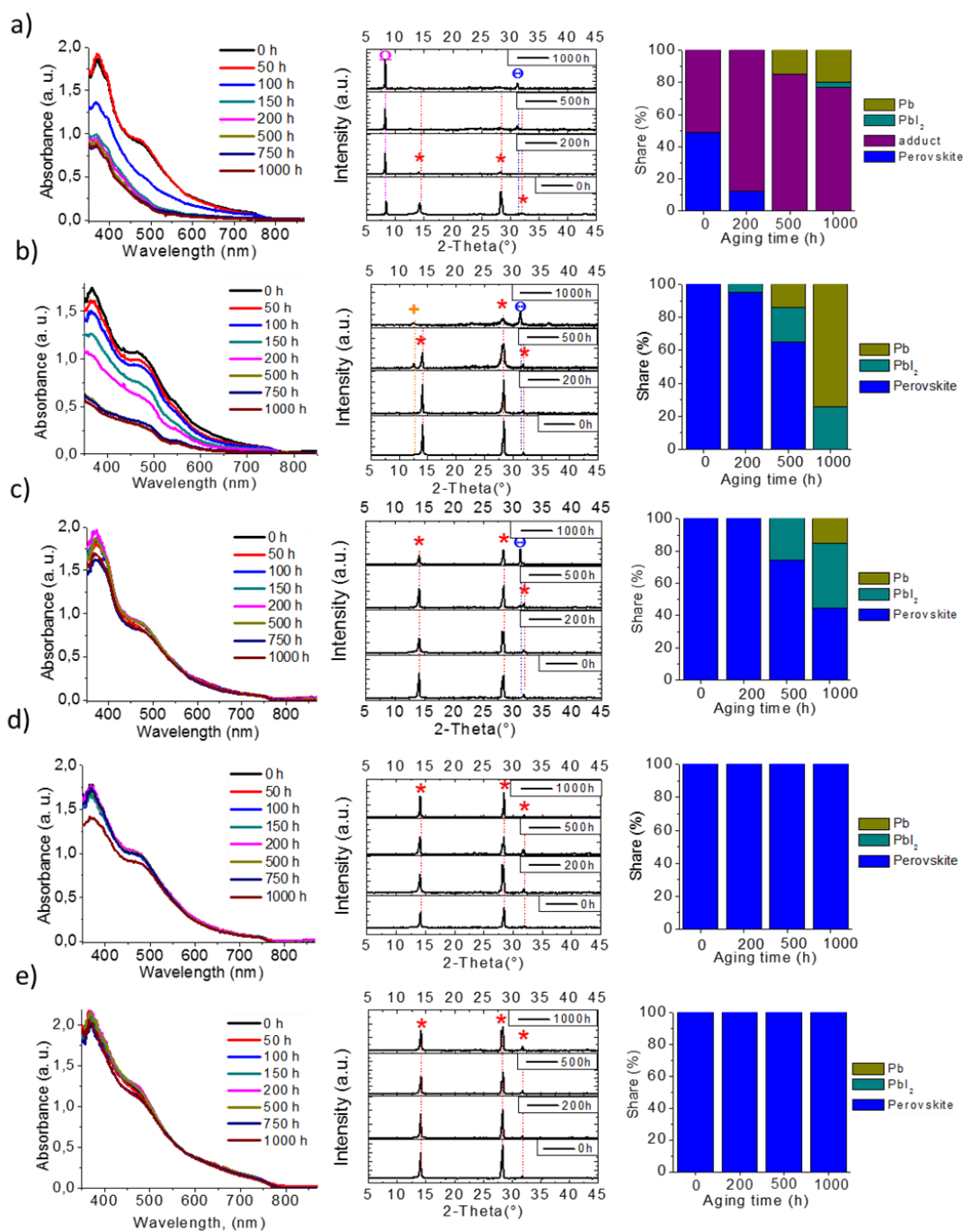


**Figure 17.** Absorption spectra (left), XRD patterns (middle) and phase composition diagrams (right) for glass/MAPbI<sub>3</sub>/NDI (a), glass/MAPbI<sub>3</sub>/PDI (b), glass/MAPbI<sub>3</sub>/Spiro-OMeTAD (c), glass/MAPbI<sub>3</sub>/PC<sub>71</sub>BM (d) and glass/MAPbI<sub>3</sub>/PC<sub>61</sub>BM (e) stacks. (50±2 mW/cm<sup>2</sup>, 45±1 °C). XRD pattern symbols: + PbI<sub>2</sub> phase; \*MAPbI<sub>3</sub> phase;  $\emptyset$  Pb(0) phase;  $\Omega$  NDI phase.

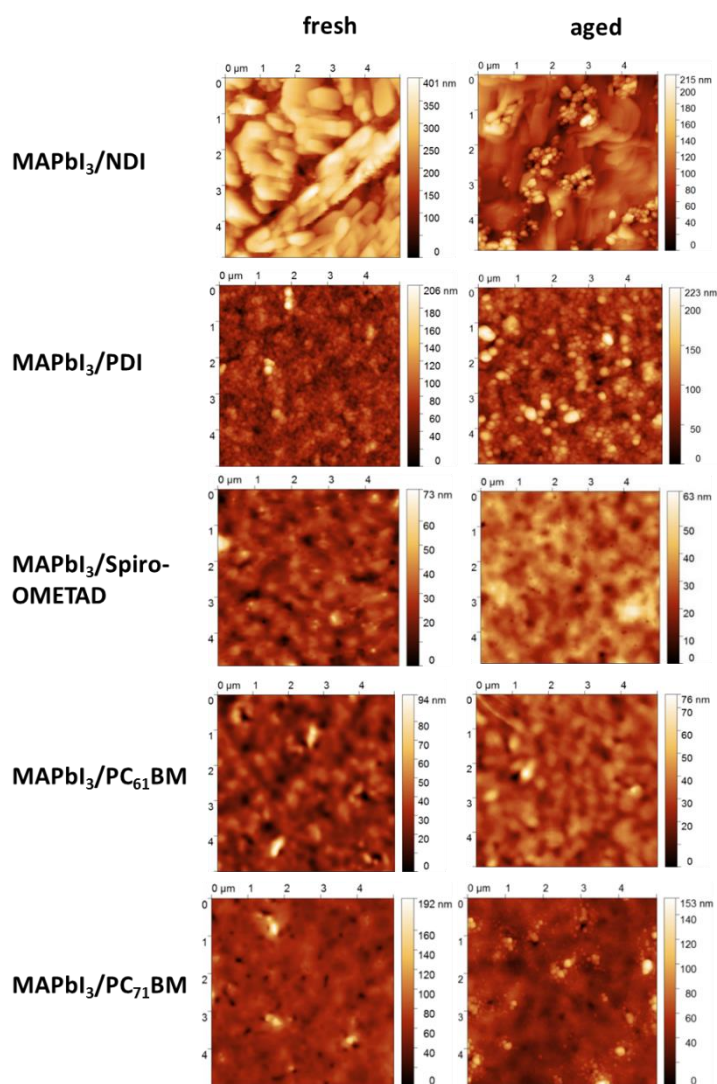


**Figure 18.** Surface topography of glass/MAPbI<sub>3</sub>/NDI, glass/MAPbI<sub>3</sub>/PDI, glass/MAPbI<sub>3</sub>/Spiro-OMETAD, glass/MAPbI<sub>3</sub>/PC<sub>71</sub>BM, and glass/MAPbI<sub>3</sub>/PC<sub>61</sub>BM films before and after 1000 h exposure to the light soaking.

Interestingly, spiro-OMETAD acts as a good encapsulation layer stabilizing the perovskite films for at least 500 h, while longer exposure to the light leads to the fast aging with the formation of Pb(0). It is known that spiro-OMETAD tends to crystallize under light soaking,<sup>56</sup> which might lead to the formation of grains and voids at the grain boundaries. These voids might provide some routes for evaporation of volatile

components from the perovskite layer thus ruining the encapsulation properties of spiro-OMeTAD upper coating.

Among all the CTL layers explored as top coatings above MAPbI<sub>3</sub> films, the fullerene derivatives showed the best encapsulation characteristics. Indeed, PC<sub>61</sub>BM and PC<sub>71</sub>BM films deposited above MAPbI<sub>3</sub> completely prevented its decomposition under light soaking conditions (Figure 17d, e). Both UV-vis and XRD data for these systems showed no signs of PbI<sub>2</sub> or Pb(0) formation. The revealed remarkable stabilization properties of the fullerene derivatives suggest that they form compact and uniform coatings above the perovskite grains, thus preventing loss of volatile species produced in the course of MAPbI<sub>3</sub> photochemical aging. Isolation of all degradation products inside the perovskite layer shifts the thermodynamic equilibrium in the desired direction and slows down the decomposition reactions.<sup>51</sup> This mechanism relying on the thermodynamic reversibility of the lead halide decomposition processes is apparently explaining the self-healing of the PSCs in the dark after they were degrading under light soaking conditions.<sup>41,121</sup> Moreover, fullerene derivatives are known to passivate perovskite grain boundaries eliminating in this way non-radiative recombination.<sup>122</sup> PCBM molecules can penetrate in the bulk of perovskite material and passivate Pb-I antisite defects or under-coordinated Pb<sub>2</sub><sup>+</sup> vacancies at grain boundaries.<sup>122</sup>

To summarize this section, we conclude that for the investigated series of glass/MAPbI<sub>3</sub>/CTL systems spiro-OMeTAD and, especially PC<sub>61</sub>BM and PC<sub>71</sub>BM showed the strongest stabilization effects on MAPbI<sub>3</sub> films due to their excellent encapsulation properties.

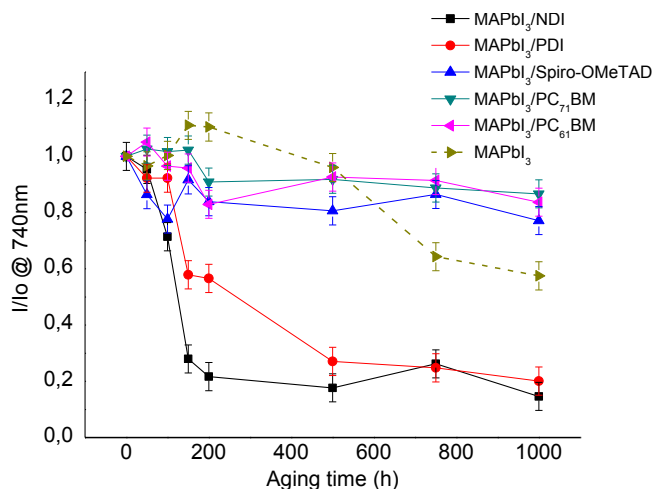


**Figure 19.** Evolution of the optical density of glass/MAPbI<sub>3</sub>/CTL stacks at 700 nm ( $I_0$  stands for initial optical density at this wavelength).

## 2.6 Effect of CTLs on device stability

In the previous section, we featured PC<sub>61</sub>BM and PC<sub>71</sub>BM as the most promising CTLs enhancing remarkably the photostability of MAPbI<sub>3</sub> films. However, these results might contradict with the conclusions of previous publication, where it was shown that PC<sub>61</sub>BM and PC<sub>71</sub>BM absorb MAI in the cavities between the fullerene spheres, which leads to a rapid failure of the photovoltaic cells.<sup>51</sup>

Here we revisited the stability of the ITO/PEDOT:PSS/ MAPbI<sub>3</sub>/ETL p-i-n device architectures (ETL: PC<sub>61</sub>BM or PC<sub>71</sub>BM) under continuous light soaking conditions. Considering the fact that the top electrode might also be responsible for a number of aging pathways, we exposed the electrode-free stacks ITO/PEDOT:PSS/MAPbI<sub>3</sub>/ETL to the illumination and evaporated the Mg/Ag electrodes just before the measurements (see details in 2.2 Materials and Methods). Figure 20 shows that the devices comprising PC<sub>61</sub>BM or PC<sub>71</sub>BM as ETLs strongly degraded within less than 20 h of light exposure, and after 40 h the efficiency drops down to almost zero.

Current-voltage characteristics of the degraded solar cells can be found in Figure 21 and Figure 22. Particularly fast degradation was observed for the solar cells with the PC<sub>61</sub>BM layer.  $J_{SC}$  dropped from  $\sim 15$  to  $\sim 4$  mA/cm<sup>2</sup> within the initial 15 h of light soaking. EQE measurements confirmed severe current losses Figure 23).

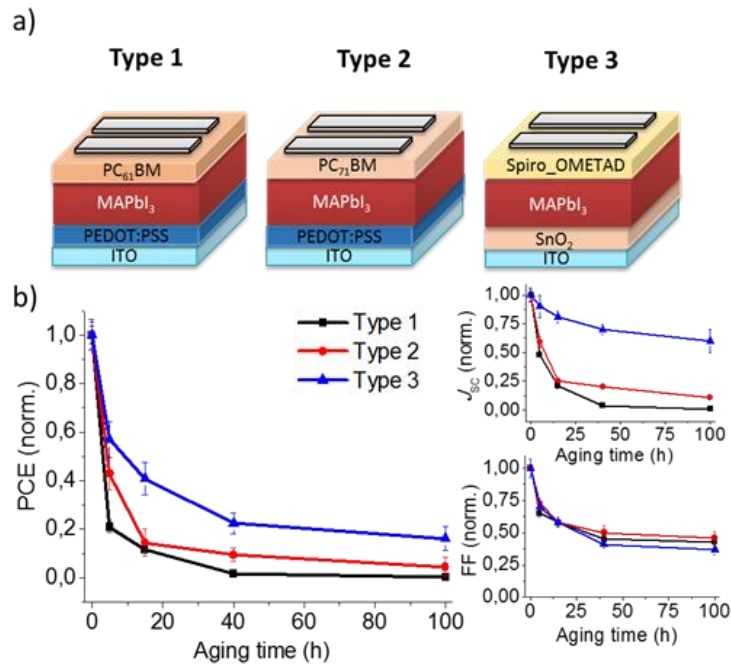


**Figure 20.** Structure of 3 types of studied solar cells (a) and evolution of their PCE,  $J_{SC}$ , and FF under light soaking conditions (b). Note that aging was performed before the top electrode deposition

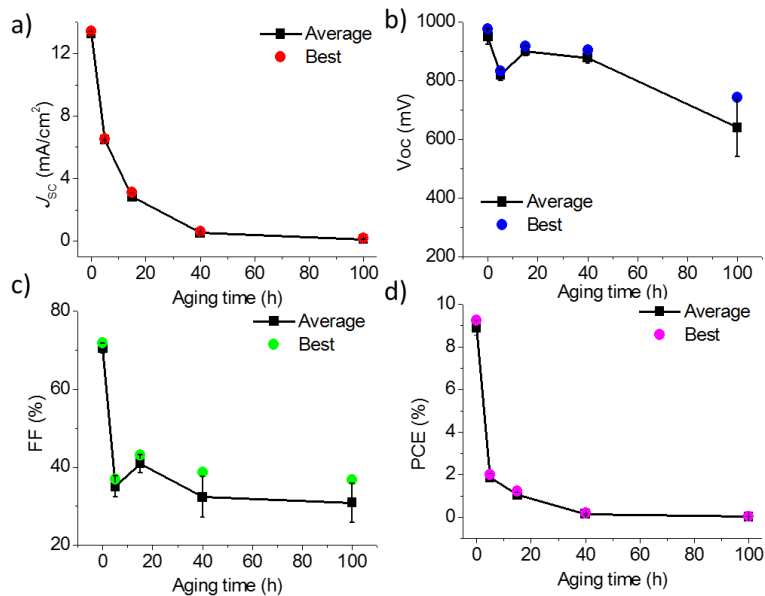


**Figure 21.** Evolution of the characteristics of ITO/PEDOT:PSS/MAPbI<sub>3</sub>/PC<sub>61</sub>BM/Mg/Ag solar cells under light soaking conditions applied to ITO/PEDOT:PSS/MAPbI<sub>3</sub>/PC<sub>61</sub>BM stacks:  $J_{SC}$  (a),  $V_{OC}$  (b), FF (c), PCE (d).

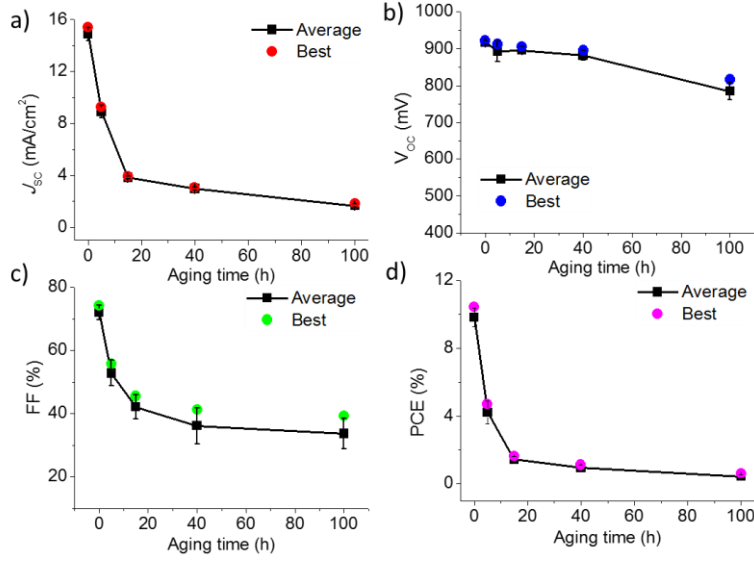


**Figure 22.** Evolution of the characteristics of ITO/PEDOT:PSS/MAPbI<sub>3</sub>/PC<sub>71</sub>BM/Mg/Ag solar cells under light soaking conditions applied to ITO/PEDOT:PSS/MAPbI<sub>3</sub>/PC<sub>71</sub>BM stacks:  $J_{sc}$  (a),  $V_{oc}$  (b), FF (c), and PCE (d).

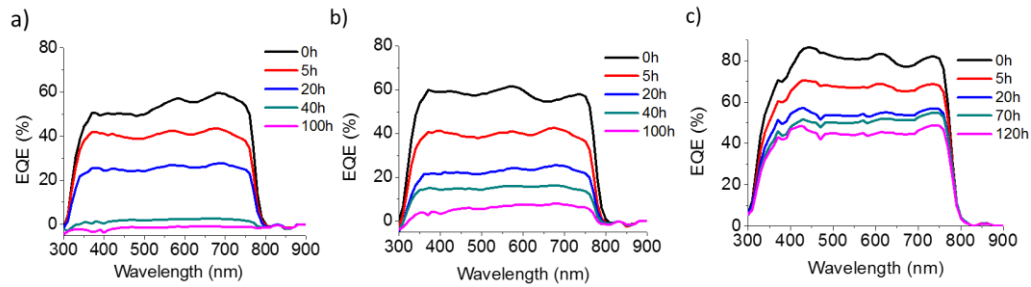


**Figure 23.** Evolution of EQE spectra of ITO/PEDOT:PSS/MAPbI<sub>3</sub>/PC<sub>61</sub>BM/Mg/Ag (a), ITO/PEDOT:PSS/MAPbI<sub>3</sub>/PC<sub>71</sub>BM/Mg/Ag (b) and ITO/SnO<sub>2</sub>/MAPbI<sub>3</sub>/spiro-OMeTAD/Ag/Au (c) solar cells fabricated using fresh and exposed to light soaking top electrode free stacks.

Such behavior is fully consistent with the previous observations<sup>51</sup> and does not match the excellent stability of the perovskite films encapsulated with either PC<sub>61</sub>BM or PC<sub>71</sub>BM. One might suspect that it is another interface, namely PEDOT:PSS/MAPbI<sub>3</sub>, which is responsible for the observed device degradation. However, replacing PEDOT:PSS with PTAA, which is one of the most chemically inert and robust HTL materials, does not influence the degradation trend (Figure 24).

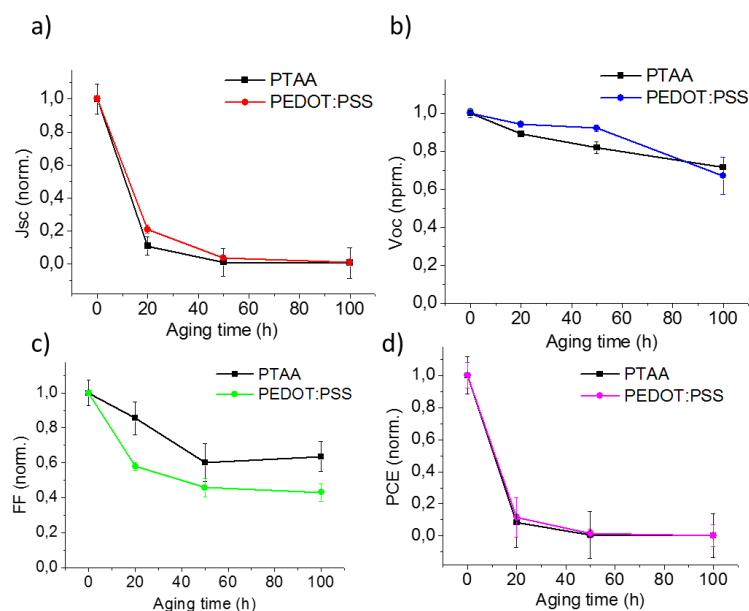


**Figure 24.** Comparison of the degradation behavior of ITO/PEDOT:PSS/MAPbI<sub>3</sub>/PC<sub>61</sub>BM/Mg/Ag and ITO/PTAA/MAPbI<sub>3</sub>/PC<sub>61</sub>BM/Mg/Ag solar cells under light soaking conditions applied to the electrode-free stacks:  $J_{SC}$  (a),  $V_{OC}$  (b), FF (c), and PCE (d).

Note also that the efficiency of devices with PTAA used as HTL comes close to 16%, which is a decent value for p-i-n PSCs, which were not optimized for reaching the ultimate performance. This suggests also that MAPbI<sub>3</sub> films have acceptable quality and bulk defects in the perovskite films should not affect dramatically their degradation behavior. Therefore, the obtained results lead to the conclusion that the fullerene-based electron transport layer is mainly responsible for the degradation at least within the presented timescale.

Thus, even though PC<sub>61</sub>BM and PC<sub>71</sub>BM can encapsulate and stabilize the MAPbI<sub>3</sub> films with respect to their bulk aging, interfacial degradation ruins their performance in devices. It should be also noted that the adsorption of MAI in PC<sub>61</sub>BM layer at the perovskite/ETL interface can hardly be detected by UV-vis or XRD measurements due to the limited sensitivity of these techniques. Considering the impressive perovskite film stabilization effects demonstrated here for PC<sub>61</sub>BM and PC<sub>71</sub>BM, future efforts should be focused on preventing the MAI absorption in the fullerene-based ETLs while maintaining their charge transport characteristics.

Notably, the n-i-p solar cells with ITO/SnO<sub>2</sub>/MAPbI<sub>3</sub>/spiro-OMeTAD/Au configuration also showed low operation stability even though gold electrodes were deposited just before measurements as described above for p-i-n cells. The PCE decreased rapidly approaching ~2% after 100 h of light soaking (Figure 25). It is known that the SnO<sub>2</sub> layer might also contribute to device degradation, while the major effect, we believe, still comes from the top HTL layer. As a proof, solar cells fabricated with TiO<sub>x</sub> bottom ETL and spiro-OMeTAD top HTL demonstrated a similar degradation behavior. Therefore, we assume that spiro-OMeTAD layer is mostly responsible for the observed device aging, while the impact of the oxide ETLs also should not be neglected.

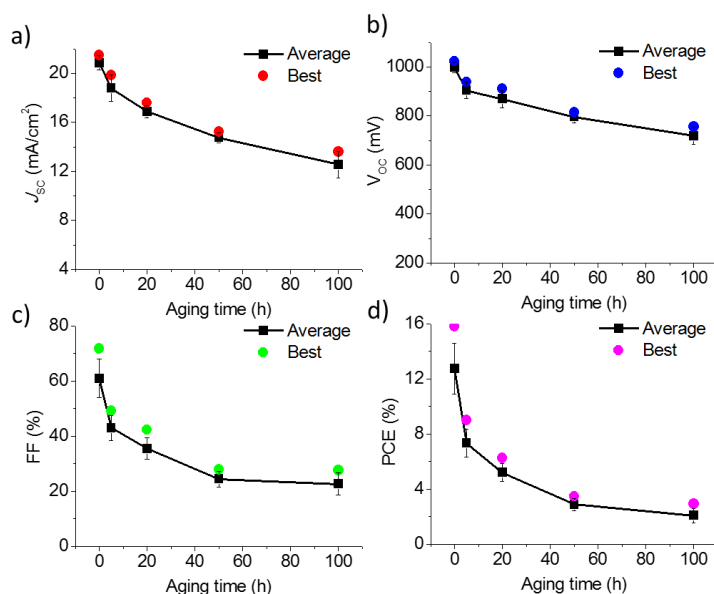


**Figure 25.** Evolution of the characteristics of ITO/SnO<sub>2</sub>/MAPbI<sub>3</sub>/Spiro-OMeTAD/Ag/Au solar cells under light soaking conditions applied to ITO/SnO<sub>2</sub>/MAPbI<sub>3</sub>/Spiro-OMeTAD stacks:  $J_{sc}$  (a),  $V_{oc}$  (b), f FF (c), and PCE (d).

We have applied the ToF-SIMS analysis in order to gain a deeper insight into the degradation mechanism of PSCs with spiro-OMeTAD hole transport layer. Fresh and degraded ITO/SnO<sub>2</sub>/MAPbI<sub>3</sub>/spiro-OMeTAD/Au devices were profiled with Cs<sup>+</sup> (positive ion detection mode) and O<sub>2</sub><sup>-</sup> (negative ion mode) ion beams to reveal possible light-induced changes inside the functional layers and at the interfaces. Figure 26 shows

the distribution of the most important markers, which can be used to identify the corresponding layers. For instance,  $\text{Pb}^+$  and  $\text{I}_2^-$  ions show the homogeneous distribution and outline the borders of the perovskite film. Organic  $\text{CH}_3\text{NH}_3^+$  cations probed by both  $\text{CH}_3^+$  and  $\text{CH}_5\text{N}^+$  ions show somewhat inhomogeneous distribution. Since the perovskite films were grown using a two-step approach by applying organic iodide on top of  $\text{PbI}_2$  films, some enrichment of the upper layers with respect to MAI as compared to the bottom layers is not surprising. Therefore, both  $\text{CH}_3^+$  and  $\text{CH}_5\text{N}^+$  ions should be considered primarily as markers of non-bound excessive MAI. The  $\text{I}_2^+$  ion, most probably, is the marker of a degradation product formed via oxidation of iodide anions  $\text{I}^-$  to molecular iodine ( $\text{I}_2^+$ ) and its trapping in the form of polyiodide (e.g.  $\text{I}_3^-$ )<sup>123</sup>. Interestingly, for fresh samples, it appears only at the interface between  $\text{SnO}_2$  and  $\text{MAPbI}_3$  since  $\text{Sn(IV)}$  is oxidizing  $\text{I}^-$ , probably under the harsh conditions induced by the ion beam. However, the aged sample shows  $\text{I}_2^+$  signal uniformly distributed in the perovskite layer, which suggests that  $\text{SnO}_2/\text{MAPbI}_3$  interface gets passivated (e.g. via reduction of  $\text{Sn(IV)}$  to  $\text{Sn(II)}$ ) and polyiodide species accumulate everywhere in the bulk of the perovskite phase suggesting its photochemical degradation with the release of iodine. This degradation pathway was identified previously.<sup>35</sup>

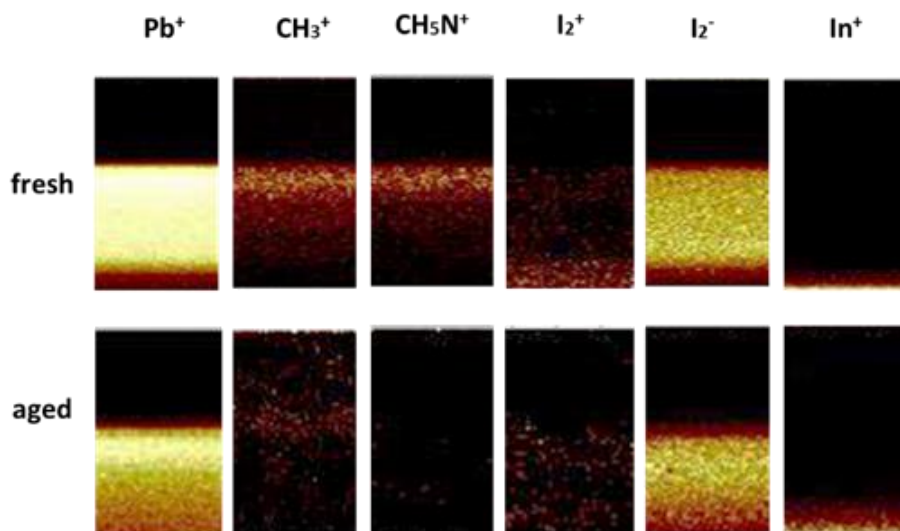


**Figure 26.** ToF-SIMS profiles showing the distribution of the marker in fresh and aged ITO/ $\text{SnO}_2$ / $\text{MAPbI}_3$ /spiro-OMeTAD/Au/Ag solar cells.

The most striking is the behavior of  $\text{CH}_3^+$  and  $\text{CH}_5\text{N}^+$  markers. Both of them virtually disappear in the perovskite layer after aging suggesting the absence of any non-bound “excessive” MAI. This result is expectable since long exposure of the samples to light soaking and elevated temperature ( $\sim 50^\circ\text{C}$ ) facilitated interdiffusion of MAI and  $\text{PbI}_2$  thus producing  $\text{MAPbI}_3$  with uniform composition. However, we can clearly observe the appearance of  $\text{CH}_3^+$  inside the spiro-OMeTAD HTL layer after 100 h of light exposure. One might assume that spiro-OMeTAD behaves in the same way as fullerene derivatives  $\text{PC}_{61}\text{BM}$  and  $\text{PC}_{71}\text{BM}$  by adsorbing and accumulating MAI. However, the fact that  $\text{CH}_5\text{N}^+$  marker ions are not visible in the HTL, suggest other nature of the absorbed species. It was reported previously that thermal and photochemical degradation of  $\text{MAPbI}_3$  produces the first  $\text{PbI}_2$ , while the organic part is decomposing to  $\text{CH}_3\text{NH}_2$ ,  $\text{HI}$ ,  $\text{NH}_3$  and  $\text{CH}_3\text{I}$ . The latter two components might dominate under certain conditions.<sup>33,46</sup> It is known that  $\text{CH}_3\text{I}$  is a strong alkylating reagent and can convert easily aromatic amines  $\text{Ar}_3\text{N}$  to the corresponding quaternized species  $[\text{Ar}_3\text{NCH}_3]^+\text{I}^-$ . Alternatively, it can react with the doping reagent LiTFSI forming  $\text{LiI}$  and  $\text{CH}_3\text{N}(\text{SO}_2\text{CF}_3)_2$  species. Both reactions are presented in Figure 27.

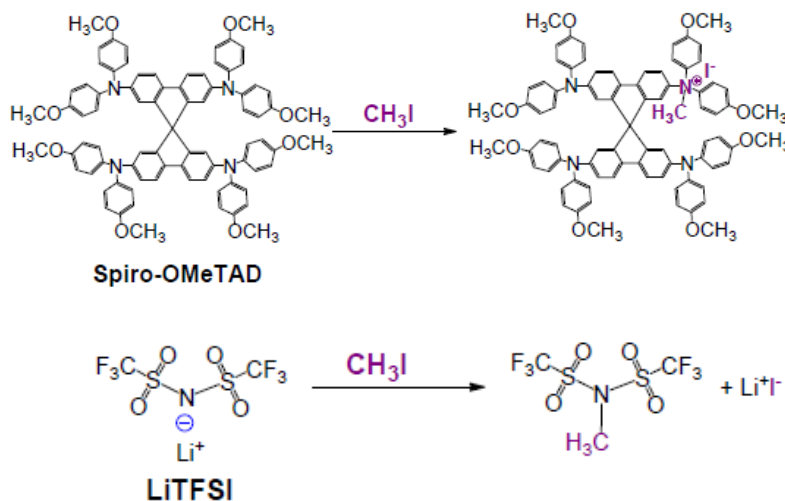


**Figure 27.** Chemical reactions of spiro-OMeTAD with  $\text{CH}_3\text{I}$  and LiTFSI with  $\text{CH}_3\text{I}$ .

Regardless of the fact which pathway is realized, it is clear that spiro-OMeTAD is not chemically inert with respect to the MAPbI<sub>3</sub> photodegradation products and, therefore, can hardly provide long-term device stability.

## 2.7 Summary

In this part of the work, we performed a comparative analysis of five different organic charge transport layers in two different sample geometries: glass/CTL/MAPbI<sub>3</sub> and glass/MAPbI<sub>3</sub>/CTL, which provided complementary information on the interfacial chemistry and encapsulation properties of the corresponding CTLs. Using rylene diimides NDI and PDI as a model system, we have shown that any specific interactions of the perovskite degradation products (PbI<sub>2</sub> in that case) with CTL strongly accelerate MAPbI<sub>3</sub> photodecomposition. Fullerene derivatives PC<sub>61</sub>BM and PC<sub>71</sub>BM showed remarkable encapsulation properties and completely prevented MAPbI<sub>3</sub> decomposition under light soaking conditions. However, interfacial chemistry related to MAI diffusion to the fullerene-based CTL, which was reported previously, ruins the performance of both PC<sub>61</sub>BM and PC<sub>71</sub>BM in PSCs exposed to continuous illumination. Well-known organic hole-transport material spiro-OMeTAD stabilized MAPbI<sub>3</sub> in both sample geometries while being used as an underlayer or upper encapsulation coating for the perovskite films. However, spiro-OMeTAD was also absorbing some of the perovskite degradation products (presumably CH<sub>3</sub>I) as revealed by ToF-SIMS analysis, which affects badly the operation lifetime of the devices using this CTL.

Thus, the presented set of results emphasizes the crucial importance of interfacial degradation effects limiting severely the lifetime of the present generation PSCs. Achieving long-term operation stability in perovskite photovoltaics requires both a deeper understanding of the chemistry occurring at the functional interfaces and designing new advanced CTLs, which can be chemically robust with respect to the perovskite absorber while suppressing the main pathways of its photodegradation.

Among the studied panel of the charge transport materials, fullerene derivatives delivered the most impressive results as top encapsulation coatings improving the stability of the perovskite films. However, MAI diffusion and accumulation in the

fullerene-based ETLs affects badly their electrical characteristics and ruins the perovskite solar cell performance.<sup>48</sup> This challenge can be addressed by filling the space between the fullerene spheres with some inert material, e.g. poly(methyl methacrylate) (PMMA) as was shown recently for PC<sub>61</sub>BM/PMAA passivation coatings. Alternatively, some additional diffusion barriers (e.g. 1 nm thick Al<sub>2</sub>O<sub>3</sub>)<sup>124</sup> might be introduced at perovskite/PC<sub>61</sub>BM interface to block the migration of MAI. We strongly believe that while using these or other approaches for careful engineering the CTL structure and properties, the perovskite community will succeed in substantial increasing the solar cell operation lifetime bringing it to commercially interesting benchmarks.

## **Chapter 3. Unraveling the impact of perovskite and HTL composition on the interfacial photostability of the multilayered stacks and p-i-n solar cells**

### **3.1 Motivation**

Based on the results of the previous chapter, PC<sub>61</sub>BM works as a good encapsulation layer completely preventing bulk photodecomposition of MAPbI<sub>3</sub> films. This gave us an opportunity to focus on the HTL/perovskite interface and study it thoroughly to understand the main degradation mechanisms in devices with p-i-n configuration. Taking MAPbI<sub>3</sub> as a reference system, we expanded the list of studied materials including Cs<sub>0.15</sub>FA<sub>0.85</sub>PbI<sub>3</sub>, Cs<sub>0.1</sub>MA<sub>0.15</sub>FA<sub>0.75</sub>PbI<sub>3</sub>, Cs<sub>0.1</sub>MA<sub>0.15</sub>FA<sub>0.75</sub>Pb(Br<sub>0.15</sub>I<sub>0.85</sub>)<sub>3</sub>, and Cs<sub>0.15</sub>FA<sub>0.85</sub>Pb(Br<sub>0.15</sub>I<sub>0.85</sub>)<sub>3</sub> to assess if the degradation mechanisms depend only on HTL or rather on both HTL and perovskite. Most importantly, we took common HTLs used in p-i-n solar cells and studied their influence on perovskite absorber layer stability.

### **3.2 Materials and methods**

The overall layout of the performed experiments is shown in Figure 28a. First, I studied ITO/HTL/perovskite photostability, by exposing the samples with simulated

light for 1000 h. Then, another set of samples of ITO/HTL/perovskite/PC<sub>61</sub>BM structure was exposed to light soaking for 4000 h. The last part of the experiment aimed at analyzing the photostability of completed solar cells with a refreshed PC<sub>61</sub>BM layer prior to the electrode deposition.

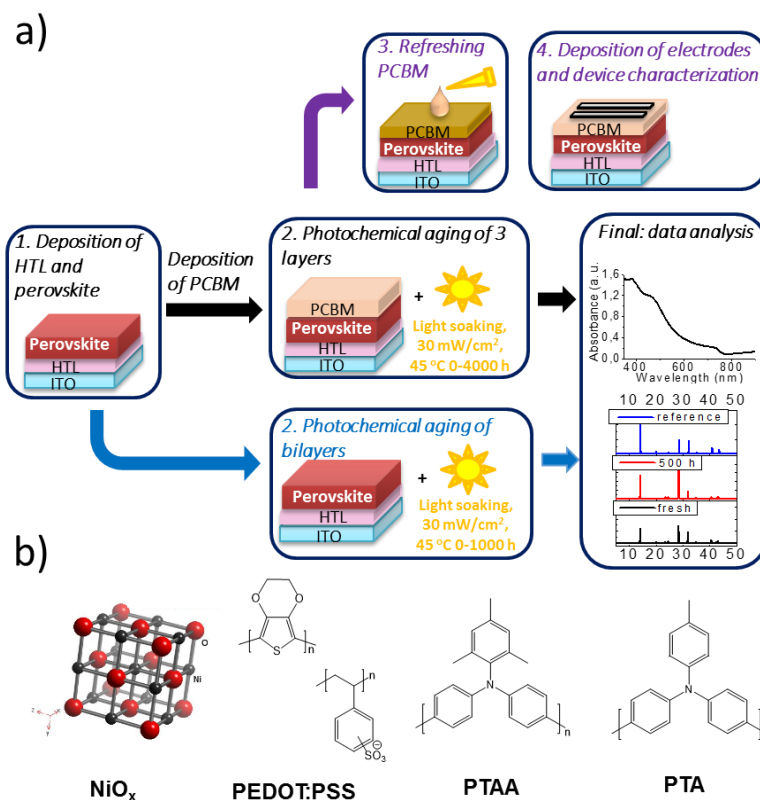


**Figure 28.** The general layout of the experiment (a) and the molecular structures of the used HTL materials (b).

### *Film deposition and sample preparation*

ITO substrates were cleaned by sonication in deionized water, acetone, and isopropyl alcohol (IPA) for 10 min each, dried in the air and subjected to a plasma cleaning (50 W, 300 sec). PEDOT:PSS (Clevious PH) suspension in deionized water was deposited by spincoating at 3000 rpm followed by annealing at 160 °C in air for 20 min. Both PTAA and PTA solutions in toluene (2.5 mg/ml) were deposited inside the argon glove box at 3000 rpm. NiO<sub>x</sub> nanoparticles were synthesized from Ni(NO<sub>3</sub>)<sub>2</sub>·6H<sub>2</sub>O as reported previously.<sup>72</sup> A dispersion of NiO<sub>x</sub> nanoparticles in water

with 15 mg/ml concentration was deposited on substrates by spin-coating in the air at 6000 rpm. Samples were annealed at 160 °C for 10 min to remove water.

#### *Perovskite deposition*

MAPbI<sub>3</sub> solution was prepared by mixing PbI<sub>2</sub> and MAI powders in stoichiometric amounts and dissolving in DMF:DMSO (80:20) mixed solvent to achieve 0.5M concentration. A solution of Cs<sub>0.15</sub>FA<sub>0.85</sub>PbI<sub>3</sub> was prepared by mixing equal molar quantities of PbI<sub>2</sub> and cation iodides CsI:FAI (15:85). For Cs<sub>0.1</sub>MA<sub>0.15</sub>FA<sub>0.75</sub>PbI<sub>3</sub> CsI:MAI:FAI ratio was 10:15:75 with the stoichiometric amount of PbI<sub>2</sub>. Cs<sub>0.1</sub>MA<sub>0.15</sub>FA<sub>0.85</sub>Pb(Br<sub>0.15</sub>I<sub>0.85</sub>)<sub>3</sub> solution was prepared by mixing 16.8 mg MABr, 25.9 mg CsI, 129 mg FAI, 55 mg PbBr<sub>2</sub>, and 391.8 mg PbI<sub>2</sub> powders and 2 ml of DMF:DMSO solvent (80:20) to reach formal perovskite concentration of 0.5M. Cs<sub>0.15</sub>FA<sub>0.85</sub>Pb(Br<sub>0.15</sub>I<sub>0.85</sub>)<sub>3</sub> solution was made using 31.9 mg CsBr, 146.2 FAI, 55 mg PbBr<sub>2</sub>, 391.8 mg PbI<sub>2</sub>, and 2 ml of DMF:DMSO solvent (80:20). All filtered solutions were deposited in glovebox at 4000 rpm followed by quenching with toluene antisolvent after 16 sec. MAPbI<sub>3</sub> films were annealed at 85 °C for 3 min, all other perovskites - at 120 °C for 3 min.

#### *Aging experiment*

The prepared samples were exposed to light soaking for different periods of time ranging from 1000 h to 4000 h in a specially designed aging chamber integrated into MBraun glovebox. Metal halide lamps with a spectrum similar to the solar AM1.5G spectrum were used as a light source with the average power of 37±3 mW/cm<sup>2</sup>. The sample temperature during the experiments was approx. 45±1 °C. We intentionally kept the temperature below 50 °C to avoid undesired phase transitions in some perovskite absorbers (MAPbI<sub>3</sub><sup>33</sup>) and suppress the contribution of heat-induced degradation of complex lead halides.<sup>35</sup>

#### *Multilayered stack and device fabrication*

The p-i-n ITO/PTAA/perovskite/PC<sub>61</sub>BM samples were prepared following the recipes presented elsewhere.<sup>80,51</sup> These stacks were exposed to light soaking under conditions specified above. After a certain period of light exposure ranging from 1000

h to 4000 h, the samples were taken out of the aging chamber. The top PC<sub>61</sub>BM layer was refreshed by washing with 50  $\mu$ L of chlorobenzene and spin-coating a new PC<sub>61</sub>BM film from 20 mg/mL solution in chlorobenzene at 2000 rpm. The top Mg/Ag (20/80 nm) electrodes were evaporated in high vacuum ( $5 \times 10^{-6}$  mbar) through a shadow mask defining the active area of each device as 0.16 cm<sup>2</sup>. Characterization of the solar cells by current-voltage and EQE measurements is described in Chapter 2.3

*Characterization techniques:*

NT MDT microscope (SMENA) was used to measure the topography of the samples in a tapping mode under a dry ambient atmosphere. Scanning electron microscopy (SEM) images were obtained using Supra 50VP instrument. The samples were placed on a microscope stage inside the glove box to reduce the exposure time in the air down to  $\sim$ 1 min. EDX analysis was performed on an Oxford Instruments INCA Energy+ unit integrated with the Supra 50VP microscope. PL spectra were measured in an inert atmosphere using Horiba spectrometer with 532 nm laser as excitation.

The details about UV-vis, XRD, XPS, and ToF-SIMS measurements can be found in Chapter 2.3.

### **3.3 The impact of HTL material on MAPbI<sub>3</sub> photostability**

We selected three HTL materials that are the most commonly used in p-i-n device configuration (PEDOT:PSS, NiO<sub>x</sub>, PTAA) and included additionally recently reported promising hole-transport polymer PTA<sup>82,81</sup> (Figure 28b). Considering the absorber materials, we explored five perovskite compositions including the most common and well-studied methylammonium lead iodide MAPbI<sub>3</sub>, double (Cs<sub>0.15</sub>FA<sub>0.85</sub>PbI<sub>3</sub>) and triple (Cs<sub>0.10</sub>MA<sub>0.15</sub>FA<sub>0.75</sub>PbI<sub>3</sub>) cation formulations as well as mixed halide systems Cs<sub>0.15</sub>FA<sub>0.85</sub>Pb(Br<sub>0.15</sub>I<sub>0.85</sub>)<sub>3</sub> and Cs<sub>0.1</sub>MA<sub>0.15</sub>FA<sub>0.75</sub>Pb(Br<sub>0.15</sub>I<sub>0.85</sub>)<sub>3</sub>. To simplify the notations given below, we define multication and mixed halide systems as CsFAPbI<sub>3</sub>, CsMAFAPbI<sub>3</sub>, CsFAPb(BrI)<sub>3</sub> and CsMAFAPb(BrI)<sub>3</sub>, respectively.

At the first stage, we studied the photochemical stability of ITO/HTL/MAPbI<sub>3</sub> systems. MAPbI<sub>3</sub> is the most studied complex lead halide used in PSCs. It is known that MAPbI<sub>3</sub> rapidly degrades above 50 °C due to the high volatility of MAI and its

decomposition products.<sup>33,35</sup> Our experiments were performed at  $45 \pm 1$  °C to minimize the contribution of heat-induced aging processes. To make sure that thermal degradation does not contribute significantly to the observed sample behavior, a set of identical reference samples was kept in the dark at 45 °C for the same periods of time. The results obtained for the ITO/HTL/MAPbI<sub>3</sub> samples are presented in Figure 29. Photobleaching effect reflected in a gradual decrease of the film absorbance was observed for all studied systems thus suggesting that perovskite films were not photostable (Figure 29a). The usage of NiO<sub>x</sub> as HTL slightly accelerates the degradation, which is particularly evident if we consider the evolution of the perovskite characteristic band at 750 nm.

XRD patterns presented in Fig.29b allowed us to analyze the phase composition of the films as a function of the aging time. In all cases, the perovskite phase was degrading and the phase of PbI<sub>2</sub> was appearing, which is better visualized by the diagrams presented in Figure 29c. The share of each phase was evaluated by considering a relative contribution of the analyzed component to the maximum characteristic peak intensity in the XRD pattern presented in Figure 29b.

This estimation might not be fully accurate with respect to the real quantitative composition of the samples since it does not account for the amorphous phase. However, it provides quite valuable qualitative information about the degradation behavior of perovskite films. The justification for using this method was given in Chapter 2.3.

Following Figure 29c, 1000 h of light soaking results in the formation of ca. 65, 50, 15, and 35% of the PbI<sub>2</sub> phase in the systems with NiO<sub>x</sub>, PEDOT:PSS, PTAA, and PTA HTLs, respectively. The lowest amount of PbI<sub>2</sub> as the aging product is formed in ITO/PTAA/MAPbI<sub>3</sub> samples, which suggests their advanced stability.

Microscopy data presented in Figure 29d show that all perovskite films undergo significant morphological changes during light soaking, which can be considered as a sign of their light-induced degradation. EDX analysis (Figure 29e) revealed that all samples except for ITO/NiO<sub>x</sub>/MAPbI<sub>3</sub> system degrade and become iodide-deficient, which is in line with the previous reports showing severe compositional changes for MAPbI<sub>3</sub> films deposited on glass and exposed to light.

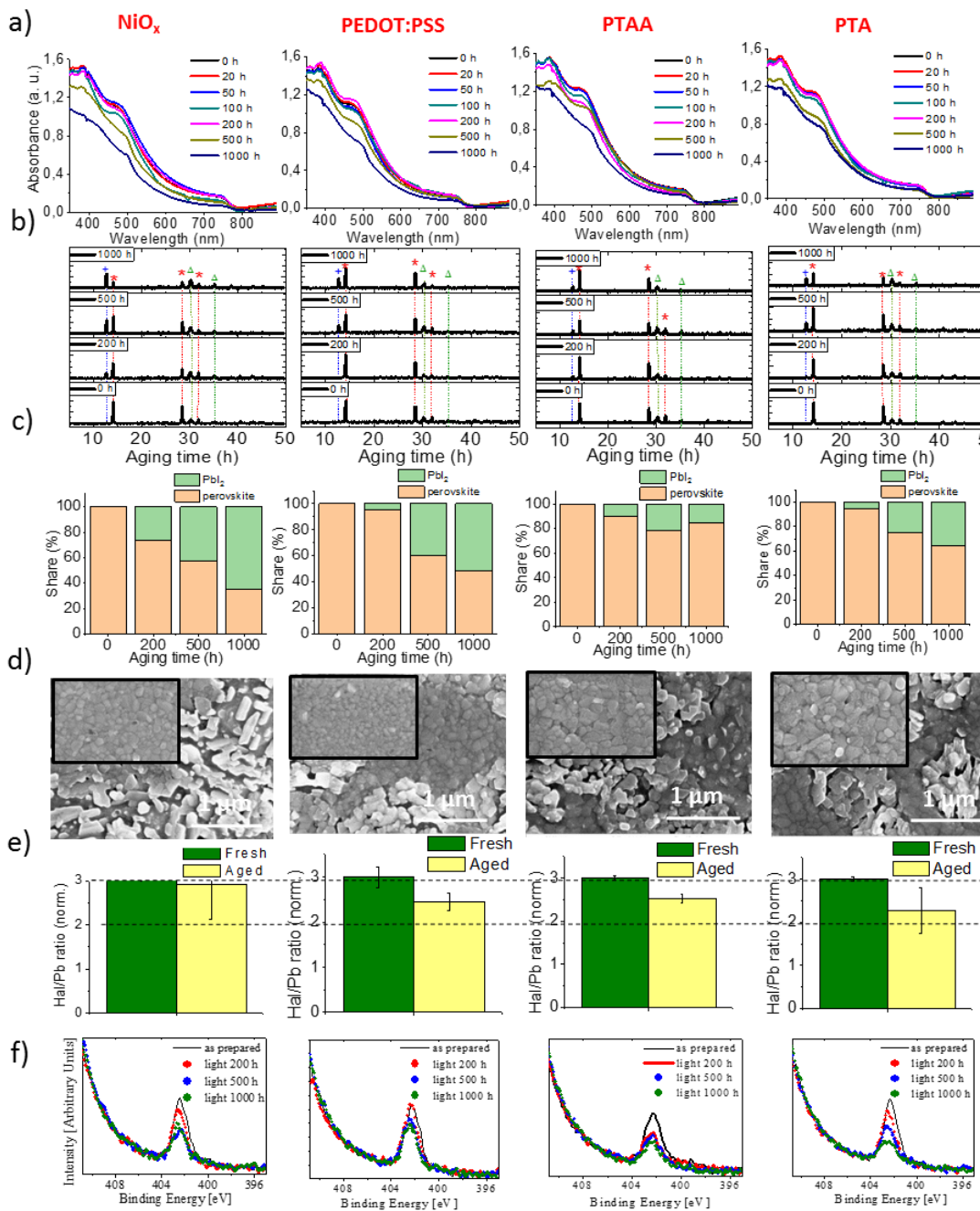


**Figure 29.** UV-vis spectra (a), XRD pattern(b), XRD diagram(c), SEM images(d), EDX data (e) and XPS N1 S –spectra (f) of ITO/HTL/MAPbI<sub>3</sub> samples under light exposure (37±3 mW/cm<sup>2</sup>, 45±1 °C). Symbols on XRD pattern: \* - perovskite phase + - PbI<sub>2</sub> phase Δ – ITO.

The observed unusual compositional stability of ITO/NiO<sub>x</sub>/MAPbI<sub>3</sub> system contradicts with the data provided by other methods evidencing strong perovskite degradation. Therefore, it is very likely that volatile iodine-containing products become somehow trapped in that system rather than released to the atmosphere. A possible mechanism of such trapping involving the NiO<sub>x</sub> HTL layer is discussed below.

XPS analysis was used to follow the changes in the surface composition of the samples. The observed gradual decrease in the intensity of N 1s bands in Figure 29f suggested a strong decomposition of the samples with the loss of MA cations. In that context, the films grown atop PEDOT:PSS were more stable probably due to similar trapping of volatile nitrogen-containing species by HTL. For example, methylamine can be trapped by acidic PSS and this effect can be detected by XPS considering the fact that the films lose their compact structure and form isolated islands at long aging times (Figure 29d).

The overall set of results presented in Figure 29 clearly indicates that HTL influences significantly the light-induced degradation of the perovskite MAPbI<sub>3</sub> films and, probably, even changes the main aging pathway in some cases. To gain a deeper understanding of the interfacial degradation effects we explored fresh and aged (1000 h) samples by the ToF-SIMS analysis. The samples were profiled by O<sub>2</sub><sup>+</sup> ion beams under 10<sup>-6</sup> mbar. Figure 30 shows the distribution of the most important markers assigned to the corresponding HTL layers: NiI<sub>2</sub><sup>+</sup> for NiO<sub>x</sub> and C<sub>2</sub><sup>-</sup> ions for both PEDOT:PSS and PTAA layers. Fresh samples revealed well-defined borders between the HTL and perovskite layer. Light exposure leads to a strong accumulation of NiI<sub>2</sub><sup>+</sup> ions in the perovskite layer suggesting the formation of NiI<sub>2</sub> as a product of the interfacial reaction between MAPbI<sub>3</sub> and NiO<sub>x</sub>. The fact that this system showed almost no iodine loss after light exposure strongly suggests that NiO<sub>x</sub> attracts iodide from the volatile MAI to form NiI<sub>2</sub> and some organic volatiles. The ToF-SIMS analysis of the aged ITO/PEDOT:PSS/MAPbI<sub>3</sub> samples shows strong interdiffusion of the components at both ITO/PEDOT:PSS and PEDOT:PSS/MAPbI<sub>3</sub> interfaces.

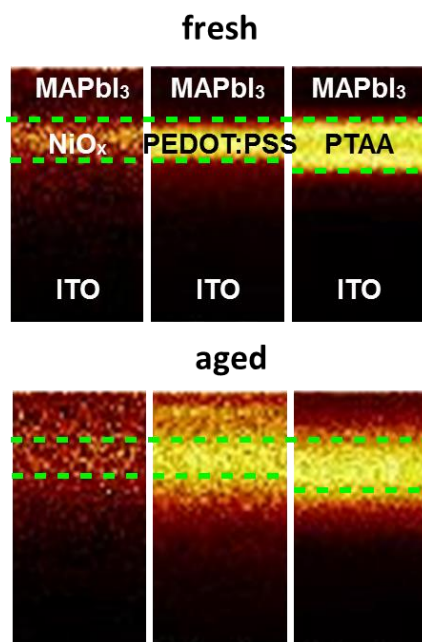


**Figure 30.** Selected ToF-SIMS analysis data for ITO/HTL/MAPbI<sub>3</sub> samples showing the distribution of markers specific for a certain HTL: NiI<sub>2</sub><sup>+</sup> for NiO<sub>x</sub> and C2<sup>-</sup> for PEDOT:PSS and PTAA.

Among three studied systems, only the ITO/PTAA/MAPbI<sub>3</sub> samples did not show severe component intermixing at the HTL/perovskite interface, which might be an origin of superior stability of this stack. Nevertheless, some blurring of the interfaces was still observed, which might be due to a change in the film morphology after light soaking.

To summarize this part, we showed that PTAA has superior stability at the interface with MAPbI<sub>3</sub>. On the contrary, both NiO<sub>x</sub> and PEDOT:PSS induce some interfacial (photo)chemical reactions with MAPbI<sub>3</sub>, which accelerate its light-induced decomposition.

### **3.4 The impact of HTL materials on the operational stability of a series of complex lead halides**

At the next stage of this work, we compared the photostability of a series of complex lead halides combined with a set of different HTL materials. Figure 31 summarizes the evolution of UV-vis spectra of all studied samples under exposure to light. Some of the systems demonstrated typical photobleaching behavior, i.e. gradual

decay of the film absorbance with an increase in the aging time as it was observed for MAPbI<sub>3</sub>. On the contrary, some other systems, in particular, mixed halide perovskites, demonstrated a significant change in the shape of the absorption profile accompanied by an increase in the absorbance at long wavelengths and redshift of the band.

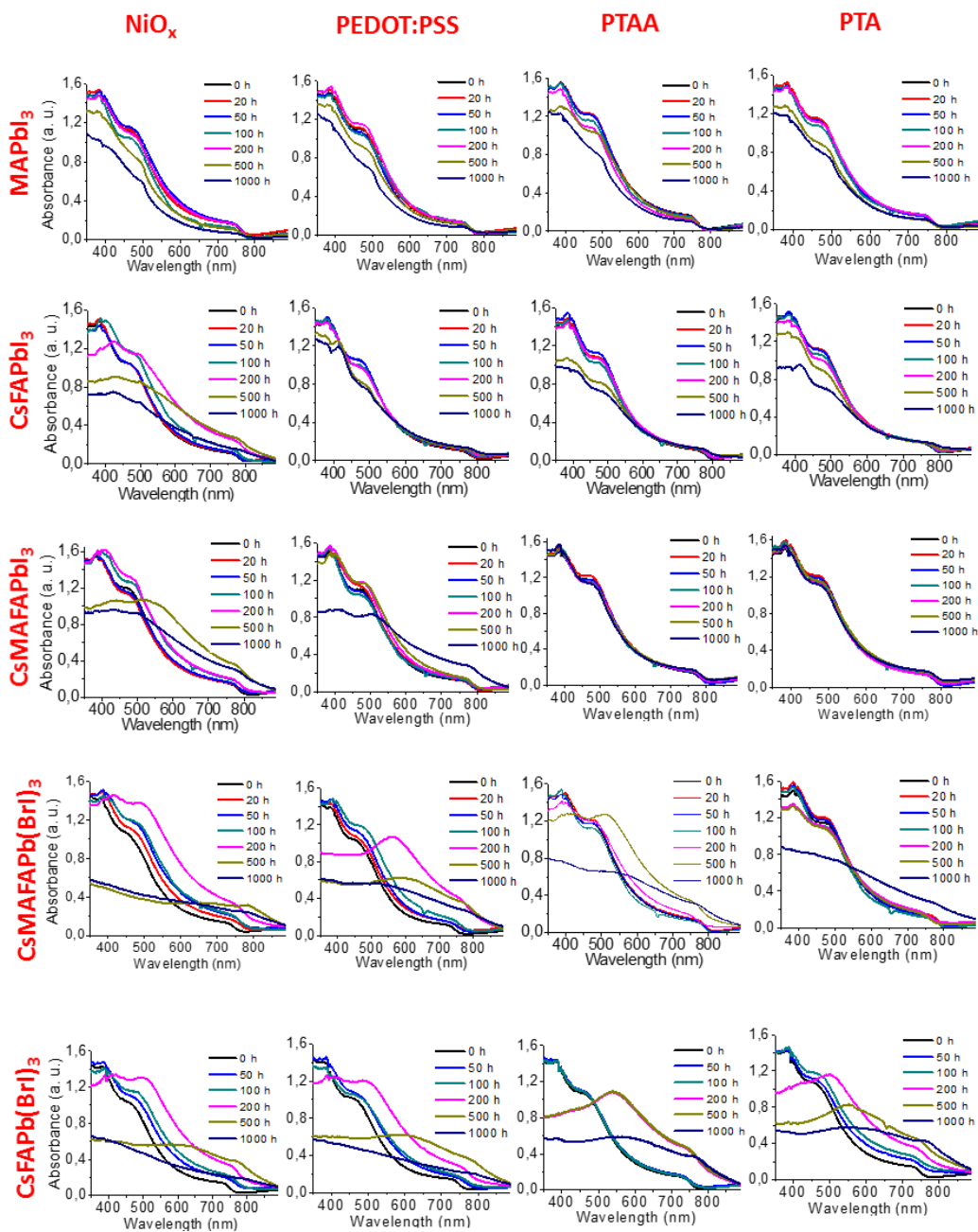


**Figure 31.** Evolution of the UV-vis spectra of various ITO/HTL/perovskite samples under light exposure ( $37\pm 3$  mW/cm<sup>2</sup>,  $45\pm 1^\circ\text{C}$ ).

Using a set of techniques, we have revealed that such unusual film behavior is due to light scattering originated from a significant change of the film morphology under light exposure. Indeed, light causes a significant (at least 10-fold) increase in the size of the perovskite grains as it is evident from the AFM topography and optical microphotographs shown in Figure 32.

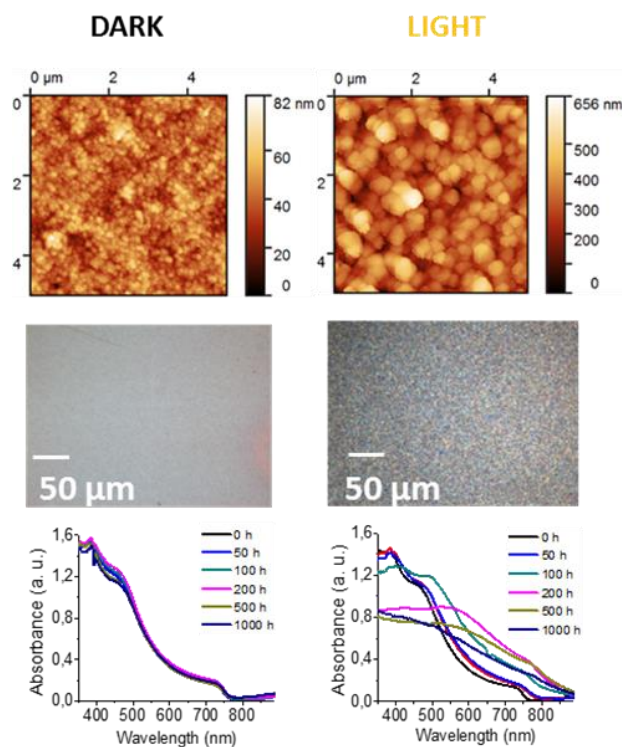


**Figure 32.** Comparison of AFM, SEM images, and UV-vis spectra of ITO/CsMAFAPb(BrI)<sub>3</sub> samples kept under dark and light conditions for 1000 h (T 45 ± 1 °C).

Such evolution of the film morphology leads to the appearance of optical interference and light scattering effects, which change completely the shape of the UV-vis spectrum. SEM images obtained for all samples (Figure 33) confirm that strong light scattering effects in optical spectra correlate with dramatic changes in the film morphology, e.g. appearance of large features in the films. Interestingly, reference samples kept in the dark at the same temperature reproducibly do not show any changes in the film morphology and optical characteristics (Figure 32).

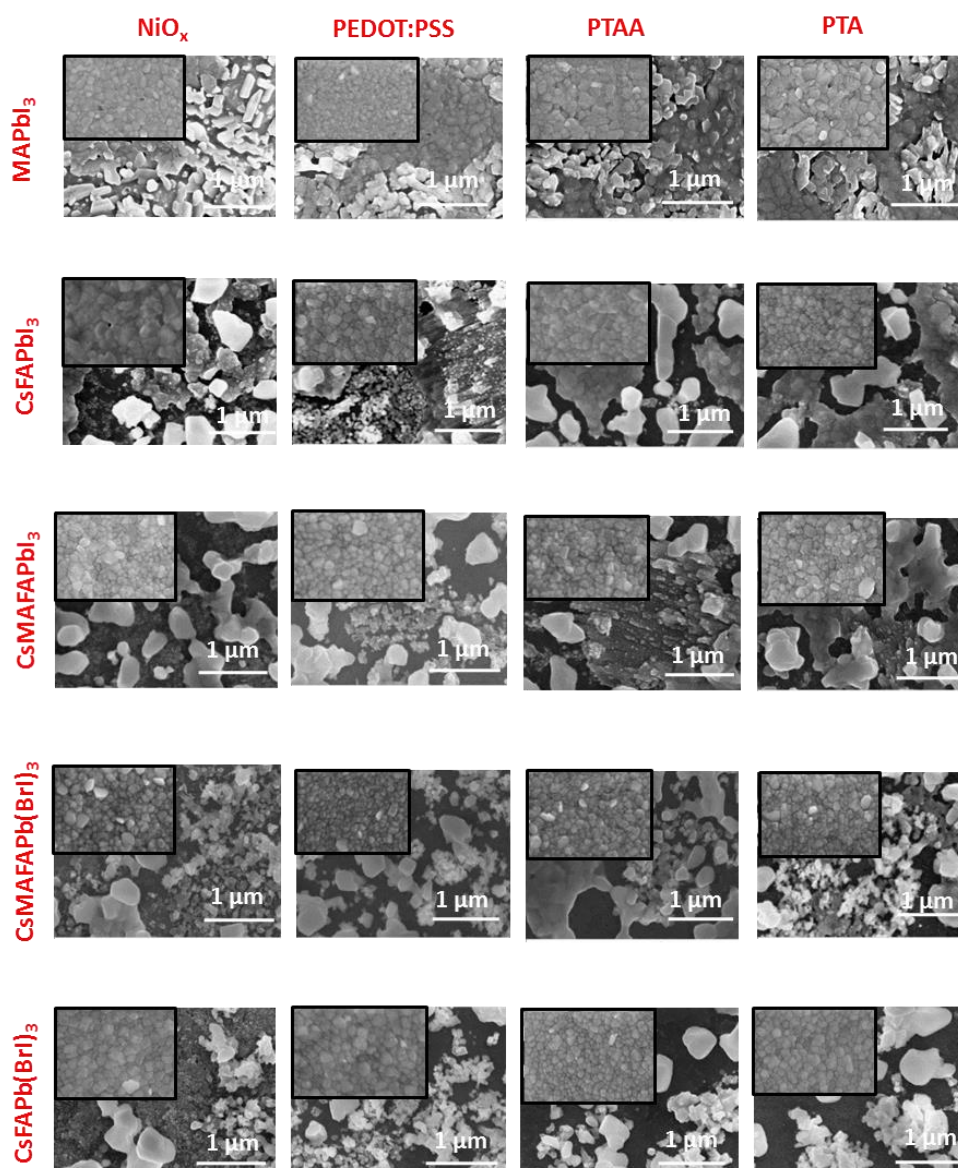


**Figure 33.** SEM images of fresh (inserts) and aged ITO/HTL/perovskite samples after 1000 h of light soaking ( $37\pm 3 \text{ mW/cm}^2$ ,  $45\pm 1 \text{ }^\circ\text{C}$ ).

Moreover, no real photochemical degradation occurs with the material since its phase composition remains the same as follows from the XRD data (Figure 34).

Therefore, the effect observed under light exposure seems to have photoinduced nature and can be called as “light-induced perovskite crystallization”. It should be emphasized that such massive crystallization of the absorber in a completed solar cell

might ruin completely its operation due to the appearance of voids, pinholes or interfacial delamination. Therefore, this effect should be considered as one of the possible pathways of perovskite solar cell degradation. Since MAPbI<sub>3</sub> does not demonstrate such behavior, formamidinium FA<sup>+</sup> cations seem to be promoting light-induced crystallization. The most aggressive crystallization occurs with mixed halide systems, which suggests that the incorporation of bromide anions also facilitates this process. In other words, more disorder we create in the system by compositional engineering, stronger is its tendency to crystallize. In that context, the light might be forming some defects catalyzing the massive crystallization of the perovskite absorber films.

Another interesting phenomenon is associated with the influence of the HTL underlayer on the light-induced crystallization of the perovskite absorber films. Here, the perovskite films grown atop PTA or PTAA showed the least pronounced tendency to crystallize under exposure to light: this happens only with two mixed halide perovskites at long aging times. On the contrary, all perovskite films (except MAPbI<sub>3</sub>) undergo strong light-induced crystallization when they are grown on NiO<sub>x</sub> used as HTL. One might speculate that surface properties of the HTL underlayer govern the kinetics of the perovskite film crystallization. Though we cannot exclude such a possibility, we believe that the observed HTL impact is more related to defects. NiO<sub>x</sub> was shown to be quite aggressive with respect to the perovskite layer, e.g. forming NiI<sub>2</sub> as an interfacial reaction product. Obviously, any chemical interaction between the HTL material and absorber layer create defects, which accelerate perovskite film crystallization. In that context, PTA and PTAA being the most chemically inert materials do not form that many interfacial defects and hence slow down the perovskite film crystallization.

Figure 34 summarizes the evolution of the phase composition of different ITO/HTL/perovskite systems. CsFAPbI<sub>3</sub> behaves in a quite similar way to MAPbI<sub>3</sub> showing dramatic degradation when deposited atop NiO<sub>x</sub> or PEDOT:PSS and being relatively stable in combination with PTAA and PTA HTLs.

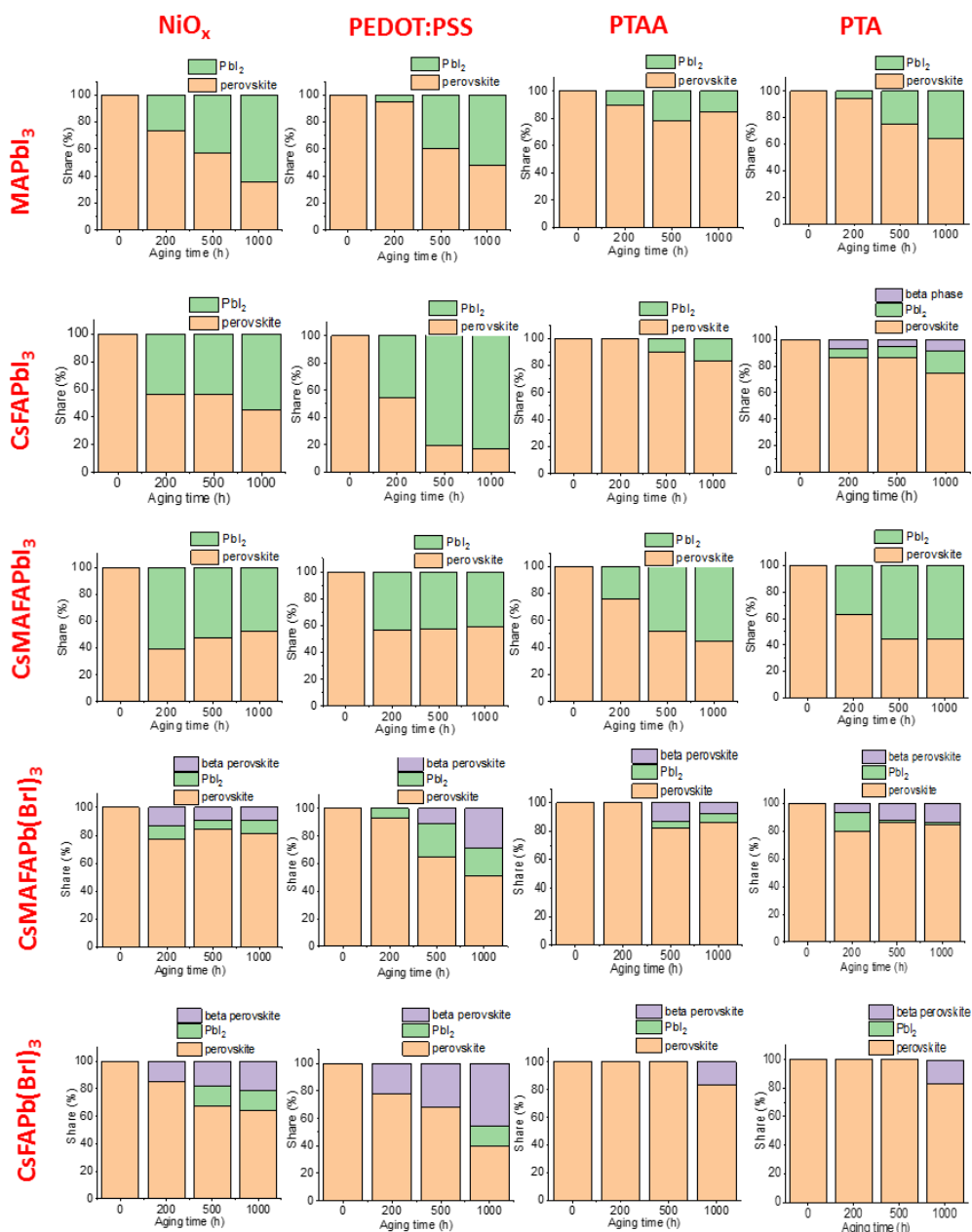


**Figure 34.** Evolution of the phase composition of various ITO/HTL/perovskite samples under light exposure ( $37 \pm 3 \text{ mW/cm}^2$ ,  $45 \pm 1 \text{ }^\circ\text{C}$ ).

Interestingly, ITO/PTA/CsFAPbI<sub>3</sub> system features the formation of  $\beta$ -FAPbI<sub>3</sub> perovskite phase. It is known that pure FAPbI<sub>3</sub> forms a photoactive cubic phase only at T above 170 °C. The introduction of Cs<sup>+</sup> cations significantly decreases the phase transition temperature. Nevertheless, there is still a possibility of segregation of

thermodynamically more stable FA-enriched  $\beta$ -phase from the cubic  $\alpha$ -CsFAPbI<sub>3</sub> perovskite. The results obtained in our work suggest that this process can be influenced by the properties of HTL/perovskite interface. The segregation of the  $\beta$ -FAPbI<sub>3</sub> phase was very characteristic for two mixed halide perovskites. The amount of this non-photoactive beta phase was considerably larger in the case of using NiO<sub>x</sub> and PEDOT:PSS as HTL underlayers, which suggests that phase segregation can be also mediated by the interfacial defects.

The XRD data for CsMAFAPbI<sub>3</sub> samples presented in Figure 34 contradicts quite strongly to the UV-vis data given in Figure 31. Indeed, XRD patterns suggest that all perovskite films strongly degrade with the formation of substantial amounts of PbI<sub>2</sub> as the main decomposition product. However, UV-vis spectra of the films deposited on PTAA or PTA showed virtually no changes consistent with the formation of noticeable amounts of PbI<sub>2</sub>. The optical spectra of the films grown on NiO<sub>x</sub> and PEDOT:PSS were also quite stable and showed only scattering effects at long aging times. We emphasize that both optical spectra and XRD patterns were measured from the same samples, which leaves no room for potential sample-to-sample irreproducibility issue as a possible explanation for the observed discrepancy.

To explain these results, one should keep in mind that XRD visualizes only crystalline components of the films, while the absorption spectra do not depend strongly on the material crystallinity (assuming that the grains are not inducing interference effects). Therefore, we strongly believe that CsMAFAPbI<sub>3</sub> perovskite films undergo amorphization (or a strong decrease in crystallinity) under light exposure. On the contrary, even a minor amount of PbI<sub>2</sub> product is formed as a highly crystalline phase giving strong signals in XRD. As a consequence, the CsMAFAPbI<sub>3</sub> perovskite films seem to be quite stable and undergo just a minor degradation, which is consistent with the UV-vis data. However, high crystallinity of PbI<sub>2</sub> coupled with decreased crystallinity of the perovskite phase accounts for their comparable peak intensities in XRD as observed experimentally.

Another complication is related to the proper ranking of intrinsic stability of the systems, which undergo strong light-induced crystallization, in particular, mixed halide perovskites. When the material is assembled in big 500-1000 nm-sized crystals, light can hardly penetrate through such big particles due to high extinction coefficients of complex lead halides. Hence, such big crystallites undergo light soaking only from the surface and non-shadowed sides, while the bulk phase of the material practically is not exposed to light. Even more problematic is the evaluation of the HTL impact on the perovskite stability in that case, since the contact between HTL and big perovskite crystals becomes very limited. The situation is completely different for uniform thin films of materials, which do not undergo crystallization and, therefore, are efficiently soaked with light in the whole area and preserve efficient contact with the HTL underlayer. As a conclusion, we can hardly compare the stability of the systems showing very different crystallization behavior during the experiment using UV-vis spectra, since they become non-informative because of light scattering, and XRD due to the reasons explained above.

However, some valuable information can be provided by surface analysis techniques such as XPS. Figure 35 shows the comparison of Pb 4f and N 1s spectra of CsMAFAPbI<sub>3</sub> and CsMAFAPb(BrI)<sub>3</sub> samples deposited on different HTLs. N 1s spectra clearly evidence some decomposition of organic cations (MA or FA) considering the noticeable decrease in the intensity of the bands for the samples prepared using NiO<sub>x</sub> and PEDOT:PSS as HTLs. This nitrogen depletion from the films was ca. twice stronger in the case of mixed halide system CsMAFAPb(BrI)<sub>3</sub> probably due to increased volatility of organic bromides as compared to iodides. Interestingly, the samples of both perovskite formulations did not show any nitrogen loss in the case when they were deposited on PTAA or PTA thus further confirming superior stability provided by these HTL materials.

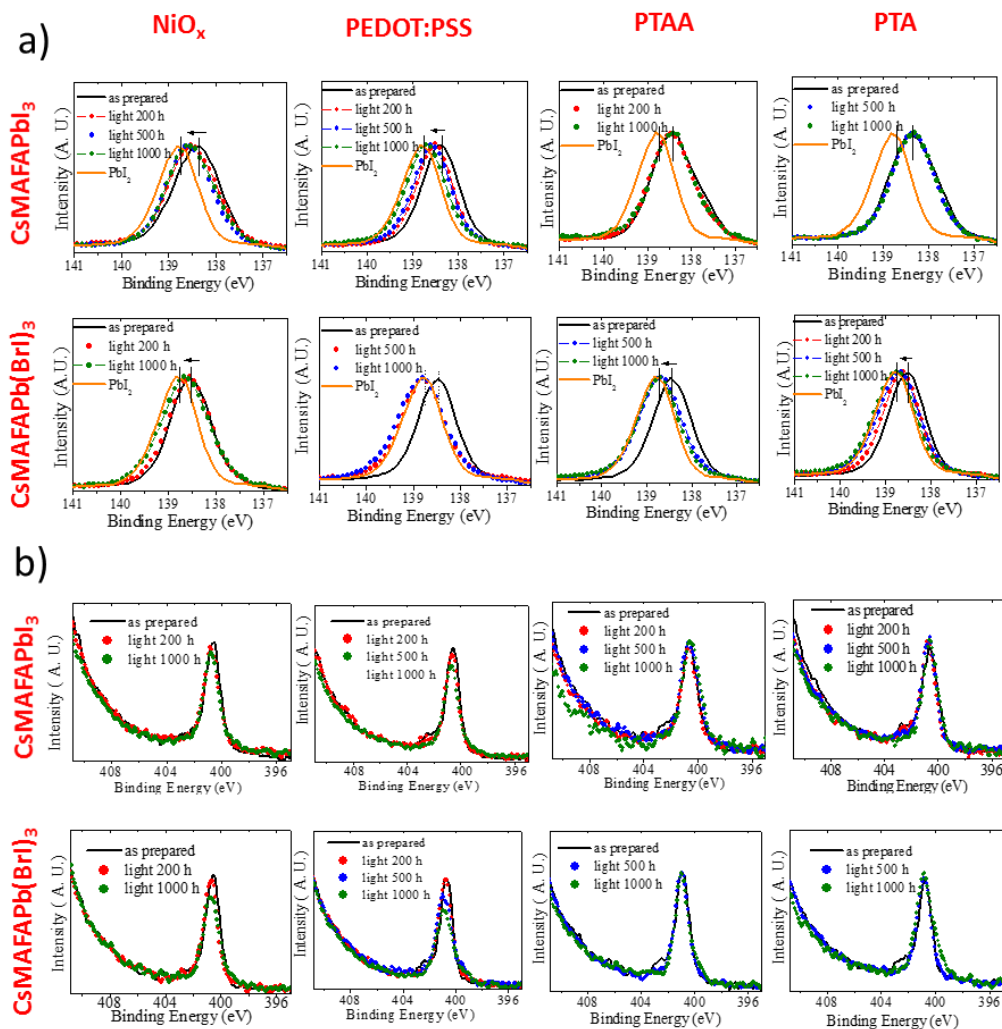


**Figure 35.** Evolution of Pb 4f (a) and N 1s (b) XPS spectra for ITO/HTL/perovskite samples under light exposure ( $37\pm 3$  mW/cm<sup>2</sup>,  $45\pm 1$  °C).

Considering the XPS Pb 4f bands, one can easily deduce the light-induced formation of PbI<sub>2</sub> on the surface of all samples grown at NiO<sub>x</sub> and PEDOT:PSS as HTLs, though this effect was considerably stronger for Br-containing perovskite. Interestingly, CsMAFAPbI<sub>3</sub> showed no PbI<sub>2</sub> formation for the films deposited on PTAA or PTA, thus featuring surface passivation effects. On the contrary, samples of CsMAFAPb(BrI)<sub>3</sub> undergo photodecomposition even in combination with such HTLs as PTAA or PTA. To summarize, it is evident from the obtained results that mixed halide

perovskites are less stable than Br-free complex lead iodides regardless of the used HTL underlayer. However, among the HTL layers, NiO<sub>x</sub> and PEDOT:PSS appear to be less promising since they promote degradation of the deposited on top perovskite film. On the contrary, PTA and PTAA provide significantly improved stability due to the formation of an optimal HTL/perovskite interface.

The EDX analysis data presented in Figure 36 show the iodine loss from the samples after their exposure to light for 1000 h.

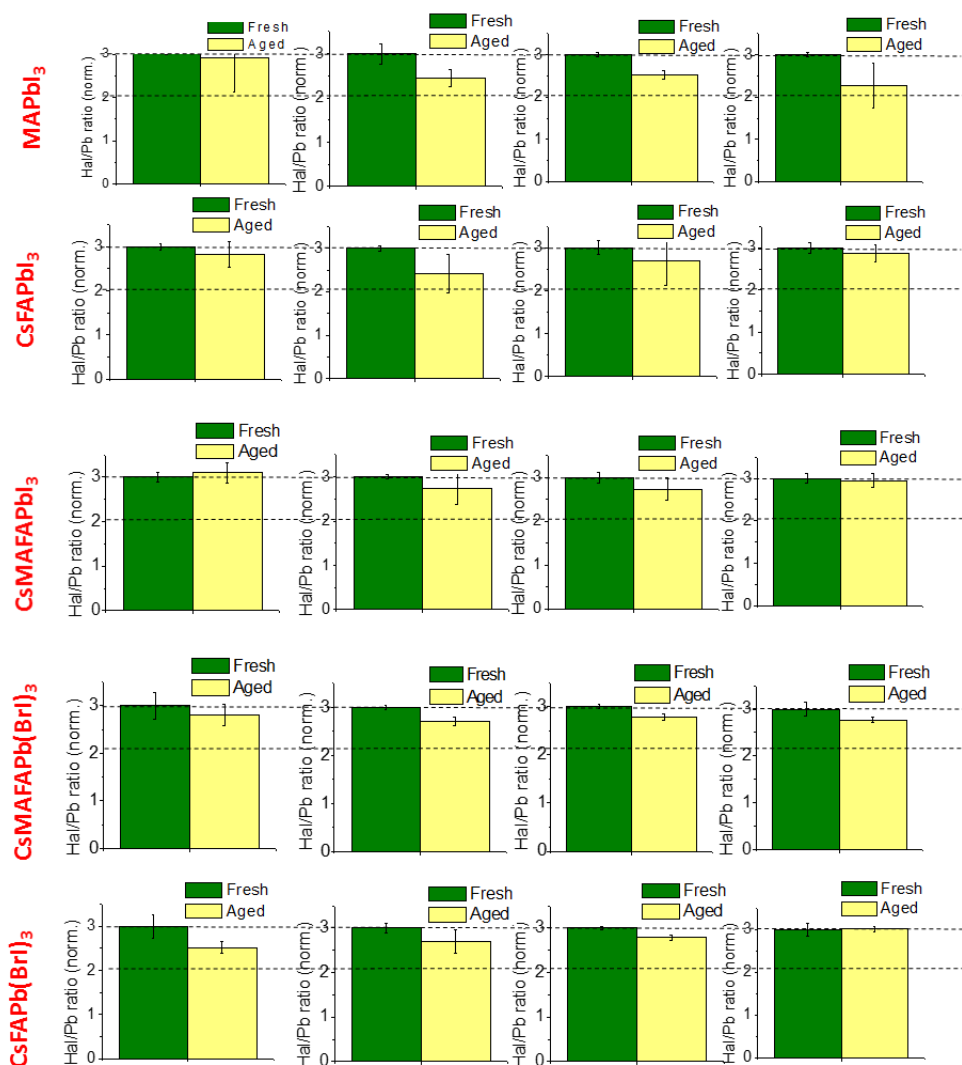


**Figure 36.** Evolution of the chemical composition (halogen to Pb ratio) of the films based on normalized EDX data of various ITO/HTL/perovskite samples under light exposure ( $37\pm 3$  mW/cm<sup>2</sup>,  $45\pm 1$  °C).

Among all the systems, most of the perovskite samples deposited on NiO<sub>x</sub> showed virtually unchangeable I/Pb ratio, which might be related to efficient iodide trapping in the form of NiI<sub>2</sub>, which is discussed above. This hypothesis is also indirectly supported by the fact that two mixed halide CsMAFAPb(BrI)<sub>3</sub> and CsFAPb(BrI)<sub>3</sub> perovskites still revealed a considerable iodine loss even when they were grown atop NiO<sub>x</sub>. Indeed, these perovskites undergo fast light-induced crystallization leading to dramatic shrinkage of the perovskite/NiO<sub>x</sub> contact interface and, hence, reducing the ability of the latter to trap iodide probably released during the decomposition of organic MAI and FAI. The perovskite films deposited atop PTAA and PTA showed reproducibly lower iodine loss compared to the perovskite films grown on PEDOT:PSS. Therefore, these results additionally confirm the advanced stability of interfaces provided by PTAA and PTA. Among different perovskites, the smallest compositional changes were revealed for CsMAFAPbI<sub>3</sub>, which is consistent with the UV-vis data for this system showing minimal evolution during light soaking within 1000 h (Figure 31).

Another interesting effect was observed while studying the PL properties of the films before and after different periods of light exposure. Table 2 summarizes the positions of PL maxima for fresh and aged within 1000 h samples for each of the studied systems. As can be seen from the table, light soaking results in a strong PL redshift in the case of mixed halide systems. It is especially visible on the PL graphs presented in Figure 37. On the contrary, Br-free complex lead iodides showed no changes in the position of PL band within the error of the measurement.

A similar redshift of the PL band under light exposure and reversed process observed in the dark is known as the “Hoke effect” and was reported previously many times for mixed halide lead-based perovskites.<sup>125,126,127</sup> Our experiments suggest that long-term light soaking results in a massive halide phase segregation, which becomes essentially irreversible. At least, we were not able to observe any recovery of the PL peak position for aged samples within a few months of storage in the dark.

**Table 2.** PL maxima for fresh and degraded ITO/HTL/perovskite samples after 1000 h of continuous light exposure ( $37\pm 3$  mW/cm<sup>2</sup>,  $45\pm 1$  °C).

Perovskite	HTL	PL maxima, nm		
		fresh	aged	$\Delta$
MAPbI <sub>3</sub>	NiO <sub>x</sub>	766	766	0
	PEDOT:PSS	765	765	0
	PTAA	767	768	1
	PTA	767	765	-2
CsFAPbI <sub>3</sub>	NiO <sub>x</sub>	791	790	-1
	PEDOT:PSS	791	791	0
	PTAA	791	792	1
	PTA	790	793	3
CsMAFAPbI <sub>3</sub>	NiO <sub>x</sub>	794	792	-2
	PEDOT:PSS	791	793	2
	PTAA	793	794	1
	PTA	792	792	0
CsMAFAPb(BrI) <sub>3</sub>	NiO <sub>x</sub>	755	774	<b>19</b>
	PEDOT:PSS	749	777	<b>28</b>
	PTAA	747	776	<b>29</b>
	PTA	752	776	<b>24</b>
CsFAPb(BrI) <sub>3</sub>	NiO <sub>x</sub>	751	773	<b>22</b>
	PEDOT:PSS	756	776	<b>20</b>
	PTAA	757	771	<b>14</b>
	PTA	759	770	<b>12</b>

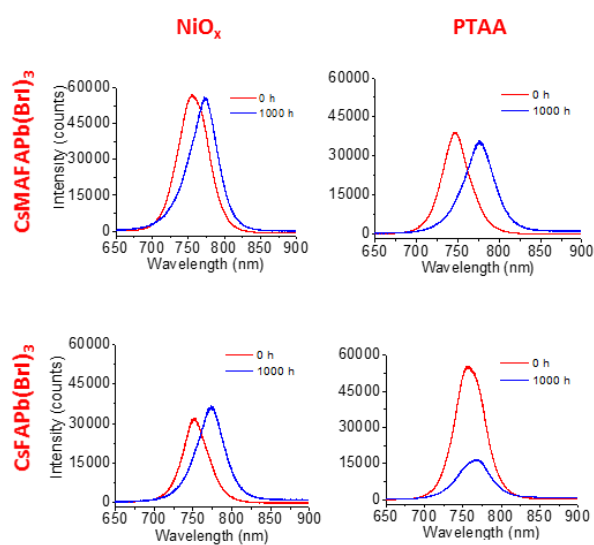


**Figure 37.** PL spectra of fresh and degraded ITO/HTL/perovskite samples after 1000 h of continuous light exposure ( $37\pm 3$  mW/cm<sup>2</sup>,  $45\pm 1$  °C).

### **3.5 Impact of PC<sub>61</sub>BM upper coating on the photostability of lead halide perovskites in ITO/HTL/perovskite/PC<sub>61</sub>BM sample configuration**

Considering our experimental data presented above and preceding reports on the photostability of pristine perovskite films deposited on glass,<sup>35</sup> we can conclude that behavior of ITO/HTL/perovskite samples is governed by two major effects:

- interfacial (photo)chemical interactions between HTL and perovskite absorber;
- intrinsic light-induced decomposition of complex lead halides occurring in top layers of absorber film, which are not impacted by HTL.

Since in this chapter we are most interested in the first effect, the second one has to be somehow suppressed. We have shown in Chapter 2 that the photostability of MAPbI<sub>3</sub> films can be improved dramatically by depositing top coating composed of the fullerene derivative PC<sub>61</sub>BM.<sup>37</sup> The stabilization effect is mostly related to the encapsulation of the absorber film and blocking the evaporation of volatile products formed during light-induced degradation of complex lead halides. Accumulation of the aging products in the perovskite films shifts the equilibrium to the desired direction and prevents their further decomposition. In the present study, we also deposited the top encapsulation coating of PC<sub>61</sub>BM in the series of ITO/HTL/perovskite/PC<sub>61</sub>BM samples and expected that it will suppress the intrinsic perovskite degradation while having probably less impact on the aging pathways occurring at the perovskite/HTL interfaces. Therefore, degradation processes occurring in the multilayer ITO/HTL/perovskite/PC<sub>61</sub>BM stacks closely resemble the behavior of p-i-n PSCs under realistic operation conditions except for certain aging pathways involving the top electrode, which are beyond the scope of this work. The concept is schematically presented in Figure 38.

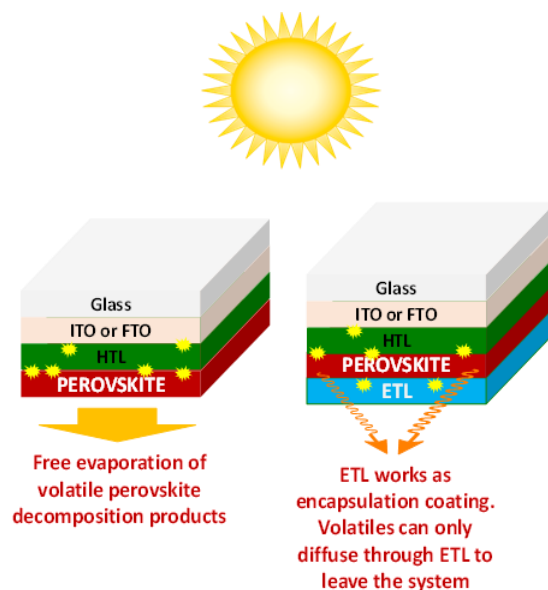


**Figure 38.** Schematic illustration of different aging pathways for samples with and without top ETL encapsulation coating.

It should be emphasized that the ITO/HTL/perovskite/PC<sub>61</sub>BM sample structure is very similar to the used p-i-n solar cell geometry besides the absence of top metal electrodes. Figure 39 illustrates the behavior of different ITO/HTL/MAPbI<sub>3</sub>/PC<sub>61</sub>BM systems assessed using a set of complementary analytical techniques. First, no detectable changes were revealed in the absorption spectra of all samples within 4000 h of light soaking with except for the system comprising NiO<sub>x</sub> as HTL.

These results suggest that PC<sub>61</sub>BM encapsulation coating indeed was able to suppress bulk degradation of the perovskite films while having much less impact on the chemical processes occurring at the HTL/perovskite interface. Therefore, NiO<sub>x</sub> being the most aggressive among the tested HTLs, still induced partial decomposition of the perovskite films due to the formation of NiI<sub>2</sub> and volatile byproducts as revealed by ToF SIMS analysis discussed above. XRD showed the formation of minor amounts of PbI<sub>2</sub>, which is consistent with the reaction of NiO<sub>x</sub> with organic iodide MAI. Interestingly, PL spectra showed no significant evolution for all samples regardless of the used HTL underlayer, which suggests that the perovskite films do not undergo any significant aging in the top layers adjacent to PC<sub>61</sub>BM.

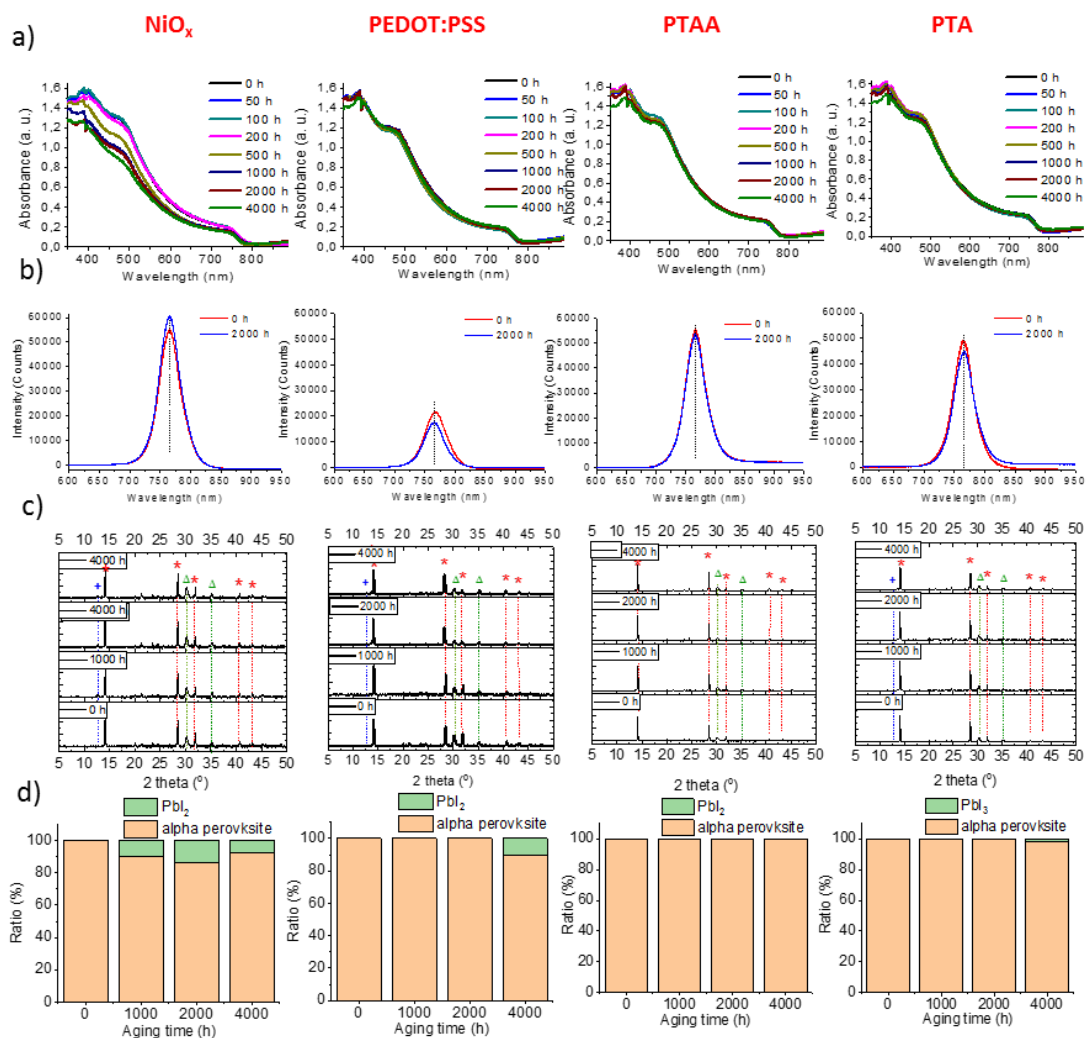


**Figure 39.** Evolution of the UV-vis spectra (a) PL spectra (b), XRD patterns (c) and phase composition (d) of ITO/HTL/MAPbI<sub>3</sub>/PC<sub>61</sub>BM samples under constant illumination (37±3 mW/cm<sup>2</sup>, 45±1 °C). Symbols on XRD pattern: \* - perovskite phase + - PbI<sub>2</sub> phase Δ – ITO.

Summarizing the results obtained for all four ITO/HTL/MAPbI<sub>3</sub>/PC<sub>61</sub>BM systems, we can conclude that PTAA provides superior stability of the perovskite films, which is especially evident from the XRD data (Figure 39).

The remarkable stabilization effect of PC<sub>61</sub>BM ETL coating was also revealed for all other investigated complex lead halides. Particular exciting were the results obtained for mixed halide perovskites: PC<sub>61</sub>BM coating not only prevented the light-induced crystallization of the absorber film but also suppressed halide phase segregation, as can

be concluded from the PL spectra showing no redshift of the band after light exposure (Figure 40, Table 3, Figure 41). Interestingly, light soaking of the samples with PC<sub>61</sub>BM top layer shows the formation of just minor (if any) amounts of  $\beta$ -FAPbI<sub>3</sub> phase in contrast to the samples exposed without such coating. Most likely, PC<sub>61</sub>BM hinders the segregation of  $\beta$ -FAPbI<sub>3</sub> from multication and mixed halide perovskites.

**Table 3.** PL maxima for fresh and degraded ITO/HTL/perovskite/PC<sub>61</sub>BM samples after 2000 h of continuous light soaking (37±3 mW/cm<sup>2</sup>, 45±1 °C).

Perovskite	HTL	PL maximum wavelength, nm		
		fresh	aged	$\Delta$
MAPbI <sub>3</sub>	NiO <sub>x</sub>	766	764	-2
	PEDOT:PSS	767	766	-1
	PTAA	767	766	-1
	PTA	766	766	0
CsFAPbI <sub>3</sub>	NiO <sub>x</sub>	784	785	1
	PEDOT:PSS	784	785	1
	PTAA	788	787	-1
	PTA	785	787	2
CsMAFAPbI <sub>3</sub>	NiO <sub>x</sub>	790	790	0
	PEDOT:PSS	788	788	0
	PTAA	789	789	0
	PTA	789	788	-1
CsMAFAPb(BrI) <sub>3</sub>	NiO <sub>x</sub>	753	752	-1
	PEDOT:PSS	751	751	0
	PTAA	750	751	1
	PTA	748	750	2
CsFAPb(BrI) <sub>3</sub>	NiO <sub>x</sub>	753	750	-3
	PEDOT:PSS	759	752	-7
	PTAA	756	752	-4
	PTA	761	751	-10

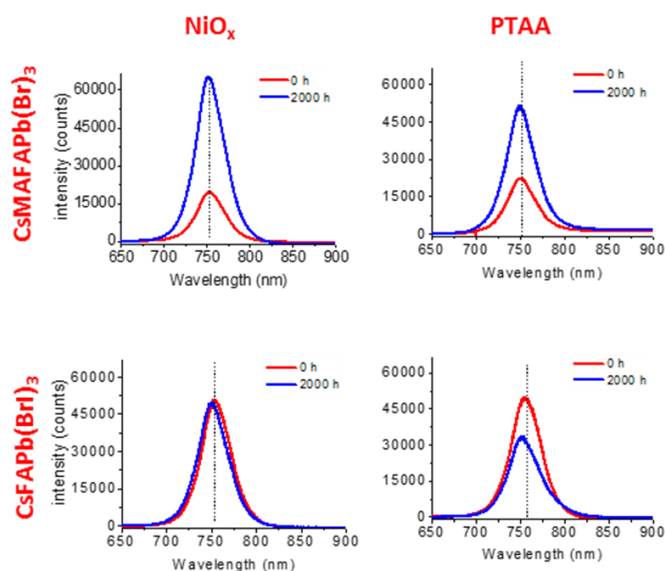


**Figure 40.** PL intensity for fresh and degraded ITO/HTL/perovskite/PC<sub>61</sub>BM samples after 1000 h of continuous light exposure ( $37\pm 3$  mW/cm<sup>2</sup>,  $45\pm 1$  °C).

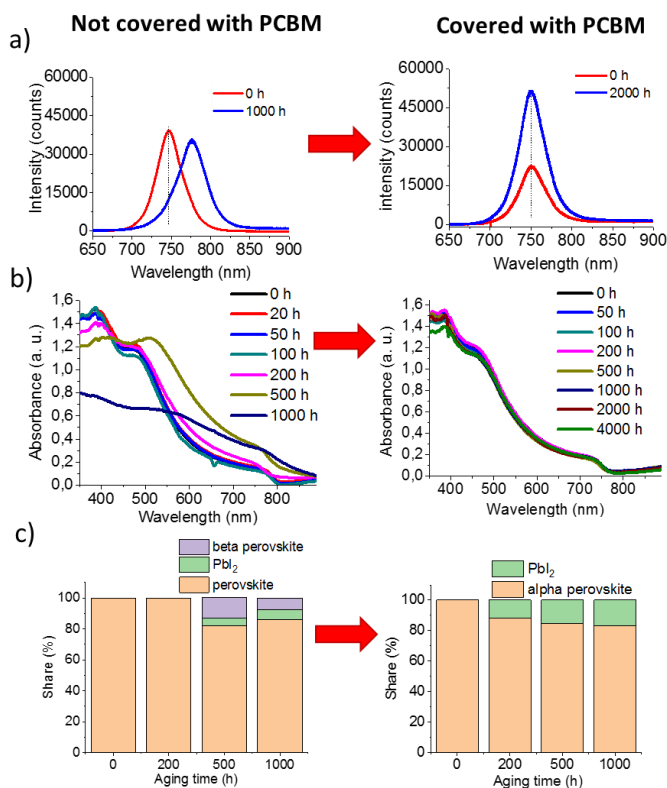


**Figure 41.** Effect of PC<sub>61</sub>BM coating on the aging behavior of ITO/PTAA/CsMAFAPb(Br)<sub>3</sub> samples.

In general, PC<sub>61</sub>BM coating prevented photobleaching of virtually all perovskite films deposited on various HTL underlayers (Figure 42).

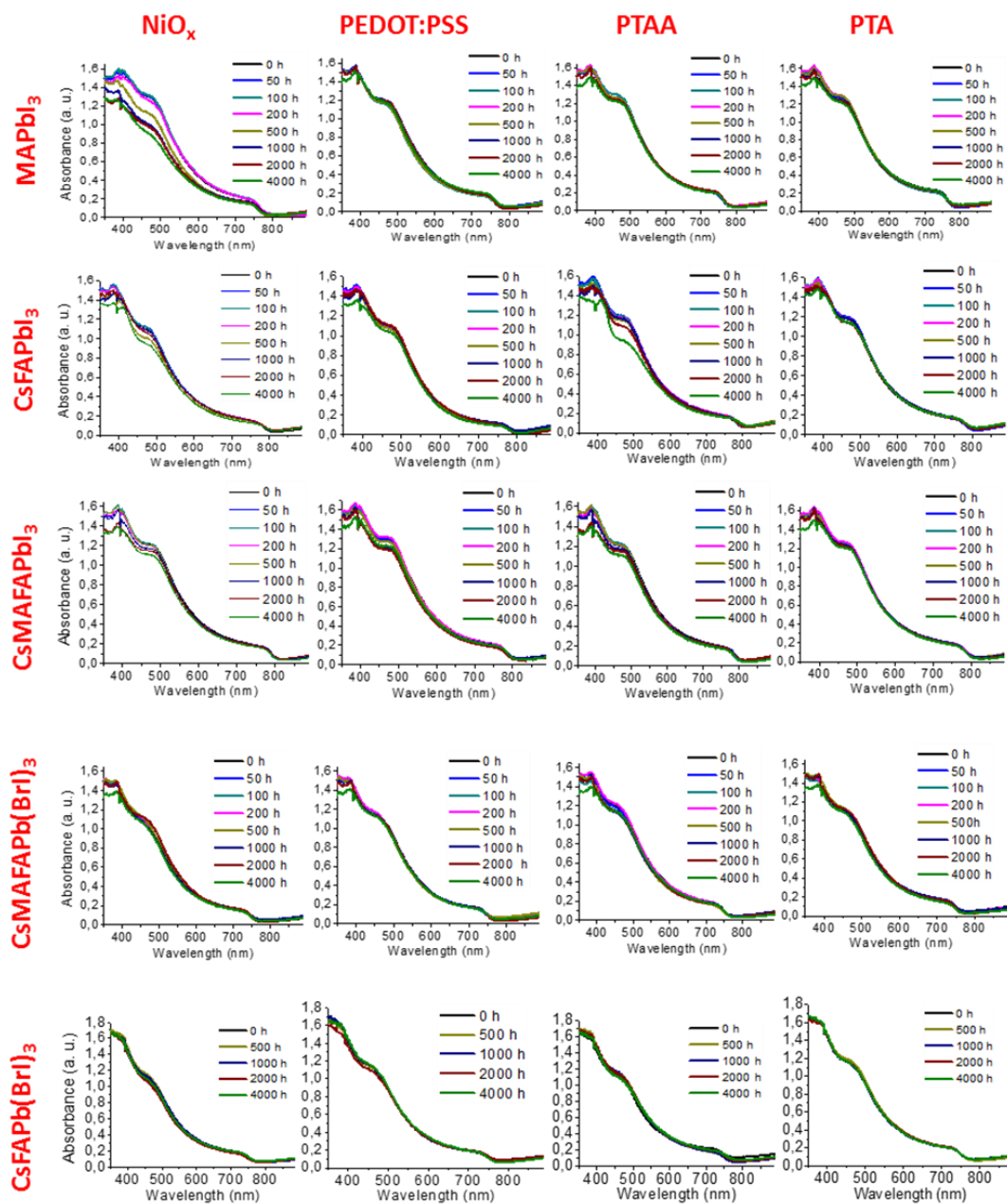


**Figure 42.** Evolution of the UV-vis spectra of ITO/HTL/perovskite/PC<sub>61</sub>BM samples under light exposure ( $37\pm 3$  mW/cm<sup>2</sup>,  $45\pm 1$  °C).

Among the exceptions showing some dynamics in the UV-vis spectra suggesting minor light-induced degradation of the material we can refer to CsFAPbI<sub>3</sub> and

CsMAFAPbI<sub>3</sub> films deposited on NiO<sub>x</sub>, PEDOT:PSS and PTAA. On the contrary, the same perovskites were fairly stable when grown atop PTA HTL. The XRD analysis (Figure 43) revealed the formation of PbI<sub>2</sub> and beta perovskite phase as major degradation products in the case of multiple perovskite/HTL systems.

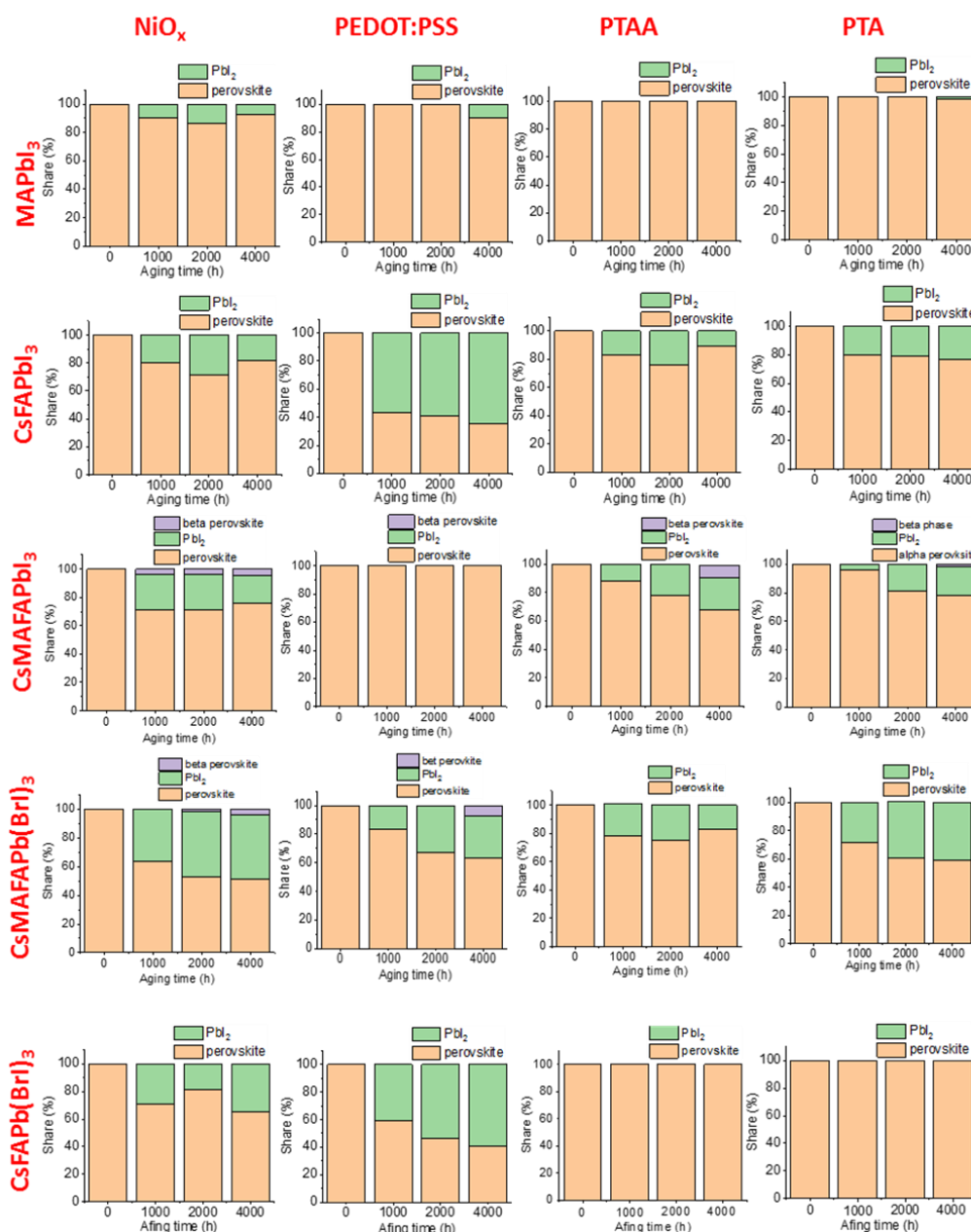


**Figure 43.** Evolution of the phase composition of various ITO/HTL/perovskite/PC<sub>61</sub>BM samples under light exposure (37±3 mW/cm<sup>2</sup>, 45±1 °C).

Even though the peaks of these aging products in XRD patterns were quite intense due to high crystallinity, the realistic concentrations of these species should be quite low considering that no significant changes were observed in the optical characteristics of the films. The most stable, apparently, were the films of MAPbI<sub>3</sub> along with the mixed halide bication perovskite formulations CsFAPb(BrI)<sub>3</sub> grown on PTA and PTAA HTLs, since these systems revealed no light-induced changes in their optical spectra and XRD patterns after 4000 h of constant light exposure.

These results are in sharp contrast with the data obtained for the series of ITO/HTL/perovskite samples and, therefore, feature the strong impact of the upper ETL encapsulation coating on the aging behavior of the multilayered system.

### **3.6 Impact of absorber material on the operational stability of PSCs**

The obtained set of results featured PTAA and PTA as the most promising HTLs providing stable interfaces with the perovskite absorber films. Therefore, we selected PTAA as an exemplary hole-transport layer for comparing the operational stability of solar cells based on different perovskite formulations. To perform this experiment, we prepared a series of ITO/PTAA/perovskite/PC<sub>61</sub>BM stacks and exposed them to light soaking for different periods of time. Afterward, the aged PC<sub>61</sub>BM coatings were washed away and replaced with fresh films of the same ETL material, which was followed by top electrode evaporation (20 nm of Mg and 80 nm of Ag) in a high vacuum (experiment layout shown in Figure 28). The need for “PC<sub>61</sub>BM refreshing” is related to the aging processes at the perovskite/PC<sub>61</sub>BM interface reported in Chapter 2.<sup>51</sup> Even though this interfacial effect has a negligibly small influence on the composition of the bulk perovskite film, aging of the interface blocks charge extraction and ruins the solar cell performance. Figure 44 shows the evolution of the power conversion efficiency of solar cells based on MAPbI<sub>3</sub>, CsFAPbI<sub>3</sub>, CsMAFAPb(BrI)<sub>3</sub>, and CsMAFAPbI<sub>3</sub> perovskites.

Surprisingly, the solar cells based on MAPbI<sub>3</sub> demonstrated much superior operation stability in comparison with other systems. Lower stability of multication and mixed halide perovskites might be attributed to unfavorable phase dynamics (cation or

anion-induced phase segregation) leading to spatial inhomogeneity within the absorber film and forming traps for charge carriers.<sup>128</sup>

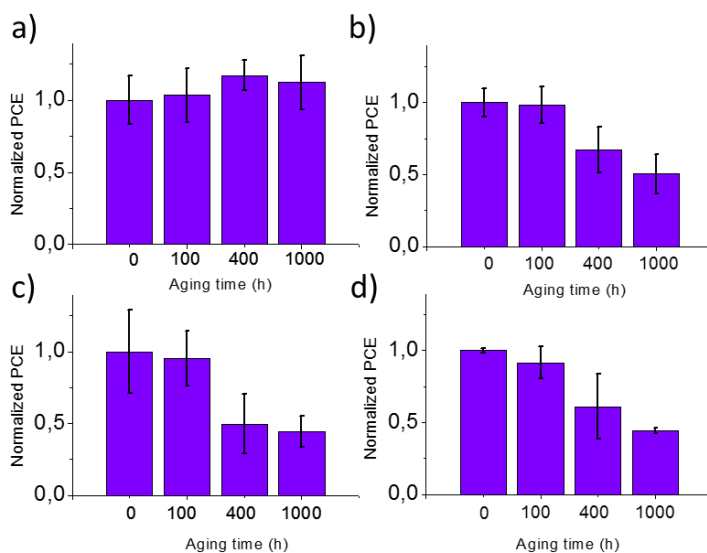


**Figure 44.** Comparison of normalized PCE values of solar cells with ITO/PTAA/perovskite/PC<sub>61</sub>BM/Mg/Ag configuration, where perovskite is MAPbI<sub>3</sub> (a), CsFAPbI<sub>3</sub>(b), CsMAFAPbI<sub>3</sub>(c), CsMAFAPb(BrI)<sub>3</sub> (d).

These results suggest a need for changing the paradigm, i.e. paying more attention to simple perovskite formulations such as MAPbI<sub>3</sub> or FAPbI<sub>3</sub> rather than focusing on compositional engineering, which was leading the development of the field of perovskite photovoltaics for a decade.

### 3.7 Summary

In this work, we performed a thorough study of 20 different perovskite-HTL systems based on combinations of 4 HTLs (NiO<sub>x</sub>, PEDOT:PSS, PTAA, and PTA) with 5 complex lead halides: MAPbI<sub>3</sub>, CsFAPbI<sub>3</sub>, CsMAFAPbI<sub>3</sub>, CsMAFAPb(BrI)<sub>3</sub> and CsFAPb(BrI)<sub>3</sub>. We expected that systematic variation of HTL and perovskite materials will provide essential information on the factors governing the stability of HTL/perovskite interfaces under light exposure. Indeed, it was revealed that NiO<sub>x</sub> and PEDOT:PSS are the most aggressive HTLs undergoing some (photo)chemical reactions with complex lead halides. In particular, NiO<sub>x</sub> was shown to form NiI<sub>2</sub> via depletion of

iodide from organic AI species (A = MA or FA). On the contrary, polyarylamine-type HTLs such as PTA and PTAA were shown to be very inert to complex lead halides and, probably, even enhance the stability of their thin films due to defect passivation.<sup>129</sup> These results are quite important in the context of developing efficient p-i-n PSCs with fairly stable interfaces.

While studying different perovskite/HTL systems, we observed a number of interesting effects. Thus, it was shown that multication and, in particular, mixed halide perovskites tend to undergo light-induced crystallization. Moreover, we observed phase segregation of  $\beta$ -FAPbI<sub>3</sub> for many systems, which evidences the phase instability of multication perovskites. In that context, the situation is even worse with the mixed halide CsMAFAPb(BrI)<sub>3</sub> and CsFAPb(BrI)<sub>3</sub> perovskites, which undergo massive and practically irreversible halide phase segregation under light exposure. Such unfavorable phase dynamics are strongly impacted by the HTLs suggesting that the formation of defects at the interfaces facilitates these transitions.

It should be emphasized that light-induced absorber crystallization and halide phase segregation effects were essentially eliminated by depositing the top ETL coating of the fullerene derivative PC<sub>61</sub>BM. This coating also strongly suppressed the segregation of  $\beta$ -FAPbI<sub>3</sub> phase in the case of multication perovskites. These results suggest that both charge transport interlayers (HTL and ETL) can tune effectively the phase dynamics in absorber perovskite films.

Among all the studied perovskite absorbers, only MAPbI<sub>3</sub> showed stable operation in PSCs, while all multication and mixed halide perovskites showed a significant deterioration of the device performance presumably due to unfavorable phase dynamics leading to the trapping of charge carriers.

As a major conclusion from the performed studies, one has to focus on multiparametric optimization of all the device components and functional interfaces in order to reach long-term operational stability of PSCs. It is very likely that polymeric PTA and PTAA represent very promising HTLs components, while the perovskite absorber should have the simplest composition, e.g. MAPbI<sub>3</sub> or FAPbI<sub>3</sub>, in order to

avoid unfavorable cation- or anion-induced phase segregation effects ruining the device performance.

## **Chapter 4. Gamma rays induced halide phase segregation in the triple-cation perovskite solar cells**

### **4.1 Motivation**

In the previous chapters, we discussed mainly the photostability of PSCs. There is still big work to be done on the way to successful technology commercialization. However, based on current research and many other works going on around the world, there is a big chance that the issue of operation stability will be solved. If we assume that, a big variety of applications for PSCs arise on the horizon starting from mobile applications and traditional solar panels for households to space technologies. In this chapter, we tried to estimate the potential of PSCs as an absorber material for solar cells placed on satellites. For the space environment, solar cells should withstand very high radiation doses including gamma rays. High solar irradiation (up to 100 Sun), proton and electron irradiation was already found to be harmless for perovskite solar cells at ambient temperatures.<sup>100, 130, 131</sup> The impact of gamma rays is still poorly investigated, whereas this type of radiation has maximal penetration depth and the associated damage cannot be mitigated using encapsulation/shielding. Herein we explore the impact of gamma rays on the film morphology, crystal structure, and photovoltaic performance of the “triple-cation”  $\text{Cs}_{0.15}\text{MA}_{0.10}\text{FA}_{0.75}\text{Pb}(\text{Br}_{0.17}\text{I}_{0.83})_3$  perovskite solar cells. Hole-collecting bottom electrode, perovskite, and electron transport materials were evaluated with respect to their contribution to the overall solar cell degradation under exposure to gamma rays.

### **4.2 Materials and methods**

The radiation stability test was performed in 3 stages. Figure 45 shows the architectures of three sets of samples used in this work and the general methodology of

the performed experiments. At the first stage glass/ITO/PEDOT:PSS samples were exposed to 150, 300, and 500 Gy doses of gamma rays. Then the sets of reference non-exposed samples and the experimental samples exposed to the radiation were processed further in one batch under the same conditions to fabricate the complete solar cell architectures. Perovskite and then PC<sub>61</sub>BM layers were deposited by spin-coating inside the nitrogen glove box followed by deposition of Ag contacts by thermal evaporation in a high vacuum. At the 2<sup>nd</sup> stage glass/ITO/PEDOT:PSS/perovskite samples were exposed to 150, 300 and 500 Gy doses. (Figure 45b). The remaining layers were deposited after radiation exposure and before sample characterization. At the 3<sup>d</sup> stage glass/ITO/PEDOT:PSS/perovskite/PC<sub>61</sub>BM samples were exposed to 150, 300 and 500 Gy doses. (Figure 45c) and then similarly to previous stages were finished for solar cell characterization.

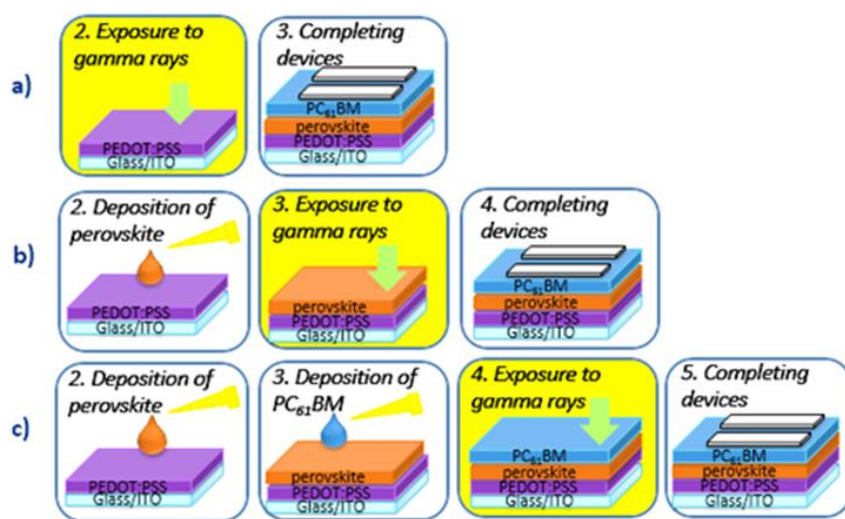


**Figure 45.** Architecture and workflow of investigated samples and general methodology of the experiment investigation: (a) Glass/ITO/PEDOT:PSS, (b) Glass/ITO/PEDOT:PSS/perovskite, (c) Glass/ITO/PEDOT:PSS/perovskite/PC<sub>61</sub>BM.

### *Film preparation*

Glass/ITO substrates (Kintek, 15 Ohm/sq.) were cleaned manually with toluene and acetone, sonicated in deionized water, acetone and isopropyl alcohol (IPA) for 10 min each, dried with air and subjected to additional plasma cleaning for 300 sec. A 1:1

solution of poly(3,4-ethylene dioxythiophene) polystyrene sulfonate (PEDOT:PSS, Clevios PH) in deionized water was deposited statically on the cleaned substrates and spin-coated at 3000 rpm for 20 sec. Subsequently, samples were annealed for 20 min at 165 °C in the air. The following procedures were performed entirely inside the nitrogen glove box to avoid exposure of the samples to the ambient atmosphere. 172.0 mg of formamidinium iodide (FAI), 507.1 mg of  $\text{PbI}_2$ , 22.2 mg of methylammonium bromide (MABr), and 73.4 mg of  $\text{PbBr}_2$  were dissolved in 1 mL of 4:1 DMF/DMSO solvent mixture. Separately 390.0 mg of CsI in 1 mL of DMSO was prepared and 70  $\mu\text{L}$  of that precursor was added to the mixture described above. The precursor solution was stirred for 2 hours at 75 °C for the complete dissolving of all the components. 25  $\mu\text{L}$  of the solution was deposited (dynamically) at 6000 rpm following by quenching with 60  $\mu\text{L}$  of toluene (dropped 55 sec after perovskite precursor) applied at the same spin-coating frequency. The deposited  $\text{Cs}_{0.15}\text{MA}_{0.10}\text{FA}_{0.75}\text{Pb}(\text{Br}_{0.17}\text{I}_{0.83})_3$  films were annealed for 3 min at 100 °C, which led to the development of a dark brown color. [6,6]-phenyl- $\text{C}_{61}$ -butyric acid methyl ester ( $\text{PC}_{61}\text{BM}$ ) was used as a traditional electron transport material in PSCs.  $\text{PC}_{61}\text{BM}$  (40 mg) was dissolved in 1 mL of chlorobenzene under stirring at 45 °C overnight and spin-coated at 2000 rpm. The samples were left for drying within 10 min inside the glove box before loading into the vacuum chamber for deposition of the top electrodes. Silver electrodes (100 nm) were evaporated in high vacuum ( $10^{-6}$  mbar) through a shadow mask defining the active area of each device as  $\sim 0.16 \text{ cm}^2$ .

#### *Radiation stability test*

Radiation stability tests were performed in parallel for three different sets of samples: Glass/ITO/PEDOT:PSS; Glass/ITO/PEDOT:PSS/perovskite and Glass/ITO/PEDOT:PSS/ perovskite/ $\text{PC}_{61}\text{BM}$ . The prepared samples were packed in three layers of Al lamination foil (used to form cases for pouch-type Li-ion batteries) inside the argon glove box. Note that the packaging material was transparent for gamma rays. Each set consisted of 10 samples, which were exposed to 100, 200, 300, 400, and 500 Gy (2 samples per dose) with  $^{137}\text{Cs}$  gamma ray source ( $E_\gamma = 662 \text{ keV}$ ) with a dose rate of 2.5 Gy/min. Two reference samples were left fresh, packed, and exposed to the

ambient atmosphere for the same time as irradiated samples. After exposure of the samples to gamma rays (or to the ambient atmosphere for the reference ones), they were introduced back in the glove box and the package was opened under the inert atmosphere. The samples (irradiated + reference) were further processed in one batch as described in the previous section to complete the p-i-n type perovskite solar cells of the following architecture: Glass/ITO/PEDOT:PSS/perovskite/PC<sub>61</sub>BM/Ag. The characterization of the devices was performed as described above.

#### *Film and solar cell characterization*

Samples with thin-films were analyzed using UV-vis, XRD, XPS, PL, and AFM tools. The current-voltage characteristics of the devices were measured using Advantest 6240A source-measurement unit. The detailed information about these methods can be found in the Materials and Methods section in Chapter 2.3.

### **4.3 Gamma rays induced halide phase segregation in perovskite solar cells and thin films**

Since PSCs represent multilayer stacks, each of the layers can potentially contribute to the device degradation. Therefore, we systematically explored the influence of gamma rays to the glass/ITO/PEDOT:PSS electrodes, perovskite absorber material, and PC<sub>61</sub>BM electron transport layer. Radiation doses in the range of 0-500 Gy were applied to the samples since 100-1000 Gy represents a typical stability benchmark for satellites working at low and middle equatorial orbits.<sup>65</sup> The mixed “triple-cation” Cs<sub>0.15</sub>MA<sub>0.10</sub>FA<sub>0.75</sub>Pb(Br<sub>0.17</sub>I<sub>0.83</sub>)<sub>3</sub> perovskite formulation (designated as “perovskite” below) was chosen because it shows high solar cell efficiencies and superior operation stability according to the available literature data.<sup>76-79</sup> Notably, the devices fabricated using exposed and the reference non-exposed glass/ITO/PEDOT:PSS samples demonstrated nearly the same PCEs of about 9.5-10.5% (Figure 46). The photovoltaic characteristics of all the samples were within the standard experimental data deviation window and showed no correlation with the radiation dose. These results allowed us to conclude that the glass substrate with the bottom ITO/PEDOT:PSS hole-

collecting electrode is fully stable with respect to the radiation and, therefore, should not contribute to the device degradation nor measured solar performance.

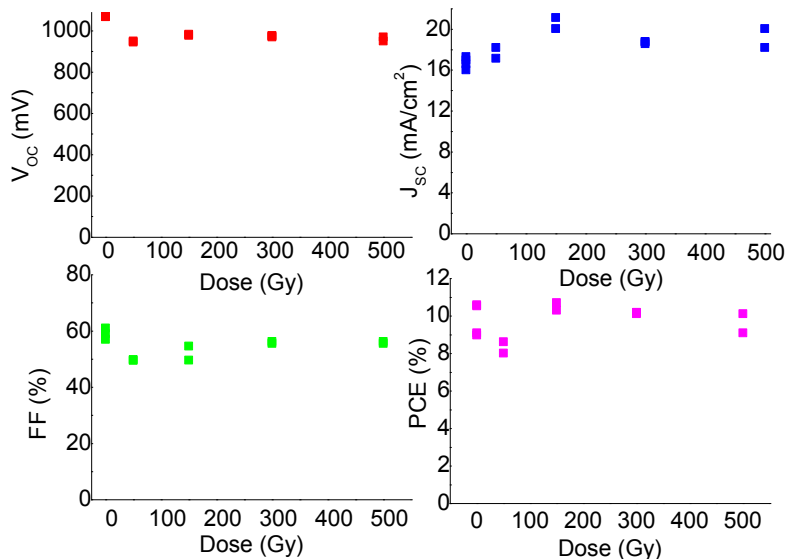


**Figure 46.** Performance characteristics of the devices based on the glass/ITO/PEDOT:PSS samples exposed to gamma rays as a function of the radiation dose.

The second set of samples (Figure 45b) exposed to gamma rays comprises the perovskite layer deposited on top of the glass/ITO/PEDOT:PSS stacks. Since the lead halide complexes form crystalline films, first we have applied XRD analysis to check for any phase composition changes caused by gamma radiation. Both exposed and reference samples (Figure 47) were encapsulated by spin-coating polystyrene films inside the glove box and then were measured in an ambient atmosphere for 10-15 min. It should be noticed that the XRD pattern of the analyzed material matches well the pattern of previously reported  $(\text{MAPbBr}_3)_{0.15}(\text{FAPbI}_3)_{0.85}$  perovskite showing differences only in the peak intensities probably due to different textural effects.<sup>80</sup> Therefore, the  $(\text{MAPbBr}_3)_{0.15}(\text{FAPbI}_3)_{0.85}$  XRD pattern was used as a reference one to analyze the experimental patterns of the perovskite films obtained in this work.

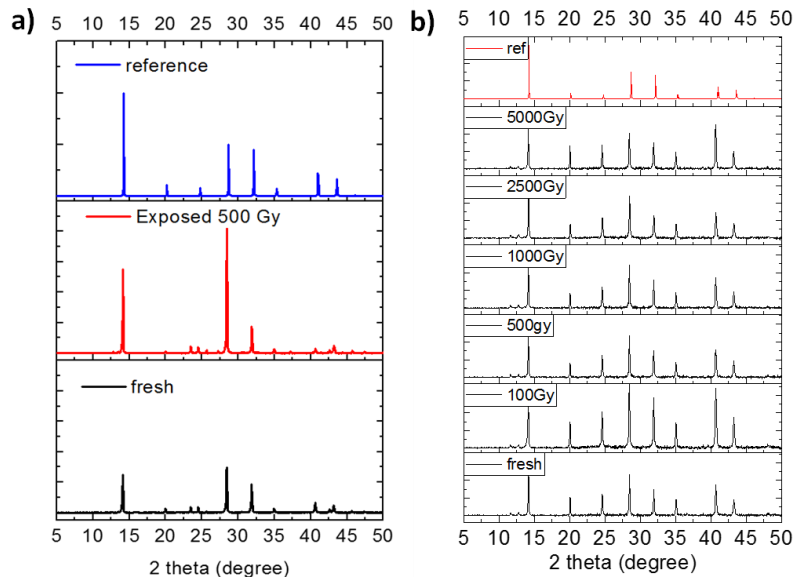


**Figure 47.** XRD patterns of the reference and 500 Gy exposed Glass/ITO/ PEDOT:PSS/ perovskite/PC<sub>61</sub>BM samples (a) and glass/perovskite samples exposed to 0-5000 Gy (b). The reference XRD pattern of MAPbI<sub>3</sub> films is shown for comparison.

XRD data presented in Figure 47a show that gamma rays have no real impact on the phase purity of the perovskite films. No additional peaks indicating the appearance of the decomposition products (e.g. PbI<sub>2</sub> or metallic Pb) or some phase transitions effects were observed. Moreover, there were essentially no changes in the XRD patterns of the glass/perovskite samples exposed to high doses of gamma rays (up to 5000 Gy, Figure 47b), which suggested that the triple-cation perovskite formulation investigated in this work is resistant to radiation.

These XRD data were fully in line with the results of the XPS measurements. The XPS survey spectra (Figure 48a) of all exposed samples were virtually identical and matching the spectrum of the pristine perovskite. Zooming the N 1s and Pb 4f<sub>7/2</sub> signatures (Figure 48b, c) also showed almost no impact of the radiation except for some band broadening observed for the sample exposed to the highest dose of 5000 Gy.

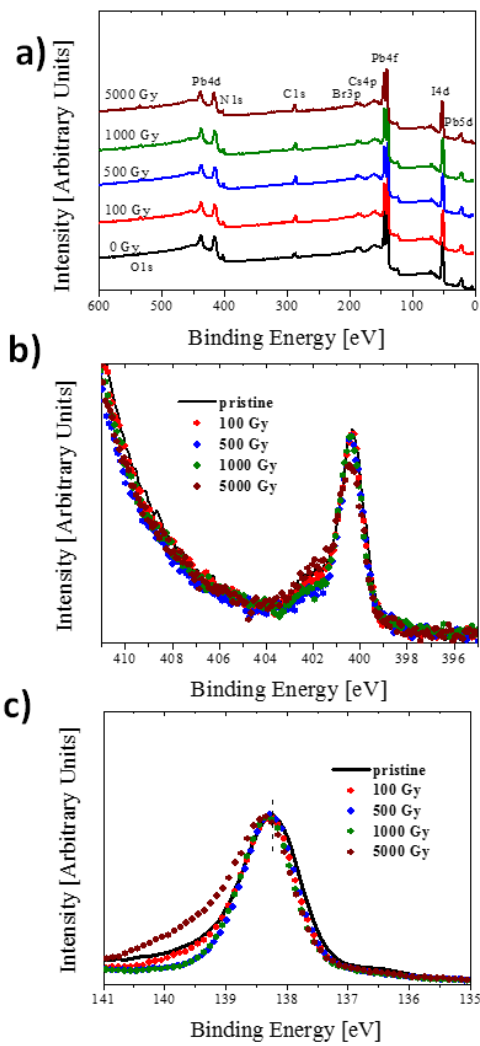


**Figure 48.** XPS survey spectra (a) and zoomed areas of the N 1s (b) and Pb 4f<sub>7/2</sub> (c) of pristine perovskite film and the films exposed to 100-5000 Gy doses of gamma rays.

This peak broadening might be related to some partial decomposition of the material (which is unlikely considering the XRD and optical spectroscopy data, see below) or to the radiation-induced gradients in the composition of the material (e.g. phase separation of I-rich and Br-rich domains). Thus, the main message provided by the XPS data is the good radiation stability of the used triple-cation perovskite formulation.

Scanning probe microscopy was used to explore the potential impact of gamma radiation on the surface morphology and electronic properties of the perovskite films. In particular, the contact potential (surface potential) was measured by 2-pass amplitude-modulated Kelvin Probe Force Microscopy (AM-KPFM). The topography and surface potential images for the glass/ITO/PEDOT:PSS/perovskite samples (exposed to 500 Gy and reference) are shown in Figure 49.

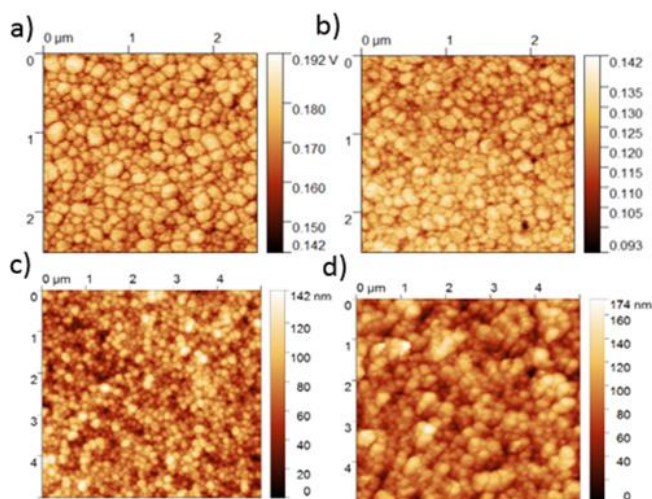


**Figure 49.** Surface potential (a, b) and topography (c,d) images of the reference (a,c) and exposed to 500 Gy (b, d) Glass/ITO/PEDOT:PSS/perovskite samples.

Gamma radiation-induced a minor change in the surface work function of the films from 4.67 eV to 4.72 eV, which might be related to the formation of the acceptor-type defects or ion vacancies. Topography images show that the samples exposed to 500 Gy have considerably larger grains (15 nm vs. 10 nm in non-exposed samples) and rougher surface (22 nm vs. 18 nm). We believe that radiation induces crystallization of the perovskite material leading to the growth of the grains in the samples and an increase in the film roughness though this hypothesis requires more systematic study.

The effect of gamma radiation on the optical properties of the perovskite films was investigated by monitoring their UV-vis and PL spectra as a function of the radiation dose. The UV-vis spectra did not noticeably change with exposure to gamma radiation. In particular, no notable radiation-induced change in the relative intensity of

the existing or appearance of any new absorption features was observed even when the doses were as high as 2500-5000 Gy.

On the contrary, PL spectra of the perovskite films revealed a considerable enhancement in the intensity of the emission bands, significant changes in their shape, and notable shifts (by ~5 nm) of the maxima towards longer wavelengths following the increase in the radiation dose (Figure 50a).

It should be emphasized that the gamma rays-induced changes in the emission spectra were essentially reversible: repeating the measurements 2 weeks after radiation exposure revealed only three times stronger PL intensity for 5000 Gy exposed samples, while the red-shift of the bands completely disappeared (Figure 51b).

The observed PL dynamics are inconsistent with the expected radiation-induced defect (trap) formation mechanism, which should result in a severe quenching of the photoluminescence. However, the increase in the PL intensity and red-shift of the emission bands were both well-documented for the mixed halide perovskite films exposed to light and are known in the literature as “Hoke effect”.<sup>125,126,132</sup> We explored the PL dynamics of the triple-cation perovskite films under illumination with the green laser (532 nm). Indeed, the films demonstrated very characteristic behavior reflected in the steady enhancement of the PL intensity while increasing the laser light exposure time from 30 s to 30 min. Finally, we observed three times more intense emission than for pristine films, while the maximum of the emission band shifted from 770 to 778 nm (Figure 50b). The samples deposited on glass substrates demonstrated a 10-fold increase in the PL intensity over 13 min of laser exposure and red-shifting of the emission band by 18 nm (Figure 51c).

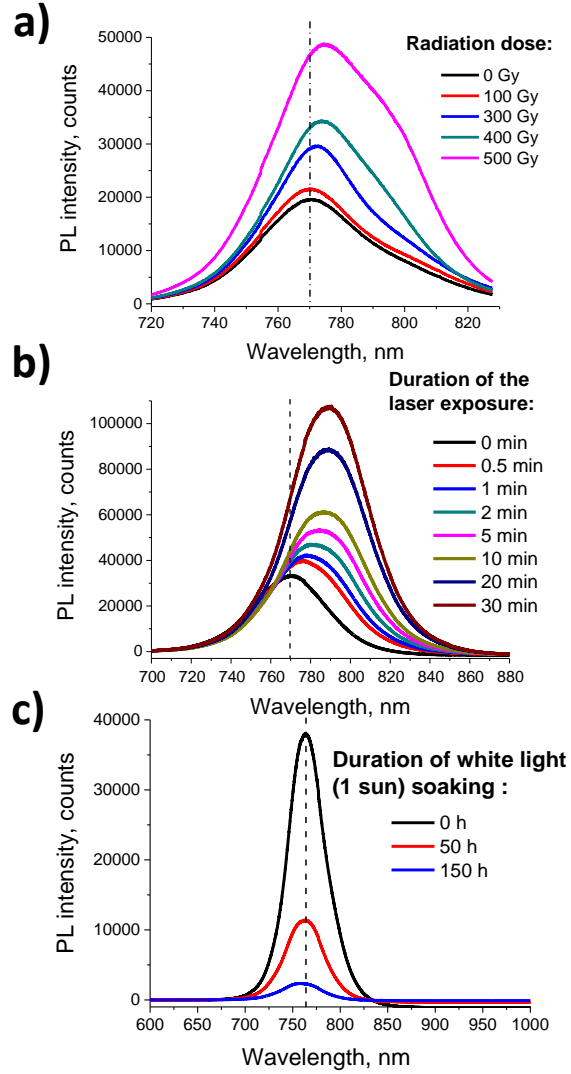


**Figure 50.** PL spectra of glass/ITO/PEDOT:PSS/perovskite films measured at least 1 h after exposure to gamma rays with the doses of 0-500 Gy (a) and green laser light (532 nm, 0.238 mW)(b) demonstrating the dynamics characteristic for the Hoke effect. PL spectra of the perovskite films exposed to white light illumination (100 mW/cm<sup>2</sup>, a nitrogen atmosphere) revealing the photochemical degradation of the films accompanied by the quenching of the photoluminescence due to trap formation (c).

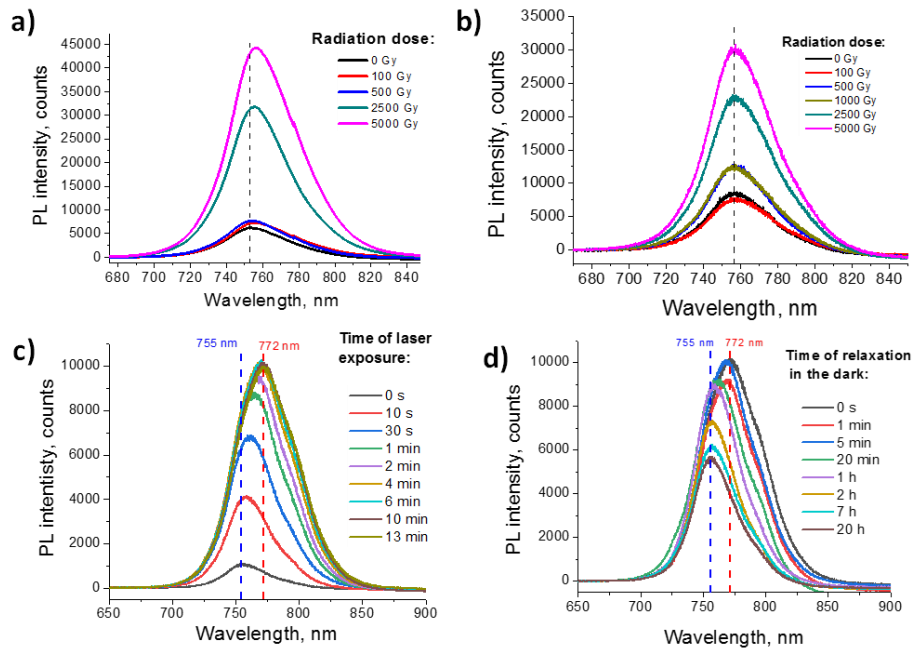


**Figure 51.** PL dynamics in the perovskite films induced by gamma rays (a-b) and green (532 nm) laser (c-d). Strong increase in the PL intensity accompanied by the red-shift of the emission band maximum as revealed 1 h after the radiation exposure (a) and the spectra of the same samples measured 2 weeks later showing a significant relaxation of the gamma rays-induced effects (b). Laser-induced PL dynamics in the perovskite sample characteristic for the Hoke effect (c) and its relaxation while storing the sample in the dark (d).

In particular, the sample exposed to 500 Gy demonstrated an unsymmetrical emission band with more than twice higher intensity (especially in the 785-820 nm range) as compared to the spectrum of the pristine sample. Moreover, exposing the perovskite films deposited on glass substrates to higher doses of radiation resulted in even more pronounced enhancement of the luminescence: 5- and 7-fold increases were observed by applying 2500 Gy and 5000 Gy, respectively (Figure 51a).

The relaxation of the light-induced changes was monitored while keeping the samples in the dark and measuring their PL spectra with a short (<0.1 s) exposure to the laser illumination. The maximum of the emission band shifted by 13 nm to shorter wavelengths within 1 h of storage of the samples in the dark, leaving just 4 nm offset with the spectrum of the pristine sample (Figure 51d). Such relatively fast reverse

transition explains why only the 5 nm red-shift was observed in the spectra of the 500 Gy exposed samples vs. pristine perovskite films since the PL measurements could be done only 1 h after the radiation experiment (due to the safety issues and different locations of these facilities). One can assume that measuring PL spectra immediately after the radiation exposure might reveal much stronger red-shifts of the emission bands like observed under laser light exposure.

The light-induced PL dynamics in the mixed halide perovskites are usually associated with the reversible phase segregation of I-rich and Br-rich (or Cl rich) domains. Considering the fact that the mechanism of the Hoke effect is still under active debates,<sup>133</sup> it is very challenging to draw any mechanistic correlations between the well-established visible-light-induced PL dynamics and the revealed in this work behavior of the samples exposed to gamma-rays. One might assume that both visible light and, particularly, gamma rays create some defects in the perovskite films, which become very luminescent due to some reason. For instance, the highest PL quantum yields are reached for perovskite quantum dots or thin films with very small grain size or 2D perovskite-like materials, which is explained by quantum confinement effects.<sup>134,135</sup> So, moderate aging of the perovskite films might reduce the effective domain size and lead to enhanced and, probably, even red-shifted photoluminescence. To verify this hypothesis, we deposited thin perovskite films on glass substrates (to avoid any interfacial effects with PEDOT:PSS and ITO) and exposed them to white light illumination under inert atmosphere inside the glove box. Figure 50c shows that white light leads to photodegradation of the material accompanied by quenching of the photoluminescence and even some minor blue-shift of the emission band. The XRD data indicated the formation of metallic lead impurity in the perovskite films exposed to the white light, which evidenced their partial photochemical decomposition (Figure 52).

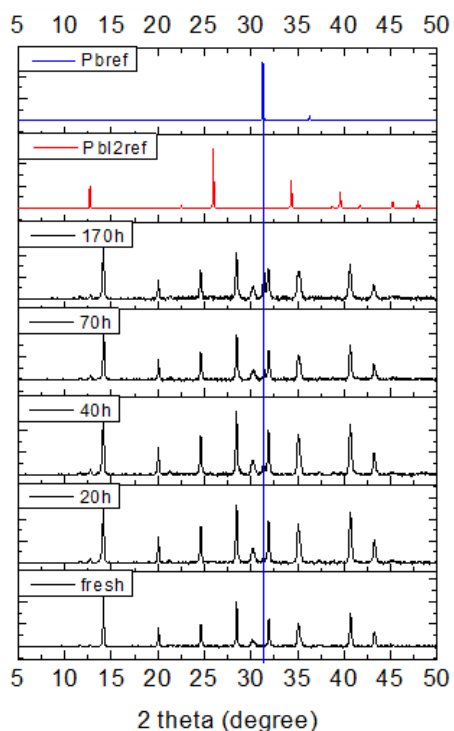


**Figure 52.** The dynamics of the XRD patterns for the Glass/perovskite sample exposed to white light illumination inside under inert atmosphere the glove box. The vertical blue line highlights the appearance of the peak characteristic for metallic lead Pb(0).

The obtained results strongly suggest that the reversible PL dynamics discussed above most probably has nothing similar to the irreversible light-induced decomposition. Most probably, both visible light and gamma rays promote phase segregation of I-rich and Br-rich domains. To the best of our knowledge, such a gamma radiation-induced Hoke effect has never been observed and reported before. It should be emphasized that halogen-induced phase segregation promoted by gamma rays might represent an important degradation pathway of the perovskite-based photovoltaic devices limiting their employment in space applications.

While continuing this study, we explored the effect of the fullerene-based PC<sub>61</sub>BM ETL on the radiation stability of the Glass/ITO/PEDOT:PSS/perovskite/ PC<sub>61</sub>BM stack (third set of samples, Figure 45c). Shortly, the layer of the fullerene derivative has a very minor (if any) effect on the behavior of the perovskite absorber exposed to gamma

rays. XRD analysis and UV-vis spectra revealed no changes just confirming the high stability of the perovskite films under gamma rays exposure. Regardless of the fact that PC<sub>61</sub>BM layer quenches PL of the perovskite absorber, we can still observe the exposure-dependent increase in the PL intensity and shift of the PL maximum to the longer wavelengths (Figure 53).

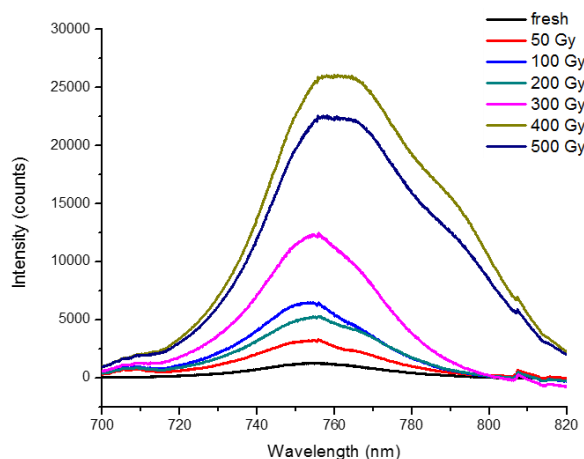


**Figure 53.** Photoluminescence spectra of glass/ITO/PEDOT:PSS/perovskite/PC<sub>61</sub>BM films exposed to 0-500 Gy.

KPFM revealed a minor rise in the surface work function of the films from 5.00 eV to 5.04 eV after 500 Gy exposure (Figure 54a-b). Moreover, the roughness of the PC<sub>61</sub>BM films has slightly increased from 3.8 nm to 5.1 nm. It should be noted that gamma rays exposure stimulated the formation of pinholes in the PC<sub>61</sub>BM layer as can be seen from the topography images (Figure 54c-d).

At the final stage of this work, we explored the effect of gamma radiation on the photovoltaic performance of the perovskite (active layer absorber) and PC<sub>61</sub>BM ETL films. The investigated sets of the reference and irradiated glass/ITO/PEDOT:PSS/perovskite and glass/ITO/PEDOT:PSS/perovskite/PC<sub>61</sub>BM samples were processed further by depositing PC<sub>61</sub>BM (in case of the first set) and evaporating top Ag contacts to complete solar cell architecture presented in Figure 45. The fabricated solar cells were characterized by standard current JV and EQE measurements.

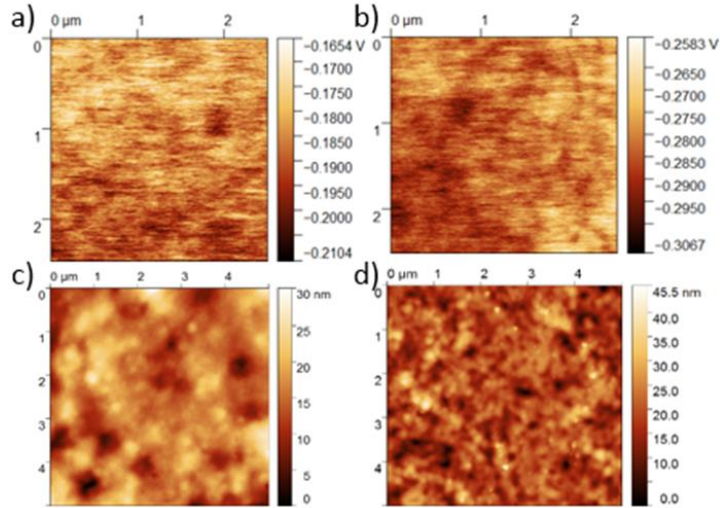


**Figure 54.** Surface potential (a, b) and topography (c,d) images of the reference (a,c) and exposed to 500 Gy (b, d) Glass/ITO/PEDOT:PSS/perovskite/PC<sub>61</sub>BM samples.

Figure 55 shows the evolution of the device characteristics as a function of the gamma radiation dose for both types of samples. Exposure of the glass/ITO/PEDOT:PSS/perovskite films to 500 Gy resulted in the decrease of PCE from ~10.2 to ~7.0% mainly due to the drop in the  $J_{SC}$  from ~18 to ~13 mA/cm<sup>2</sup>.

Somewhat stronger degradation was observed for the glass/ITO/PEDOT:PSS/perovskite/PC<sub>61</sub>BM samples: PCE decayed from >10 to ~6.0% and  $J_{SC}$  decreased from ~18 to ~11 mA/cm<sup>2</sup> as also supported by EQE measurements. All the  $J_{SC}$  values extracted from JV measurements were reconfirmed by the integration of the EQE spectra against the standard AM1.5G solar spectrum. Interestingly, FF and particularly  $V_{OC}$  remained almost unaffected by gamma radiation for both types of samples, which indicates that the main degradation mechanism is not related to the trap formation. The appearance of the traps usually increases the density of states in the gap, which leads to the  $V_{OC}$  losses.<sup>136,137</sup> We strongly believe that the device degradation is mainly induced by the radiation-induced halide phase segregation similar to the Hoke effect.<sup>125</sup> However, the light-induced phase segregation usually leads to the formation of recombination centers and causes a reduction in  $V_{OC}$ .<sup>125</sup> In our case, we do not see

any  $V_{OC}$  changes, so the mechanism of gamma ray-induced Hoke effect is still requiring additional studies to be completely understood. We also cannot exclude some contribution of the radiation-induced substrate darkening in decrease of the device  $J_{SC}$ , which we found later and discuss below.

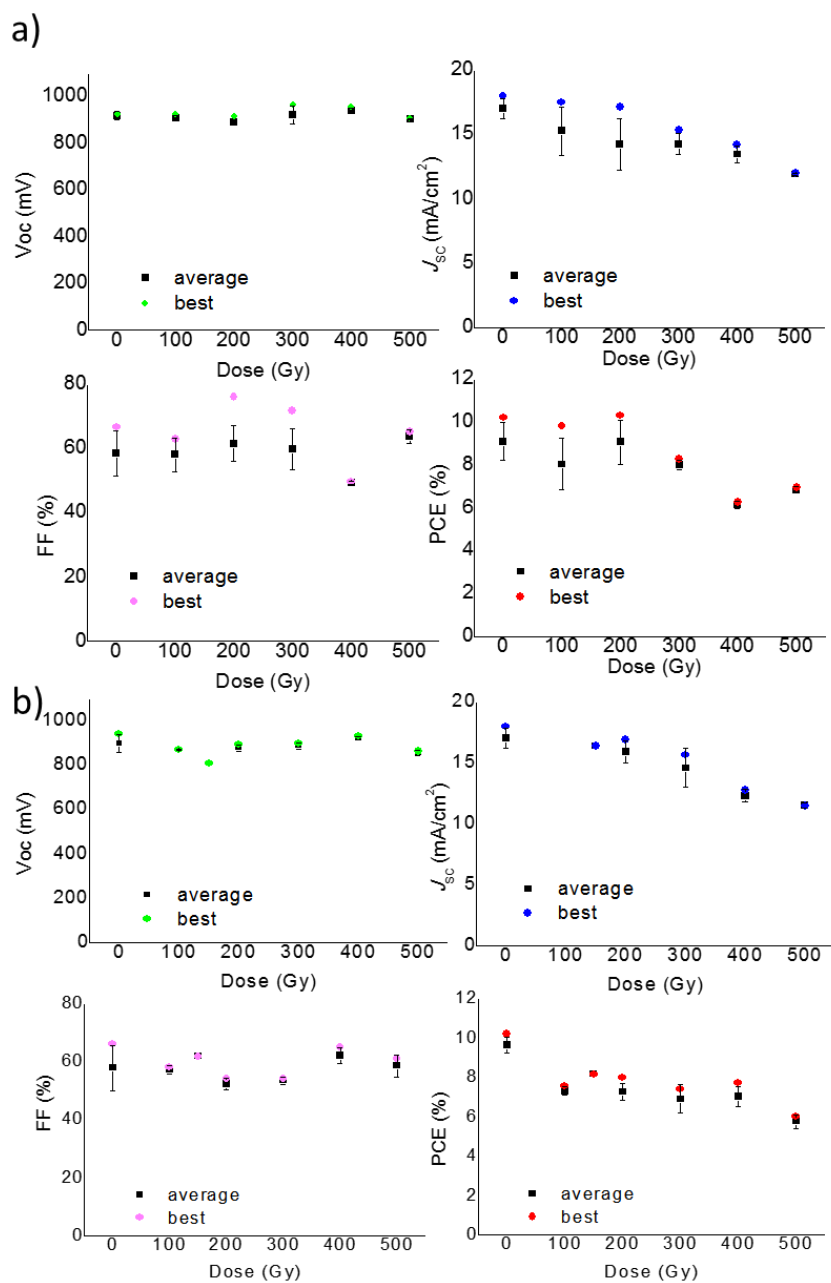


**Figure 55.** Performance characteristics as functions of the radiation dose delivered to the glass/ITO/PEDOT:PSS/perovskite (a) and glass/ITO/PEDOT:PSS/perovskite/PC<sub>61</sub>BM (b) samples.

Particularly interesting is the fact, that PC<sub>61</sub>BM does not stabilize the perovskite layer with respect to the action of gamma rays and, on the contrary, contributes to the overall degradation of the system. This observation suggests that PC<sub>61</sub>BM is intrinsically unstable with respect to radiation exposure. To verify this hypothesis we exposed a bulk sample of PC<sub>61</sub>BM to a high dose of gamma rays (5000 Gy) and then applied it as electron transport material in the ITO/PEDOT:PSS/perovskite/PC<sub>61</sub>BM/Ag solar cells (note that PC<sub>61</sub>BM was the only device component exposed to radiation in that case). Figure 56 shows that the solar cells comprising exposed PC<sub>61</sub>BM deliver notably lower current densities and power conversion efficiencies as compared to the reference devices fabricated using pristine PC<sub>61</sub>BM sample. The origin of the radiation-induced degradation of PC<sub>61</sub>BM remains unclear, though gamma rays induced polymerization, cage rapture and formation of radicals can be suspected according to the previously performed comprehensive studies of the radiation chemistry of fullerenes.<sup>138</sup>

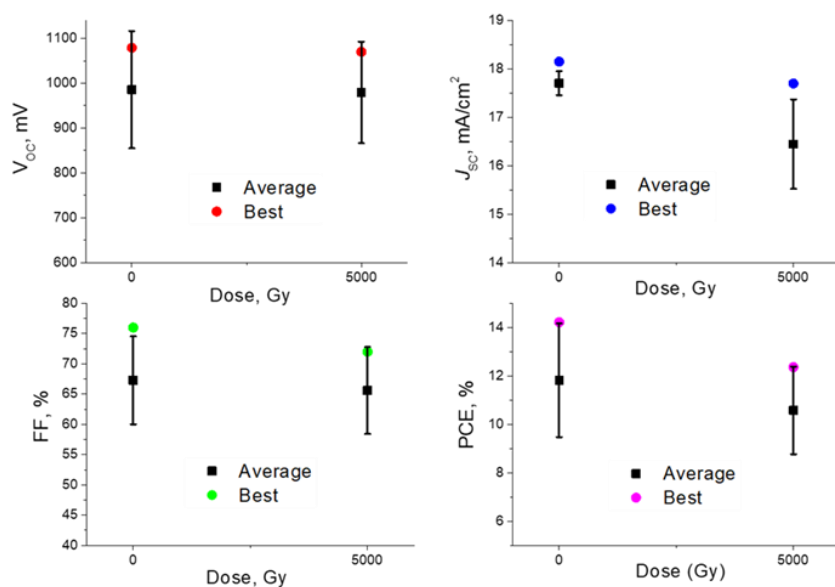


**Figure 56.** Characteristics of p-i-n glass/ITO/PEDOT:PSS/perovskite/PC<sub>61</sub>BM/Ag solar cells fabricated using two different batches of PC<sub>61</sub>BM: pristine (left column) and exposed to 5000 Gy of gamma rays (right column).

#### 4.4 Summary

To summarize, we investigated the impact of gamma radiation on the behavior of the complex lead halide  $\text{Cs}_{0.15}\text{MA}_{0.10}\text{FA}_{0.75}\text{Pb}(\text{Br}_{0.17}\text{I}_{0.83})_3$  perovskite solar cells in order to estimate the potential of such devices for space applications. It was shown that the doses up to 500 Gy do not damage the hole collecting bottom electrode glass/ITO/PEDOT:PSS. However, radiation affects significantly the perovskite absorber and the electron transport  $\text{PC}_{61}\text{BM}$  layers. The main contribution to solar cell degradation comes from the severe photocurrent losses (25-35% of the initial value) suggesting the accumulation of the radiation-induced defects reducing photocurrent. These defects most likely originate from the halide phase segregation induced by high radiation doses, which we observed here for the first time. Therefore, the current generation of the perovskite materials probably has insufficient radiation stability for considering application into space technologies. However, rapid progress in the field of perovskite photovoltaics sooner or later will bring a new generation of absorber materials showing significantly improved radiation stability. These studies might provide the impetus for developing scalable and high-performance applications of perovskite solar cells in space missions.

## Chapter 5. Unraveling the material composition effects on gamma ray stability of lead halide perovskite solar cells

### 5.1 Motivation

The previous Chapter showed that mixed halide systems are not suitable for space applications, as they undergo halide phase segregation under gamma ray exposure. I decided to check how would behave pure iodide and bromide systems in similar conditions. We selected six different perovskite compositions: MAPbI<sub>3</sub>, MAPbBr<sub>3</sub>, Cs<sub>0.15</sub>FA<sub>0.85</sub>I<sub>3</sub>, Cs<sub>0.1</sub>MA<sub>0.15</sub>FA<sub>0.75</sub>PbI<sub>3</sub>, CsPbI<sub>3</sub>, and CsPbBr<sub>3</sub> and tested their radiation hardness in thin films and completed solar cells. To the best of our knowledge, none of them were studied with respect to their tolerance to gamma-rays exposure.

### 5.2 Materials and methods

#### *Preparation of thin films and photovoltaic cells:*

Glass/ITO substrates (Kintek, 15 Ohm/sq.) were cleaned manually as reported elsewhere.<sup>35</sup> SnO<sub>2</sub> 15 wt. % suspension from Alfa-Aesar (stock) was diluted to 10 wt. % with water and sonicated for 5 minutes. After solution filtration via a 0.45 mm PES filter, SnO<sub>2</sub> was spincoated twice at 4000 rpm in air. Substrates with SnO<sub>2</sub> were annealed at 160 °C for 15 minutes and transferred to the glovebox. A solution of PCBA in chlorobenzene (0.7 mg/ml) was deposited at 3000 rpm on samples and annealed at 100 °C for 5 min.

#### *Perovskite solution preparation:*

MAPbI<sub>3</sub> solution was prepared by mixing PbI<sub>2</sub> and MAI powders in stoichiometric amounts and dissolving in DMF:DMSO (80:20) mixed solvent to achieve 1.4 M concentration. A similar procedure was used for MAPbBr<sub>3</sub> solution by mixing PbBr<sub>2</sub> and MABr powders. A solution of Cs<sub>0.15</sub>FA<sub>0.85</sub>PbI<sub>3</sub> was prepared by mixing equal molar quantities of PbI<sub>2</sub> and univalent cation iodides CsI and FAI (15:85 mole ratio). For Cs<sub>0.1</sub>MA<sub>0.15</sub>FA<sub>0.75</sub>PbI<sub>3</sub>, the components CsI, MA, and FAI were taken in 10:15:75 molar ratio and combined with the stoichiometric amount of PbI<sub>2</sub>. All filtered solutions were

deposited in glovebox at 4000 rpm followed by quenching with toluene antisolvent after 16 sec. MAPbI<sub>3</sub> and MAPbBr<sub>3</sub> films were annealed at 85 °C for 3 min, while multication perovskites - at 120 °C for 3 min. CsPbI<sub>3</sub> and CsPbBr<sub>3</sub> films were deposited by co-evaporation of stoichiometric amounts of CsI and PbI<sub>2</sub> or CsBr and PbBr<sub>2</sub>, respectively, to achieve 400 nm thickness. PTA solution (4 mg/ml) in toluene was heated at 100 °C and deposited at 1000 rpm. MoO<sub>3</sub> was evaporated on top of PTA in the vacuum chamber (10<sup>-6</sup> mbar) to achieve 7-10 nm film thickness. Aluminum electrodes (100 nm) were evaporated in high vacuum (10<sup>-6</sup> mbar) through a shadow mask defining the active area of each device as ~0.16 cm<sup>2</sup>.

#### *Radiation stability test*

Radiation stability tests were performed in parallel for glass/perovskite thin films and the following types of PSCs:

Glass/ITO/SnO<sub>2</sub>/PCBA/MAPbI<sub>3</sub>/PTA/MoO<sub>3</sub>/Al;

Glass/ITO/SnO<sub>2</sub>/PCBA/MAPbBr<sub>3</sub>/PTA/MoO<sub>3</sub>/Al;

Glass/ITO/SnO<sub>2</sub>/PCBA/Cs<sub>0.15</sub>FA<sub>0.85</sub>PbI<sub>3</sub>/PTA/MoO<sub>3</sub>/Al;

Glass/ITO/SnO<sub>2</sub>/PCBA/Cs<sub>0.1</sub>MA<sub>0.15</sub>FA<sub>0.75</sub>PbI<sub>3</sub>/PTA/MoO<sub>3</sub>/Al;

Glass/ITO/SnO<sub>2</sub>/CsPbI<sub>3</sub>/PTA/MoO<sub>3</sub>/Al;

Glass/ITO/SnO<sub>2</sub>/CsPbBr<sub>3</sub>/PTA/MoO<sub>3</sub>/Al;

Thin films were exposed to the gamma rays doses of up to 5000 Gy, solar cells – up to 10000 Gy. More information about radiation experiments can be found in Material and Methods in Chapter 4.3.

#### *Film and solar cell characterization*

Samples with thin-films were analyzed using UV-vis, XRD, XPS, PL, and AFM tools. IV characteristics of solar cells were measured with Advantest 6240A source-measurement unit. The detailed information about these methods can be found in the Materials and Methods section in Chapter 2.3.

### **5.3 Gamma ray stability of perovskite materials in thin films**

In the first part of this work, we explored the behavior of single-layer perovskite films deposited on glass substrates. Such samples were exposed to gamma-rays with

doses ranging from 100 to 5000 Gy and analyzed by XRD, XPS, UV-vis, and PL measurements. The obtained results are presented in Figure 57 and Figure 58.

The Pb 4f-spectra of MAPbI<sub>3</sub> samples (Figure 57a) show a high-energy shift in the direction of the reference PbI<sub>2</sub> thus suggesting a partial decomposition of the material with the loss of organic component MAI under gamma-ray doses above 1000 Gy. This conclusion is also supported by XPS N 1s spectra (Figure 58), showing the gradual depletion of nitrogen from the films. Importantly, XRD patterns of the exposed films showed no detectable amounts of PbI<sub>2</sub> (Figure 58). Therefore, the PbI<sub>2</sub> formation occurs at the surface, which makes it visible for XPS, probing only the upper layers of the film, and not detectable for XRD, which is a bulk analysis technique.

Similarly, the XPS spectra of CsPbI<sub>3</sub> showed clearly the formation of Pb<sup>0</sup> on the film surface correlating with a dose of the gamma rays (Figure 57a), while no signatures of metallic lead were found in XRD (Figure 58c). XPS Cs 3d and VB spectra showed just minor changes suggesting that radiation exposure is not affecting CsI incorporated in CsPbI<sub>3</sub> (Figure 58). Interestingly, the decomposition of CsPbI<sub>3</sub> goes to metallic lead rather than to PbI<sub>2</sub>, which is formed under the same conditions from MAPbI<sub>3</sub>. Most likely, the observed difference is related to the fact that MAPbI<sub>3</sub> can release volatile products from the organic MAI component, which makes it a predominant decomposition pathway. On the contrary, CsPbI<sub>3</sub> cannot release organic volatiles, so degradation goes further to Pb<sup>0</sup> and presumably molecular iodine I<sub>2</sub>.

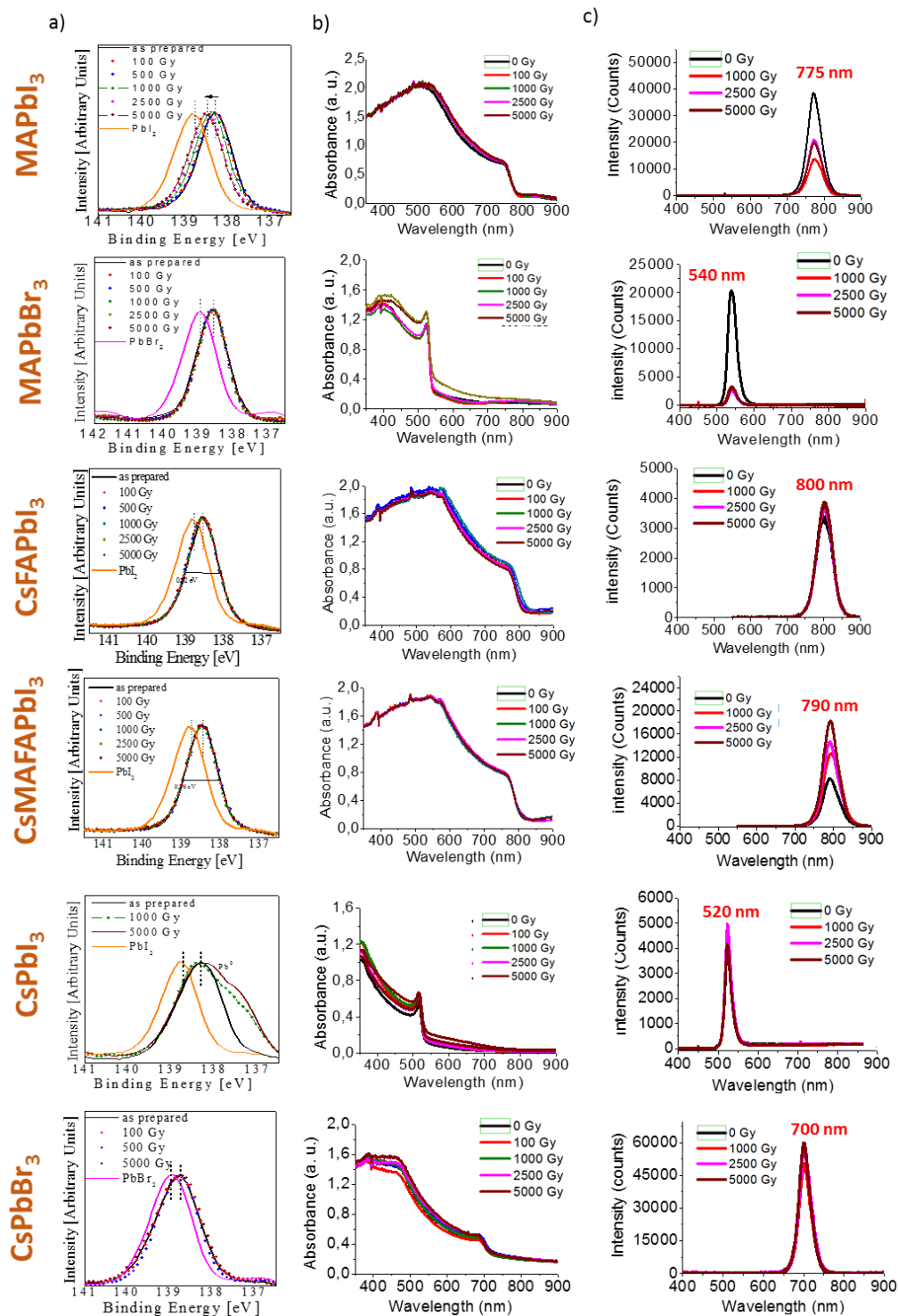


**Figure 57.** Evolution of XPS Pb 4f (a), UV-vis (b), and PL spectra (c) of thin perovskite films under gamma rays exposure (100 -500 Gy).

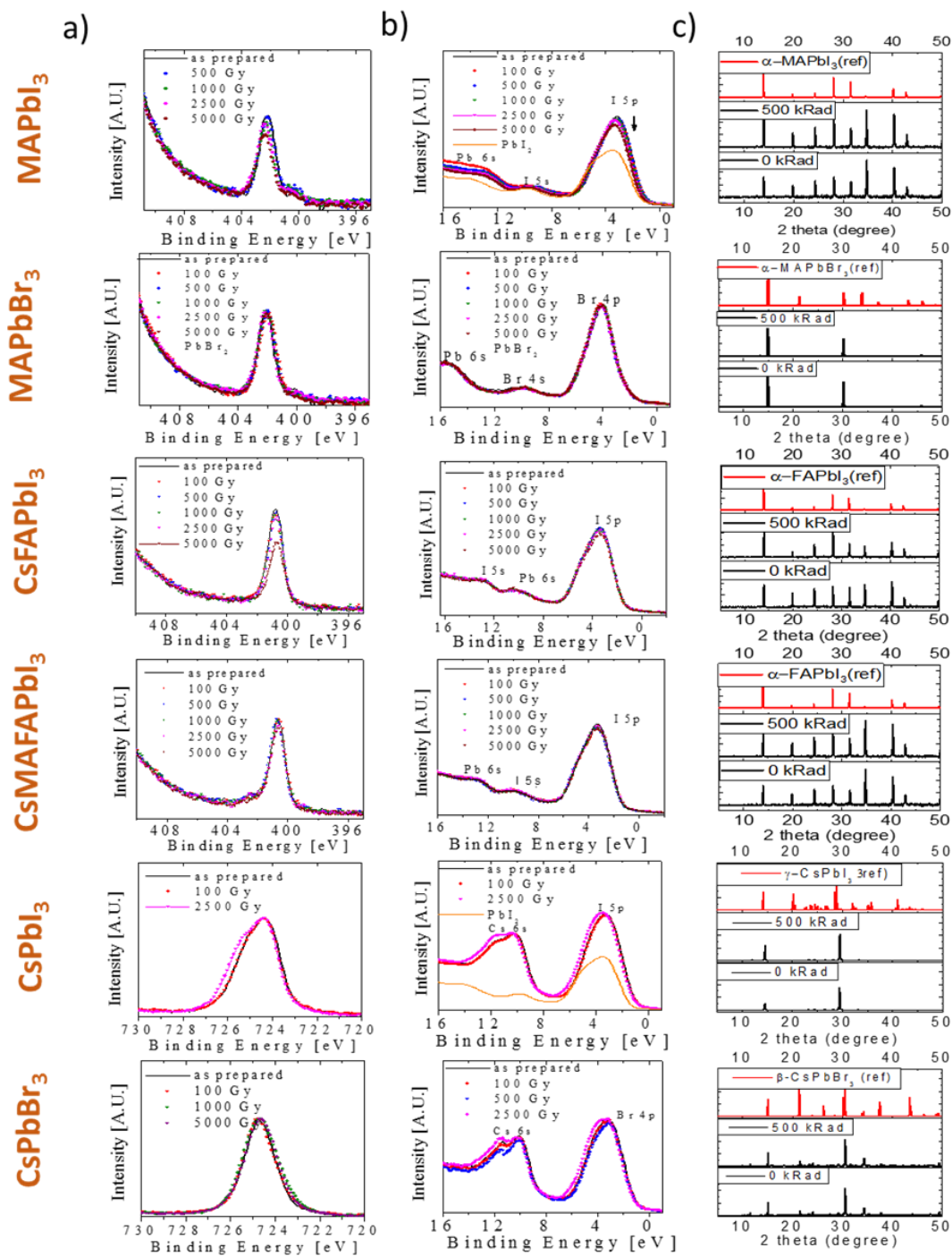


**Figure 58.** Evolution of XPS N 1s spectra (a), VB spectra (b) and XRD (c) of thin perovskite films under gamma ray exposure (100 -5000 Gy).

These findings correlate with the solar light-induced decomposition pathways reported for these perovskites recently.<sup>43</sup> Finally, it should be mentioned that XPS spectroscopy and XRD revealed no radiation-induced damage for MAPbBr<sub>3</sub>, Cs<sub>0.15</sub>FA<sub>0.85</sub>PbI<sub>3</sub>, Cs<sub>0.1</sub>MA<sub>0.15</sub>FA<sub>0.75</sub>PbI<sub>3</sub>, and CsPbBr<sub>3</sub> films.

While considering the UV-vis spectra (Figure 57b), one can notice that only wide-bandgap bromoplumbate systems show a significant evolution of the optical properties, while CsPbI<sub>3</sub> films exhibited just minor changes. On the contrary, the spectra of all narrow bandgap iodoplumbates with the absorption offset above 800 nm remain virtually unchanged. The observed correlation between the spectral changes and the material bandgap suggested that an increase in the absorption at short wavelengths might be caused by glass darkening.

To check this hypothesis, we explored the behavior of pristine glass substrates under exposure to gamma-rays. Figure 59 shows the evolution of the glass transmittance after receiving the 10000 Gy dose and the visual appearance of the samples after the radiation exposure.

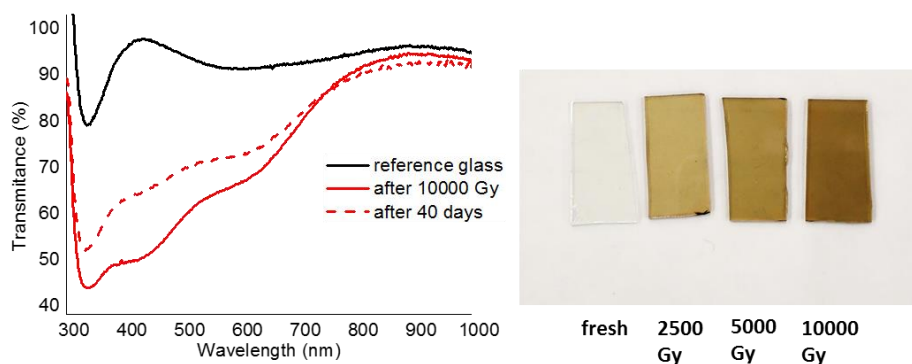


**Figure 59.** Evolution of glass substrate transmittance following exposure to 10000 Gy dose of gamma-rays and after 40 days of relaxation (a) and change in the visual appearance of the glass substrates after exposure to gamma rays (b).

Indeed, glass transmittance rapidly goes down under exposure to gamma-rays, particularly in the region of 300-600 nm. Ionization generates free electrons and holes that become trapped in vacancies or impurities,<sup>103</sup> thus creating color centers, which significantly reduce the optical transmission of glass. Therefore, all changes in optical

spectra of MAPbBr<sub>3</sub>, CsPbBr<sub>3</sub>, and (to less extent) CsPbI<sub>3</sub> films are associated with the radiation-induced glass substrate darkening.

The third column in Figure 57 shows the PL spectra of the studied systems. PL of MAPbI<sub>3</sub> films is gradually quenched with an increase in the gamma-rays dose, which points to radiative defect formation. These results correlate with the XPS spectra of MAPbI<sub>3</sub>, suggesting a partial material decomposition from the film surface. PL intensity of MAPbBr<sub>3</sub> films drops down after their exposure to 500 Gy and then remains stable after receiving higher doses. Mixed cation Cs<sub>0.15</sub>FA<sub>0.85</sub>PbI<sub>3</sub> and Cs<sub>0.1</sub>MA<sub>0.15</sub>FA<sub>0.75</sub>PbI<sub>3</sub> show even increase in the PL intensity after radiation exposure, which is resembling the behavior of the previously studied mixed halide system undergoing radiation-induced phase segregation. Therefore, we can hypothesize that similar phase segregation effects occur in Cs<sub>0.15</sub>FA<sub>0.85</sub>PbI<sub>3</sub> and Cs<sub>0.1</sub>MA<sub>0.15</sub>FA<sub>0.75</sub>PbI<sub>3</sub> systems leading to the formation of domains with higher phase purity and hence showing enhanced PL quantum yields. This explanation is tentatively supported by increased spatial inhomogeneity of the film emission for these systems after radiation exposure (Figure 60). As for all-inorganic CsPbBr<sub>3</sub> and CsPbI<sub>3</sub> perovskites, both of them showed no noticeable changes in PL spectra after gamma ray exposure, which might suggest superior radiation stability of these materials.

To sum up, the data presented in Figure 57, gamma-ray exposure of pristine perovskite films showed that MAPbI<sub>3</sub> and CsPbBr<sub>3</sub> represent, respectively, the least and the most stable perovskite materials. These findings correlate well with the photostability characteristics reported elsewhere.<sup>35,37</sup> CsPbI<sub>3</sub> showing the best thermal stability was found to decompose from the surface with the formation of metallic lead under high radiation doses. We believe that it is a general feature of all-inorganic perovskites comprising iodide anions. Indeed, we observed virtually the same behavior (Figure 61) for CsPbI<sub>2</sub>Br used as a reference material, which has no problems with the perovskite phase stability under ambient temperatures in contrast to CsPbI<sub>3</sub>, which tends to form orthorhombic yellow phase. Therefore, the revealed degradation pathway should not be associated with the phase transition effects.

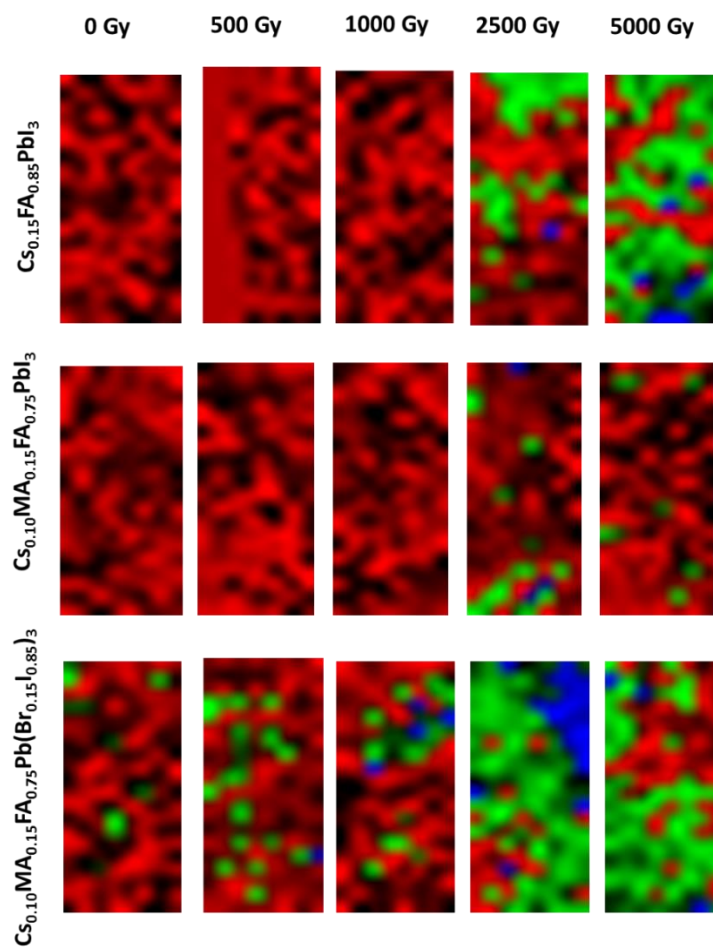


**Figure 60.** PL maps of mixed cation perovskite films showing spatial inhomogeneity of the film emission growing with radiation dose. Color gradient is normalized: red =1, green=0.5, blue=0.

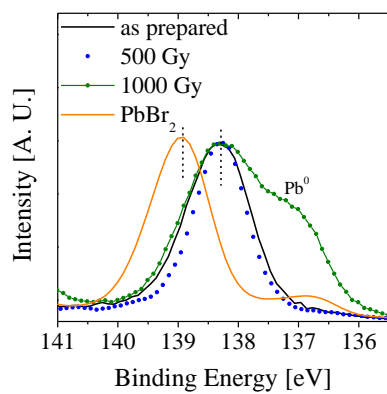


**Figure 61.** Evolution of XPS Pb 4f spectra of CsPbBrI<sub>2</sub>+10%CsBr films under gamma rays.

#### 5.4 Gamma ray stability of perovskite materials in solar cells

At the next stage of the performed study, all perovskite materials were evaluated with respect to radiation hardness in completed solar cells. We have chosen ITO/SnO<sub>2</sub>/PCBA/Perovskite/PTA/MoO<sub>3</sub>/Al solar cell configuration as it showed previously impressive stability.<sup>139,81</sup> The fabricated solar cells were placed inside a metal tube with a fixed <sup>137</sup>Cs ionization source (E = 662 keV) with a dose rate of 2.5 Gy/min. After accumulating a certain dose (100-10000 Gy), we measured JV characteristics and EQE spectra under light bias. More detailed information about solar cell fabrication and characterization procedures can be found in Materials and Methods, Chapter 4.3.

As was mentioned before, gamma rays significantly reduce glass transmittance thus leading to a decrease in the number of photons penetrating to the perovskite active layer and the associated current losses in a solar cell. To model this effect quantitatively, we introduce a correction coefficient  $k_x$  (which is a function of wavelength) showing a change of glass transmittance after exposure to the gamma ray dose  $x$ :

$$k_x(\lambda) = \frac{T_x(\lambda)}{T_0(\lambda)}, \quad (eq. 2)$$

where  $T_0$  and  $T_x$  correspond to transmittance values for non-exposed and exposed substrate, respectively.

This coefficient is used further to calculate the EQE of solar cells assuming that glass darkening is the only radiation-induced degradation effect:

$$EQE_{cal}(\lambda) = EQE_{(0\ kRad)}(\lambda) \cdot k_x(\lambda). \quad (eq. 3)$$

Figure 62 shows the evolution of EQE values for PSCs based on six different perovskite absorbers after exposure to 10000 Gy dose of gamma-rays. Here, solid lines show the experimental spectra measured under light bias, while the dashed red lines represent calculated  $EQE_{cal}$  according to the equation (3). The gap between the calculated and measured EQE values clearly shows the impact of gamma-rays on the intrinsic device performance, i.e. not affected by the substrate behavior. We introduce here an additional parameter  $T$  (which might be considered as a radiation tolerance

factor) calculated following the equation 4, that physically means the ratio between experimentally obtained photocurrent (integration of  $EQE_{exp}$ ) and the photocurrent expected to assume that device behavior is affected only by glass darkening (integration of  $EQE_{cal}$ ):

$$T = \frac{J_{sc}(\text{integrated exp})}{J_{sc}(\text{integrated cal})} . \quad (eq. 4)$$

Figure 62 shows that the lowest T-factor is obtained for the solar cells based on the multication formulation  $Cs_{0.1}MA_{0.15}FA_{0.75}PbI_3$ : these devices deliver only 81% of the maximal achievable current density.

This suggests that this system undergoes degradation under gamma-ray exposure, which leads to the decay of the photocurrent by 19% likely due to the recombination of charge carriers in the radiation-induced trap defects. All-inorganic perovskites  $CsPbI_3$  and  $CsPbBr_3$  showed rather a high photocurrent stability, delivering 96 and 98% from the maximal calculated photocurrent values. These results were expected, as inorganic perovskites were known to be very robust materials with respect to thermal stress and solar light exposure.  $MAPbBr_3$  has a T-factor of 0.95, which implies a 5% reduction in the  $J_{SC}$  due to the radiation damage of the device stack (besides substrate darkening).

Surprisingly,  $MAPbI_3$  demonstrated the highest stability under gamma-ray exposure making a particular impressive  $T=1$ , which means that gamma-ray exposure does not lead to any degradation effects limiting the photocurrent besides the glass substrate darkening.

To analyze the changes in the device power conversion efficiency, we used the following formula:

$$PCE_{cal} = \frac{J_{sc}(cal) \cdot Voc_{(0 \text{ kRad})} \cdot FF_{(0 \text{ kRad})}}{P_{light}} * 100\% . \quad (eq. 5)$$

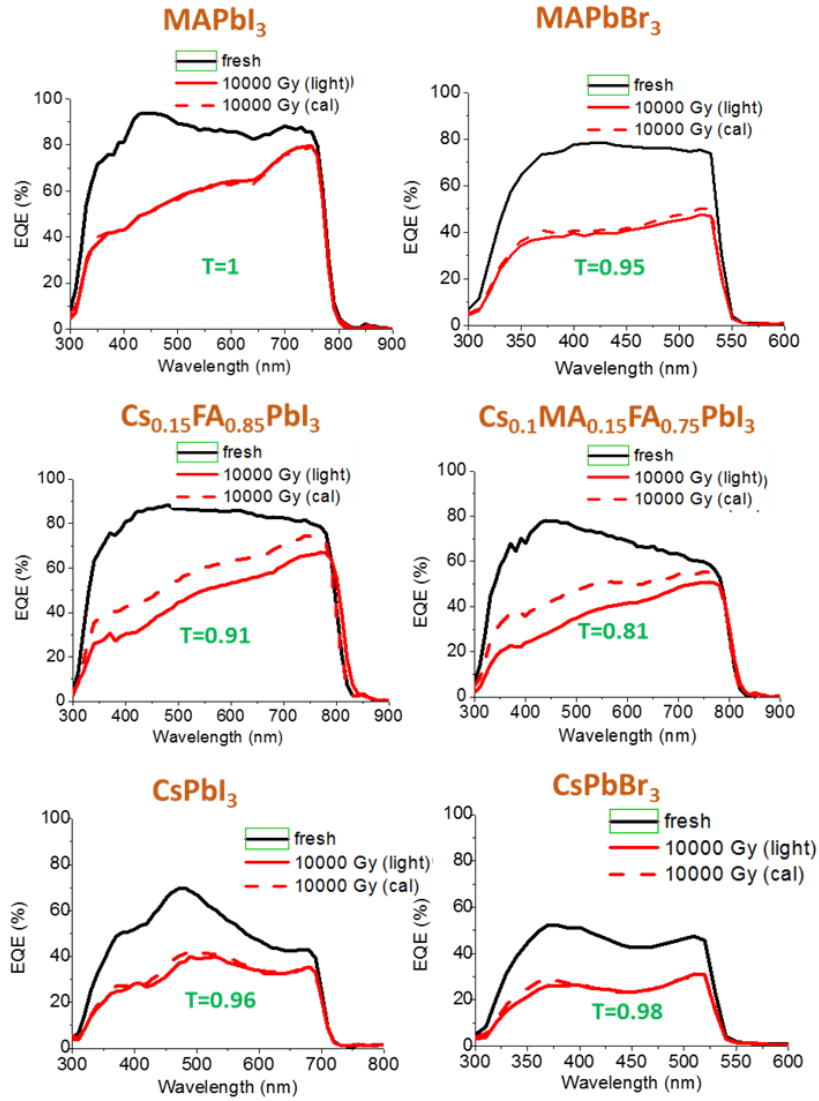
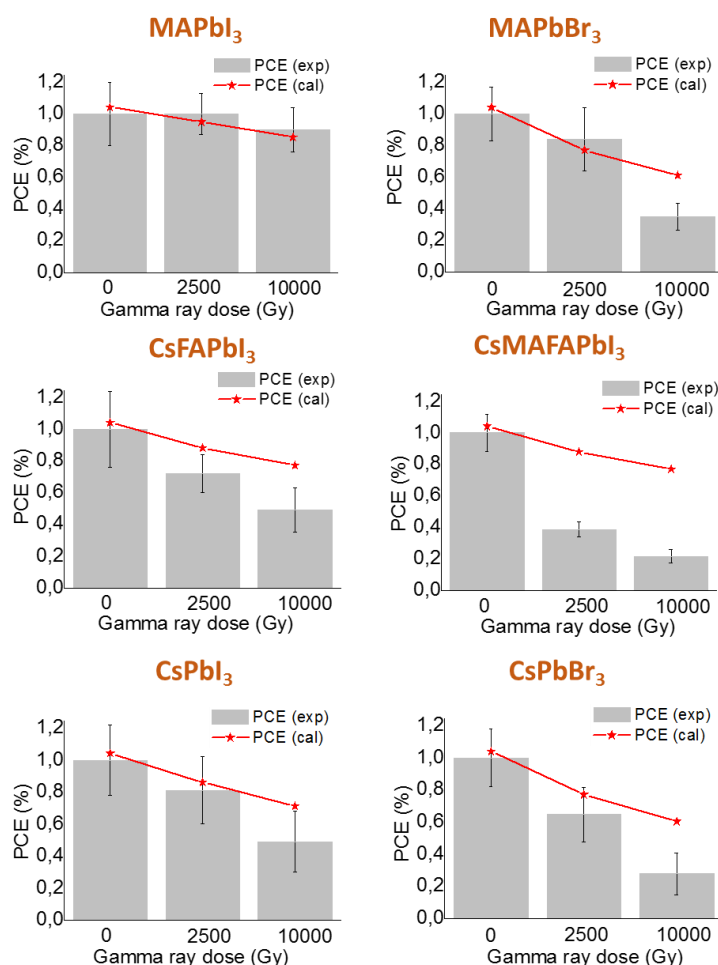


**Figure 62.** Evolution of EQE spectra of the devices after 10000 Gy gamma ray exposure. Calculated EQE spectra were modeled according to equation (3) and show the expected device behavior assuming that photocurrent is affected only by the glass darkening effect. T-factor shows which fraction of the expected  $J_{SC(cal)}$  is actually delivered by the device.

Assuming that gamma-rays induced only glass darkening effects, the device  $V_{OC}$  and FF are supposed to be unaffected, therefore we can take initial values measured before the radiation exposure. The  $J_{SC(cal)}$  is estimated by the integration of the modeled  $EQE_{(cal)}$  over the true AM1.5G spectrum. Therefore,  $PCE_{cal}$  represents the ultimate value of the device power conversion efficiency, which can be expected assuming that

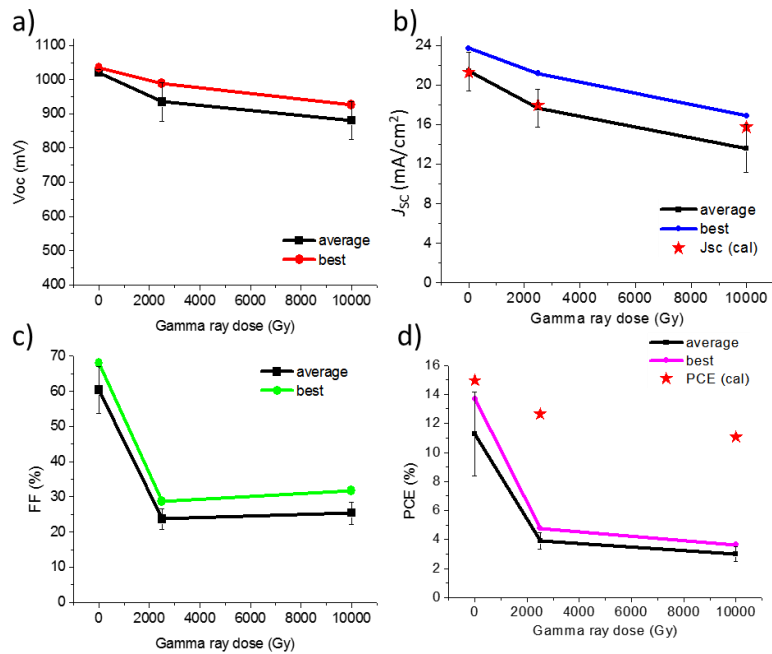
gamma-rays do not affect anyhow device stack with except for the generation of color centers in the glass substrate.

Figure 63 shows the comparison of the experimentally measured PCE values with the theoretically expected PCE<sub>cal</sub>. Solar cells based on Cs<sub>0.1</sub>MA<sub>0.15</sub>FA<sub>0.75</sub>PbI<sub>3</sub> degrade dramatically under the gamma-ray exposure mainly due to the intrinsic radiation-induced processes rather than because of the decreased substrate transparency.



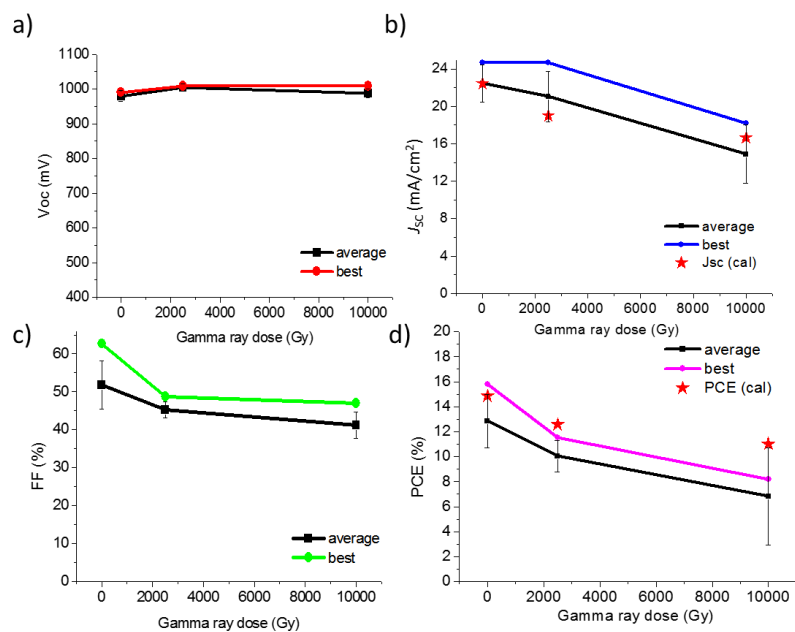
**Figure 63.** Evolution of PCE under gamma ray exposure.

In particular, significantly decreased  $V_{OC}$  and FF support the conclusion about the formation of traps and the massive recombination of charge carriers in the active layer and/or at some functional interface (Figure 64).

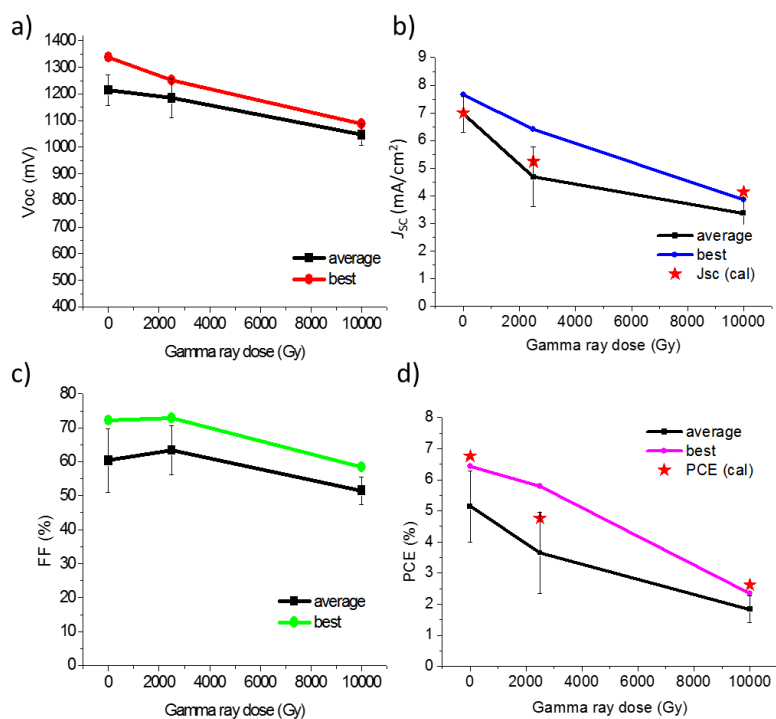


**Figure 64.** Evolution of the characteristics of ITO/SnO<sub>2</sub>/PCBA/Cs<sub>0.1</sub>MA<sub>0.15</sub>FA<sub>0.75</sub>PbI<sub>3</sub>/PTA/MoO<sub>3</sub>/Al solar cells under gamma ray exposure.

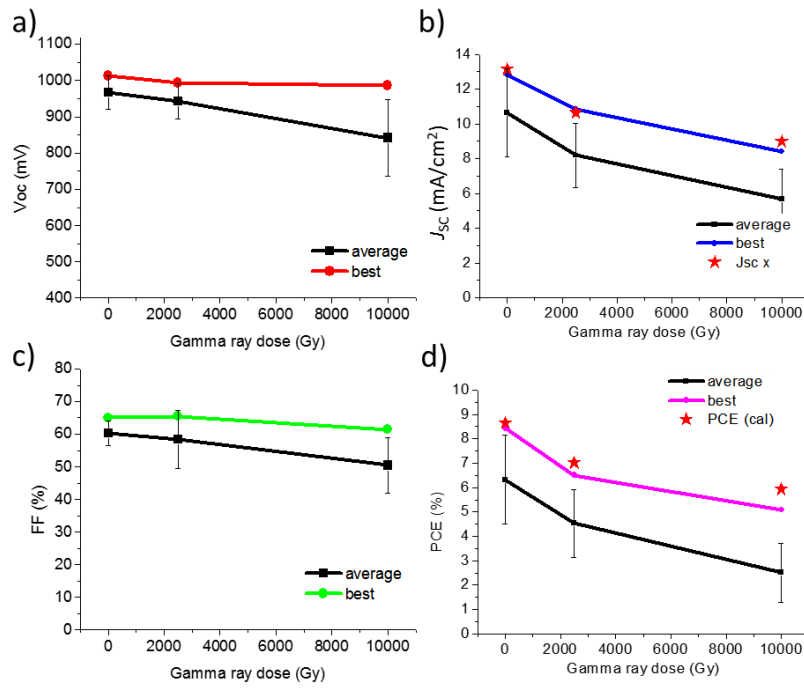
The solar cells based on Cs<sub>0.15</sub>FA<sub>0.85</sub>PbI<sub>3</sub>, MAPbBr<sub>3</sub>, CsPbI<sub>3</sub>, and CsPbBr<sub>3</sub> show somewhat enhanced radiation stability, though their efficiency is dropping significantly after exposure to 10000 Gy dose also due to decay of FF, J<sub>sc</sub>, and V<sub>oc</sub> in some cases (Figure 65, Figure 66, Figure 67, Figure 68).



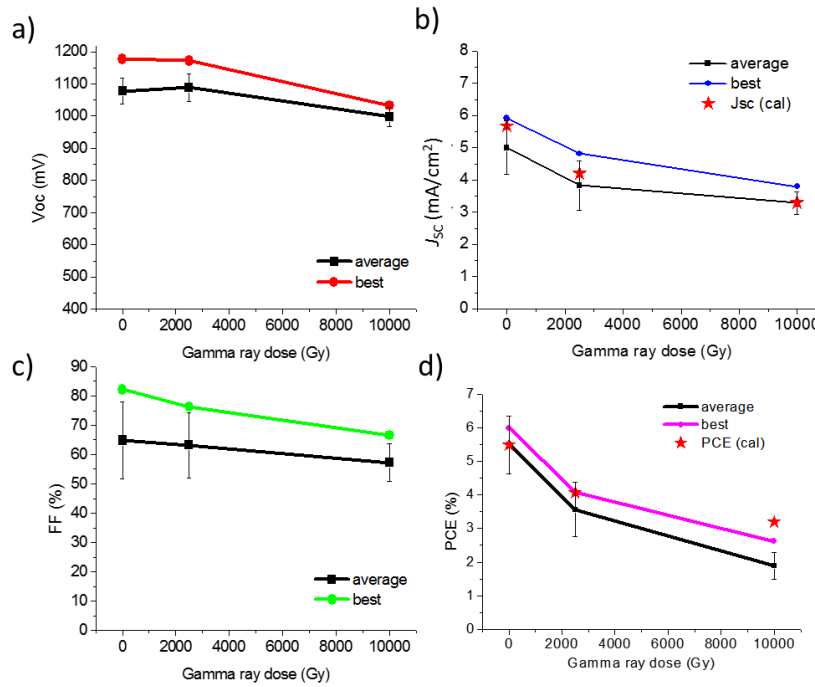
**Figure 65.** Evolution of the characteristics of ITO/SnO<sub>2</sub>/PCBA/Cs<sub>0.15</sub>FA<sub>0.85</sub>PbI<sub>3</sub>/PTA/MoO<sub>3</sub>/Al solar cells under gamma ray exposure.



**Figure 66.** Evolution of the characteristics of ITO/SnO<sub>2</sub>/PCBA/MAPbBr<sub>3</sub>/PTA/MoO<sub>3</sub>/Al solar cells under gamma ray exposure.

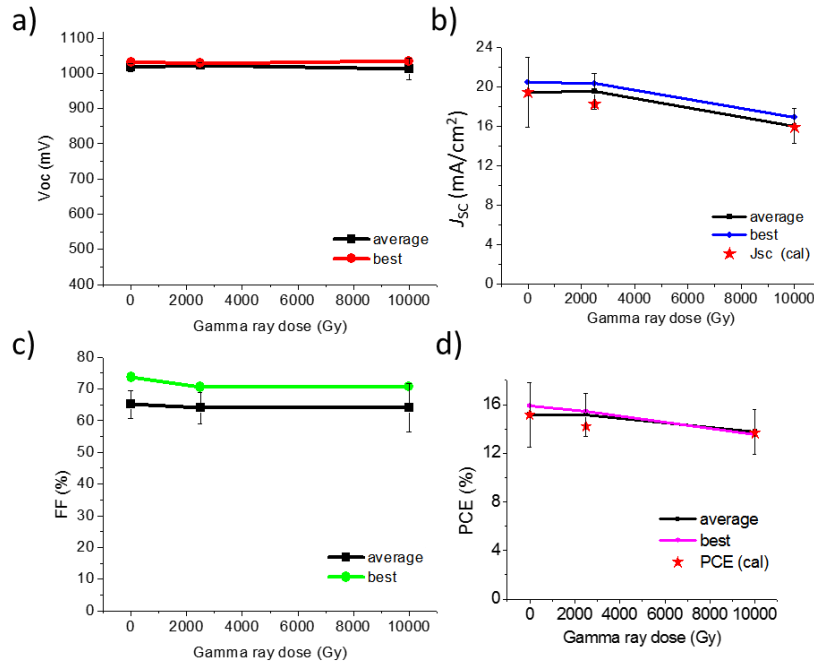


**Figure 67.** Evolution of the characteristics of ITO/SnO<sub>2</sub>/CsPbI<sub>3</sub>/PTA/MoO<sub>3</sub>/Al solar cells under gamma ray exposure.



**Figure 68.** Evolution of the characteristics of ITO/SnO<sub>2</sub>/CsPbBr<sub>3</sub>/PTA/MoO<sub>3</sub>/Al solar cells under gamma ray exposure.

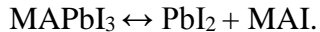
The solar cells based on MAPbI<sub>3</sub> showed a remarkable radiation hardness: both V<sub>OC</sub> and FF do not change after exposure of the devices to 10000 Gy dose of gamma-rays (Figure 69). The only process affecting the solar cell performance, in this case, is color defect formation in glass substrates, which can be easily mitigated e.g. by using quartz substrates. This result is unexpected since MAPbI<sub>3</sub> is known to have very low thermal and photochemical stability.



**Figure 69.** Evolution of the characteristics of ITO/SnO<sub>2</sub>/PCBA/MAPbI<sub>3</sub>/PTA/MoO<sub>3</sub>/Al solar cells under gamma ray exposure.

We theoretically explain this phenomenon by first noting that despite MAPbI<sub>3</sub> having a very high concentration of charge-neutral Schottky vacancy defects the carrier diffusion length remains long and the photovoltaic efficiency high. Theoretically, this has been thoroughly investigated<sup>140,141</sup> and it has been concluded that the main reason for this is that the most stable defect types do not introduce deep traps into the bandgap. The material is classified as self-compensating and the energy of formation for the Schottky defect is surprisingly low especially when compared with other semiconductors. The concentration of the  $nil \rightarrow V'_{MA} + V^*_I + MAI$  in particular is estimated to be about  $2 \cdot 10^{20} \text{ cm}^{-3}$ .<sup>142</sup>

Due to the heavy elements present, hybrid halide perovskites have a high efficiency of gamma ray to free charge carrier conversion.<sup>140</sup> Thus, band edge carriers will become more dominant and the formation of native defects will be more strongly coupled to them. In the case of MAPbI<sub>3</sub>, this leads to either the possibility that charge band edge carriers will dominate ( $\Delta H(V_{MA}^-) = \Delta H_1$ ), the band edge holes will dominate ( $\Delta H(V_I^+) = \Delta H_2$ ) or that both band edges holes and carriers will dominate ( $\Delta H_1 = \Delta H_2$ ).<sup>143</sup> Since our experiment shows that the material becomes I-poor on the surface but remains I-rich in the bulk phase we can conclude that on the surface the band edge carriers will dominate under gamma irradiation. Once MAI diffuses out of the perovskite it is predominantly converted (Figure 70, Table 4) into CH<sub>3</sub>I and NH<sub>3</sub> gasses through a substantial barrier ( $\Delta G(298K) = 2.49$  eV); however, this barrier is lower than the energy required for the endothermic degradation of MAI to CH<sub>3</sub>NH<sub>2</sub> + HI ( $\Delta G(298K) = 4.10$  eV), these latter products are in fact not observed in large quantities in previous studies.<sup>33</sup> Since the carbon-iodine bond is the weakest, it will be the first to be cleaved by ionizing radiation. Our calculations indicated that the free energy of forming a CH<sub>3</sub>\*+I\* is comparable to the barrier of gas formation:  $\Delta G(298) = 2.26$  eV, this process is highly entropic and becomes significantly more favorable as temperature increases. The iodine can then favorably react with the ammonia and rejoin with the methyl radical to recover MAI, this material then returns to the equilibrium and pushes the reaction leftwards which in turn accomplishes self-healing:



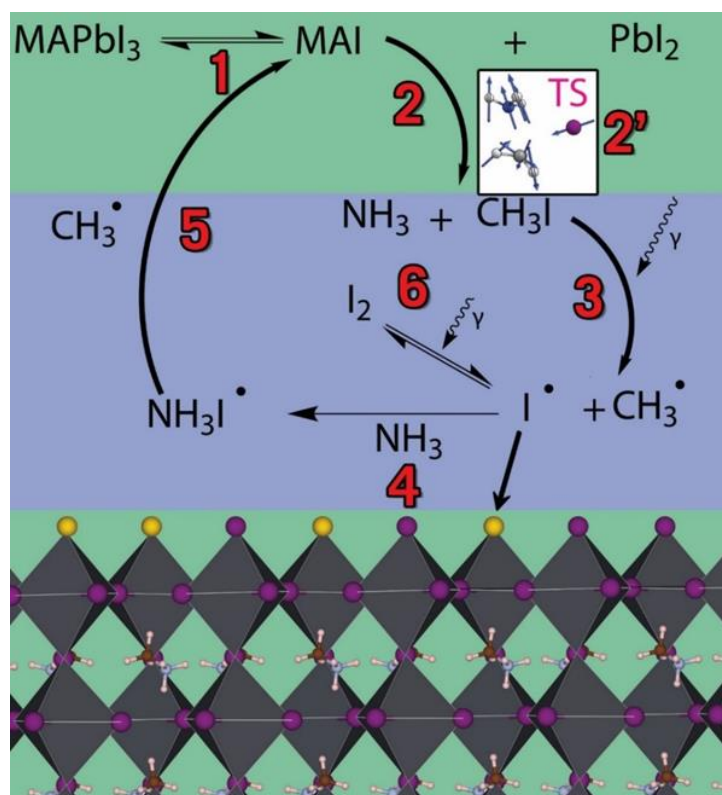


**Figure 70.** A diagram showing mechanisms of MAPbI<sub>3</sub> decomposition based on theoretical calculations. A green background indicates a solid-state while a blue background indicates the gas phase. The reactions are all numbered and their Gibbs free energy of reaction can be referenced in Table 6.

**Table 4.** The reactions pertaining to Figure 70.

#	Reactions	H(eV)	G <sub>298</sub> (eV)	S(eV/K)
1	MAPbI <sub>3</sub> → MAI + PbI <sub>2</sub> ( <i>Solid State</i> )	-0.02	-	-
2	MAI → CH <sub>3</sub> I + NH <sub>3</sub> ( <i>Solid State</i> )	1.02	-	-
2	MAI → CH <sub>3</sub> I + NH <sub>3</sub> ( <i>Gas Phase</i> )	0.15	-0.29	1.49E-03
2'	MAI → MAI(TS) [ <i>Barrier</i> ]	2.51	2.49	8.67E-05
3	CH <sub>3</sub> I → CH <sub>3</sub> * + I*	2.63	2.26	1.26E-03
4	NH <sub>3</sub> + I* → NH <sub>3</sub> I*	-0.43	-0.16	-9.06E-04
5	NH <sub>3</sub> I* + CH <sub>3</sub> * → MAI	-2.35	-1.80	-1.85E-03
6	I <sub>2</sub> → I* + I*	1.90	1.63	9.32E-04

An explanation for why damage becomes limited to the surface is that the radical iodine collides with the perovskite's surface, which due to being charge-carrier dominated will donate a charge and become passivated by the radical iodines. This is essentially the gas-phase equivalent of the acidic passivation of a perovskite. It's notable that this latter explanation really does depend on the formation of radicals since acid-base chemistry is normally not favorable in the gas phase due to a lack of solvation. Even if we were to assume the alternative degradation of MAI to HI +CH<sub>3</sub>NH<sub>2</sub> were to become dominant it would not introduce a Lewis acid to the surface the way that radical ionization of MAI does. We plan to study this charge-transfer passivation in the future.

The transition state (activation energy) includes imaginary mode displacement vectors, these confirm the character corresponds to the formation of NH<sub>3</sub> + CH<sub>3</sub>I. The surface displayed is iodine poor corresponding to the removal of MAI and is predicted to be band-edge carrier dominant. The vacancies are displayed as yellow balls (Figure 70). Thus, we strongly believe that the low thermodynamic stability of MAPbI<sub>3</sub> is, in a way, responsible for the fast healing of material while under irradiation by gamma rays. Indeed, it is experimentally known that MAPbI<sub>3</sub> can easily dissociate to the volatile species CH<sub>3</sub>I, NH<sub>3</sub>, and the PbI<sub>2</sub> phase and then reform back from these species.<sup>43,33</sup>

Therefore, in the case of MAPbI<sub>3</sub>, the reversible formation of the volatiles, combined with the radical chemistry induced by ionizing radiation, their easy diffusion in the active layer and the passivating effects of iodine as a Lewis acid can be considered the fundamental mechanisms of fast defect healing. None of the other perovskite materials actually form significant concentrations of volatile species at low temperatures, thus the gas-phase healing cannot happen in these materials (Scheme 2). For instance, MAPbBr<sub>3</sub> decomposition produced PbBr<sub>2</sub> and MABr. Though they can react back and reform the perovskite phase, the diffusion ability of these components is very limited since they are both stable solid phases.

Relaxation effects in the perovskite solar cells were studied after 40 days of storage (room temperature, inert atmosphere) following their exposure to 10000 Gy of gamma-rays. First, we observed that color defects in the exposed pristine glass

substrates were partially healed and their transmittance was noticeably recovered (Figure 59). Following the approach discussed above and using the equations (2) and (3), we modeled the EQE spectra of each system with respect to the actual glass transmittance after the relaxation.

Figure 71 shows the evolution of the EQE spectra of exposed samples after 40 days of storage and their comparison with the calculated values. One can see a notable recovery effect, which can be both from the healing of color defects in the substrates and radiation-induced defects in the absorber material. In most cases, the T-factors show an increase over the 40 days of storage, which suggests that radiation-induced degradation effects inside the device stack are reversible. We emphasize that actually the recovery of the substrate transmittance might be responsible for the self-healing effects frequently reported in the literature for perovskite solar cells exposed to radiation. Therefore, careful control of the substrate behavior and appropriate reference tests are required for an accurate assessment of the relaxation effects following the radiation exposure of the perovskite solar cells.

#### **5.4 Summary**

To summarize, we performed a comparative study of six different perovskite materials under gamma-radiation doses ranging from 100 to 10000 Gy. Using several complementary techniques we revealed a surface decomposition of  $\text{MAPbI}_3$  and  $\text{CsPbI}_3$  in thin films under gamma ray exposure, while the bulk phase was not really affected. The films of  $\text{MAPbBr}_3$ ,  $\text{Cs}_{0.15}\text{FA}_{0.85}\text{PbI}_3$ ,  $\text{Cs}_{0.1}\text{MA}_{0.15}\text{FA}_{0.75}\text{PbI}_3$ , and  $\text{CsPbBr}_3$  did not show any detectable changes in optical properties (UV-vis), surface (XPS), and phase composition (XRD). The formation of defects leading to PL quenching was revealed for  $\text{MAPbI}_3$  and  $\text{MAPbBr}_3$ . Multication perovskites showed enhanced PL intensities after radiation exposure, which is consistent with their partial phase segregation induced by gamma-rays. All-inorganic perovskites showed no change in PL even after receiving a high dose of 10000 Gy, which suggests that these materials are very robust.

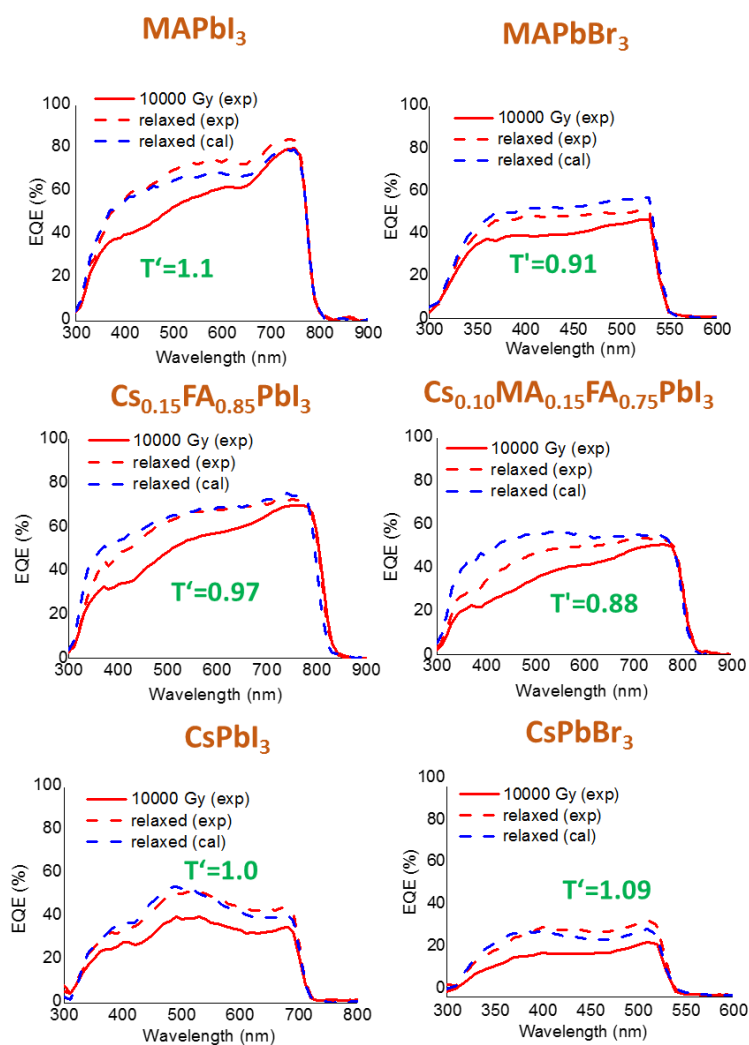


**Figure 71.** Evolution of EQE spectra after 40 days of device storage at room temperature in an inert atmosphere. Calculated EQE values consider glass darkening as the only effect leading to the photocurrent decrease as compared to the non-exposed devices.

The radiation hardness of the completed n-i-p solar cells assembled in ITO/SnO<sub>2</sub>/PCBA/perovskite/MoO<sub>3</sub>/Al configuration was substantially different from the behavior of the perovskite thin films. In particular, the devices based on multication (Cs<sub>0.15</sub>FA<sub>0.85</sub>PbI<sub>3</sub> and Cs<sub>0.1</sub>MA<sub>0.15</sub>FA<sub>0.75</sub>PbI<sub>3</sub>) perovskites showed poor radiation stability. The observed degradation can be attributed to the radiation-induced phase segregation effects. All inorganic PSCs showed minor decay in  $J_{SC}$  and FF, which suggests the formation of deep trap states leading to massive recombination of charge

carriers. MAPbBr<sub>3</sub> solar cells degraded mainly due to V<sub>OC</sub> and FF decay, while photocurrent remained stable under gamma ray exposure. Some recovery of the photovoltaic performance after 40 days of storage was shown to be both due to the defect healing in the glass substrates and perovskite materials.

Surprisingly, the methylammonium-based perovskites MAPbI<sub>3</sub>, known for the low thermal and photochemical stability, demonstrated a remarkable radiation hardness in solar cells. The MAPbI<sub>3</sub>-based devices did not show any degradation effects even after exposure to the impressive dose of 10000 Gy of gamma-rays besides some minor photocurrent decrease exclusively because of the substrate darkening. The observed exciting radiation tolerance of perovskite solar cells with the MAPbI<sub>3</sub> absorber layer was attributed to the unique dynamic behavior of this material capable of reversible decomposition with the formation of volatile species, which can diffuse easily within the perovskite lattice and heal the radiation-induced defects. The presented findings change the paradigm of research in the field focused on the development of perovskite solar cells with enhanced radiation stability for space applications.

## Conclusions

In this thesis, we performed a systematic study of multiple systems involving different perovskite absorbers and charge transport interlayers and explored their behavior under exposure to simulated solar light or ionizing radiation. Starting from individual thin films and going all the way to completed devices we revealed a number of important degradation mechanisms and featured the most promising material combinations potentially suitable for reaching long-term perovskite solar cell operational stability.

A comparative analysis of five organic charge transport layers in two different sample geometries, glass/CTL/MAPbI<sub>3</sub> and glass/MAPbI<sub>3</sub>/CTL, provided complementary information on the interfacial chemistry and encapsulation properties of the corresponding CTL materials. We discovered that rylene diimides NDI and PDI form adducts with PbI<sub>2</sub> which shifts the thermodynamic equilibrium in the system and

accelerates the decomposition of the perovskite films. Spiro-OMeTAD was found to react with  $\text{CH}_3\text{I}$ , which is another perovskite degradation product, most probably *via* the formation of quaternary ammonium salts as revealed by ToF-SIMS analysis. Such interfacial chemistry affects badly the operation lifetime of the devices. Among the studied CTLs, fullerene derivatives ( $\text{PC}_{61}\text{BM}$ ,  $\text{PC}_{71}\text{BM}$ ) delivered the most impressive results as top encapsulating coatings improving the bulk stability of the perovskite films. However, interfacial degradation related to MAI diffusion and accumulation in the fullerene-based ETLs strongly deteriorates their electrical characteristics and ruins the perovskite solar cell performance.

A systematic study of 20 different systems based on combinations of four hole-transport materials ( $\text{NiO}_x$ , PEDOT:PSS, PTAA, and PTA) and five lead halide perovskite formulations ( $\text{MAPbI}_3$ ,  $\text{CsFAPbI}_3$ ,  $\text{CsMAFAPbI}_3$ ,  $\text{CsMAFAPb}(\text{BrI})_3$  and  $\text{CsFAPb}(\text{BrI})_3$ ) provided essential information on the factors governing the stability of HTL/perovskite interfaces under light exposure. It was found that polyarylamines PTA and PTAA represent the most promising HTLs among the studied materials since they do not undergo aggressive heat- and light-induced chemistry with complex lead halides. Interfacial reactions between  $\text{NiO}_x$  and  $\text{MAPbI}_3$  produce  $\text{NiI}_2$  and  $\text{PbO}$ , thus leading to device failure. ToF SIMS analysis revealed that PEDOT:PSS also does not form a stable interface with the perovskite absorber most likely due to the formation of Pb-PSS salts.

We showed that lead halide perovskite formulation can strongly affect both bulk and interfacial degradation pathways realized under sample exposure to light and heat. In particular, multication and mixed halide perovskites tend to undergo light-induced recrystallization leading to the loss of the continuous film structure and appearance of voids and pinholes. Additionally, the formation of non-active  $\beta$ -phase of  $\text{FAPbI}_3$  under light exposure was observed. Such unfavorable phase dynamics are strongly accelerated when the perovskite films are grown atop “aggressive” HTLs, which suggests that film degradation is catalyzed by defects formed at the interfaces. It should be emphasized that light-induced absorber crystallization and halide phase segregation effects were essentially suppressed by depositing the  $\text{PC}_{61}\text{BM}$  ETL layer atop the perovskite films,

which illustrates the importance and synergy of both HTL/perovskite and perovskite/ETL interface engineering. The obtained results and, in particular, device stability studies featured MAPbI<sub>3</sub> as one of the most stable lead halide perovskites showing impressive photostability in thin films (no detectable aging within 4000 h) and completed solar cells (stable for >1000 h).

Exploring the impact of gamma rays on perovskite thin films and solar cells resulted in several important findings. In particular, we observed for the first time halide phase segregation in Cs<sub>0.15</sub>MA<sub>0.10</sub>FA<sub>0.75</sub>Pb(Br<sub>0.17</sub>I<sub>0.83</sub>)<sub>3</sub> perovskite films induced by gamma-ray exposure as evidenced by a set of complementary techniques. Multication perovskite systems such as Cs<sub>0.15</sub>MA<sub>0.10</sub>FA<sub>0.75</sub>PbI<sub>3</sub> and Cs<sub>0.15</sub>FA<sub>0.85</sub>PbI<sub>3</sub> also showed some clear signatures of phase segregation promoted by gamma rays. While analyzing the radiation stability of PSCs, we found that devices based on all-inorganic absorbers such as CsPbI<sub>3</sub> and CsPbBr<sub>3</sub> are quite promising since they show just a minor efficiency roll-off after exposure to 10000 Gy of gamma-rays. The lowest radiation stability was observed for devices with multication perovskite formulations: a significant decrease in  $J_{SC}$  and FF suggests the formation of deep trap states leading to massive recombination of charge carriers. Among all studied PSCs, the devices incorporating the MAPbI<sub>3</sub> absorber layer demonstrated a remarkable radiation hardness. No degradation effects were observed even after exposure of the MAPbI<sub>3</sub>-based solar cells to the impressive radiation dose of 10000 Gy, which is 10 times higher compared to the total average ionization dose received by satellite within 25 years of exploitation on Low equatorial orbit. Notably, the observed excellent radiation hardness of MAPbI<sub>3</sub> devices also correlates with the superior photostability of PSCs based on this absorber material. Such unexpected results were attributed to the unique dynamic behavior of this material capable of reversible decomposition with the formation of volatile species, which can diffuse easily within the perovskite lattice and heal the radiation-induced defects.

The research findings of this thesis point also to new challenges to be addressed in future projects. One of them is to develop stable ETL materials for p-i-n perovskite solar cells. A possible solution emerging in the literature is based on combining

fullerene-based materials in composites with some inert polymeric fillers, e.g. poly(methyl methacrylate,<sup>144</sup> capable of blocking MAI diffusion, which is an Achilles heel of the current generation of PC<sub>61</sub>BM-type ETLs. Alternatively, the introduction of additional diffusion barriers such as Al<sub>2</sub>O<sub>3</sub><sup>124</sup> at perovskite/PC<sub>61</sub>BM interface is actively explored to block MAI migration. Another important concern is related to color defect formation in substrates exposed to high gamma ray doses. To address this issue one should replace conventional glass with alternative substrate materials, e.g. quartz<sup>101</sup> or flexible PET,<sup>145</sup> which are more resistant to ionizing radiation.

Finally, it is worthy to mention that perovskite photovoltaics is still a hot topic in science and continues to pose challenges to researchers from all over the world. We believe that this work makes a valuable contribution to this field and represents one of the important steps on the way to perovskite PV technology commercialization.

## Bibliography

- (1) BP Energy Outlook 2019 <https://www.bp.com/content/dam/bp/business-sites/en/global/corporate/pdfs/energy-economics/energy-outlook/bp-energy-outlook-2019.pdf>
- (2) 2020 Monthly Solar Photovoltaic Module Shipments Report. *Energy Inf. Adm.* **2020**, June [https://www.eia.gov/renewable/monthly/solar\\_photo/pdf/renewable.pdf](https://www.eia.gov/renewable/monthly/solar_photo/pdf/renewable.pdf)
- (3) NREL Efficiency Chart <https://www.nrel.gov/pv/cell-efficiency.html>
- (4) Masuko, K.; Shigematsu, M.; Hashiguchi, T.; Fujishima, D.; Kai, M.; Yoshimura, N.; Yamaguchi, T.; Ichihashi, Y.; Mishima, T. . M. N. .; Yamanishi, T.; Takahama, T.; Taguchi, M.; Maruyama, E.; Okamoto, S. Achievement of More Than 25 % Conversion Heterojunction Solar Cell. *IEEE J. Photovoltaics* **2014**, *4* (6), 1433–1435. DOI: 10.1109/JPHOTOV.2014.2352151
- (5) Yoshikawa, K.; Kawasaki, H.; Yoshida, W.; Irie, T.; Konishi, K.; Nakano, K.; Uto, T.; Adachi, D.; Kanematsu, M.; Uzu, H.; et al. Silicon Heterojunction Solar Cell with Interdigitated Back Contacts for a Photoconversion Efficiency over 26%. *Nat. Energy* **2017**, *2*, 17032. <https://doi.org/10.1038/nenergy.2017.32>
- (6) Green, M. A.; Ho-baillie, A.; Snaith, H. J. The Emergence of Perovskite Solar Cells. *Nat. photonics* **2014**, *8*, 506–514. <https://doi.org/10.1038/nphoton.2014.134>
- (7) Knop, O.; Wasylishen, R. E.; White, M. A.; Stanley, T.; Michiel, J. M.; Stanley, T. Alkylammonium Lead Halides. Part 2. CH<sub>3</sub>NH<sub>3</sub>PbX<sub>3</sub> (X = Cl, Br, I) Perovskites: Cuboctahedral Halide Cages with Isotropic Cation Reorientation. *Can. J. Chem.* **1990**, *68*, 412–422.
- (8) Kieslich, G.; Sun, S.; Cheetham, A. K. Chemical Science Solid-State Principles Applied to Organic – Inorganic Perovskites : New Tricks for an Old Dog. *Chem. Sci.* **2014**, *5*, 4712–4715. <https://doi.org/10.1039/C4SC02211D>
- (9) Lufaso, M. W.; Woodward, P. M. Prediction of the Crystal Structures of Perovskites Using the Software Program SPuDS. *Acta Cryst.* **2001**, *B57*, 725–738. DOI: 10.1107/S0108768101015282
- (10) Goodenough, J. Electronic and Ionic Transport Properties and Other Physical Aspects of Perovskites. *Rep. Prog. Phys.* **2004**, *67*, 1915–1993. <https://doi.org/10.1088/0034-4885/67/11/R01>
- (11) Zeng, Q.; Zhang, X.; Liu, C.; Feng, T.; Chen, Z.; Zhang, W.; Zheng, W.; Zhang, H.; Yang, B. Inorganic CsPbI<sub>2</sub>Br Perovskite Solar Cells: The Progress and Perspective . *Sol. RRL* **2019**, *3* (1), 1800239. <https://doi.org/10.1002/solr.201800239>
- (12) Li, Z.; Yang, M.; Park, J. S.; Wei, S. H.; Berry, J. J.; Zhu, K. Stabilizing Perovskite Structures by Tuning Tolerance Factor: Formation of Formamidinium and Cesium Lead Iodide Solid-State Alloys. *Chem. Mater.* **2016**, *28* (1), 284–292. <https://doi.org/10.1021/acs.chemmater.5b04107>
- (13) Kojima A., Teshima K., M. T. and S. Y. Novel Photoelectrochemical Cell with Mesoscopic Electrodes Sensitized by Lead-Halide Compounds. In *Proc. 210th ECS Meeting (ECS, 2006)*; **2006**. DOI:10.1149/ma2007-02/8/352
- (14) Kojima, A.; Teshima, K.; Shirai, Y.; Miyasaka, T. Organometal Halide Perovskites as Visible-Light Sensitizers for Photovoltaic Cells. *J. Am. Chem. Soc.* **2009**, *131* (17), 6050–6051.

- <https://doi.org/10.1021/ja809598r>
- (15) Im, J.; Lee, C.; Lee, J.; Park, S.; Park, N. 6.5% Efficient Perovskite Quantum-Dot-Sensitized Solar Cell. *Nanoscale* **2011**, 2, 4088–4093. <https://doi.org/10.1039/c1nr10867k>.
- (16) Lee, M. M.; Teuscher, J.; Miyasaka, T.; Murakami, T. N.; Snaith, H. J. Efficient Hybrid Solar Cells Based on Meso-Superstructured Organometal Halide Perovskites. *Science (80-. )*. **2012**, 338, 643–648. DOI: 10.1126/science.1228604
- (17) Heo, J. H.; Im, S. H.; Noh, J. H.; Mandal, T. N.; Lim, C.; Chang, J. A.; Lee, Y. H.; Kim, H.; Sarkar, A.; Nazeeruddin, K.; et al. Efficient Inorganic–Organic Hybrid Heterojunction Solar Cells Containing Perovskite Compound and Polymeric Hole Conductors. *Nat.photonics* **2013**, 7, 1–6. <https://doi.org/10.1038/NPHOTON.2013.80>
- (18) Liu, M.; Johnston, M. B.; Snaith, H. J. Efficient Planar Heterojunction Perovskite Solar Cells by Vapour Deposition. *Nature* **2013**, 501 (7467), 395–398. <https://doi.org/10.1038/nature12509>
- (19) Coontz, R. Science’s Top 10 Breakthroughs of 2013. *Science* **2013**, 1–4. <https://www.sciencemag.org/news/2013/12/sciences-top-10-breakthroughs-2013>
- (20) Saliba, M.; Matsui, T.; Seo, J. Y.; Domanski, K.; Correa-Baena, J. P.; Nazeeruddin, M. K.; Zakeeruddin, S. M.; Tress, W.; Abate, A.; Hagfeldt, A.; et al. Cesium-Containing Triple Cation Perovskite Solar Cells: Improved Stability, Reproducibility and High Efficiency. *Energy Environ. Sci.* **2016**, 9 (6), 1989–1997. <https://doi.org/10.1039/c5ee03874j>
- (21) Meng, L.; You, J. Addressing the Stability Issue of Perovskite Solar Cells for Commercial Applications. *Nat. Commun.* **2018**, 9, 5265. <https://doi.org/10.1038/s41467-018-07255->
- (22) NREL. Solar Manufacturing Cost Analysis. <https://www.nrel.gov/analysis/solar-manufacturing-cost.html>
- (23) Grancini, G.; Zimmermann, I. One-Year Stable Perovskite Solar Cells by 2D / 3D Interface Engineering. *Nat. Commun.* **2017**, 8, 15684. <https://doi.org/10.1038/ncomms15684>
- (24) Arora, N.; Dar, M. I.; Hinderhofer, A.; Pellet, N.; Yadav, P.; Schreiber, F.; Zakeeruddin, S. M.; Grätzel, M. CuSCN Hole Extraction Layer Based Perovskite Solar Cells Yield Stabilized Efficiency Exceeding 20%. *Science (80-. )*. **2017**, 358, 768–771. <https://science.sciencemag.org/content/358/6364/768>
- (25) Hou, Y.; Hou, Y.; Du, X.; Scheiner, S.; Mcmeekin, D. P.; Wang, Z.; Li, N.; Killian, M. S.; Chen, H.; Richter, M.; et al. A Generic Interface to Reduce the Efficiency-Stability-Cost Gap of Perovskite Solar Cells. *Science (80-. )*. **2017**, 358 (6367), 1192–1197. <https://doi.org/10.1126/science.aao5561>
- (26) Leguy, A.; Hu, Y.; Campoy-quiles, M.; Alonso, M. I.; Weber, O. J.; Azarhoosh, P.; Schilfgaarde, M. Van; Weller, M. T.; Bein, T.; Nelson, J.; et al. The Reversible Hydration of CH<sub>3</sub>NH<sub>3</sub>PbI<sub>3</sub> in Films , Single Crystals and Solar Cells. *Chem. Mater.* **2015**, 27, 3397–3407. <https://doi.org/10.1021/acs.chemmater.5b00660>
- (27) Wang, Z.; Shi, Z.; Li, T.; Chen, Y.; Huang, W. Stability of Perovskite Solar Cells : A Prospective on the Substitution of the A Cation and X Anion Angewandte. *Angew.Chem.Int* **2016**, 56, 1190–1212. <https://doi.org/10.1002/anie.201603694>
- (28) Song, Z.; Abate, A.; Wathage, S. C.; Liyanage, G. K.; Phillips, A. B.; Steiner, U.; Graetzel, M.; Heben, M. J. Perovskite Solar Cell Stability in Humid Air : Partially Reversible Phase Transitions in the PbI<sub>2</sub> - CH<sub>3</sub>NH<sub>3</sub>I-H<sub>2</sub>O System. *Adv. Energy Mater.* **2016**, 6, 1600846. <https://doi.org/10.1002/aenm.201600846>

- (29) Yang, J.; Siempelkamp, B. D.; Liu, D.; Kelly, T. L. Investigation of CH<sub>3</sub>NH<sub>3</sub>PbI<sub>3</sub> Degradation Rates and Mechanisms in Controlled Humidity Environments Using in Situ Techniques. *ACS Nano* **2015**, *2*, 1955–1963. <https://doi.org/10.1021/nn506864k>
- (30) Christians, J. A.; Alexander, P.; Herrera, M.; Kamat, P. V. Transformation of the Excited State and Photovoltaic Efficiency of CH<sub>3</sub>NH<sub>3</sub>PbI<sub>3</sub> Perovskite upon Controlled Exposure to Humidified Air Transformation of the Excited State and Photovoltaic Efficiency of CH<sub>3</sub>NH<sub>3</sub>PbI<sub>3</sub> Perovskite upon Controlled Exposure to H. *J. Am. Chem. Soc.* **2015**, *137*, 1530. <https://doi.org/10.1021/ja511132>
- (31) Bryant, D.; Aristidou, N.; Pont, S.; Sanchez-Molina, I.; Chotchunangatchaval, T.; Wheeler, S.; Durrant, J. R.; Haque, S. A. Light and Oxygen Induced Degradation Limits the Operational Stability of Methylammonium Lead Triiodide Perovskite Solar Cells. *Energy Environ. Sci.* **2016**, *9* (5), 1655–1660. <https://doi.org/10.1039/c6ee00409a>
- (32) Pearson, A. J.; Eperon, G. E.; Hopkinson, P. E.; Habisreutinger, S. N.; Wang, J. T.; Snaith, H. J.; Greenham, N. C. Oxygen Degradation in Mesoporous Al<sub>2</sub>O<sub>3</sub> / CH<sub>3</sub>NH<sub>3</sub>PbI<sub>3</sub>(3 - x)Cl<sub>x</sub> Perovskite Solar Cells : Kinetics and Mechanisms. *Adv. Energy Mater.* **2016**, *6* (13), 1600014. <https://doi.org/10.1002/aenm.201600014>
- (33) Juarez-Perez, E. J.; Hawash, Z.; Raga, S. R.; Ono, L. K.; Qi, Y. Thermal Degradation of CH<sub>3</sub>NH<sub>3</sub>PbI<sub>3</sub> Perovskite into NH<sub>3</sub> and CH<sub>3</sub>I Gases Observed by Coupled Thermogravimetry-Mass Spectrometry Analysis. *Energy Environ. Sci.* **2016**, *9* (11), 3406–3410. <https://doi.org/10.1039/c6ee02016j>
- (34) Misra, R. K.; Aharon, S.; Li, B.; Mogilyansky, D.; Visoly-Fisher, I.; Etgar, L.; Katz, E. A. Temperature- and Component-Dependent Degradation of Perovskite Photovoltaic Materials under Concentrated Sunlight. *J. Phys. Chem. Lett.* **2015**, *6* (3), 326–330. <https://doi.org/10.1021/jz502642b>
- (35) Akbulatov, A. F.; Luchkin, S. Y.; Frolova, L. A.; Dremova, N. N.; Zhidkov, I. S.; Gerasimov, K. L.; Anokhin, D. V.; Kurmaev, E. Z.; Stevenson, K. J.; Troshin, P. A. Probing the Intrinsic Thermal and Photochemical Stability of Hybrid and Inorganic Lead Halide Perovskites. *J. Phys. Chem. Lett.* **2017**, *8*, 1211–1218. <https://doi.org/10.1021/acs.jpcclett.6b03026>
- (36) Emilio J. Juarez-Perez, Luis K. Ono, Maki Maeda, Yan Jiang, Zafer Hawash, Y. Q. Photo-, Thermal- Decomposition in Methylammonium Halide Lead Perovskites and Inferred Design Principles to Increase Photovoltaic Device Stability. *J. Mater. Chem. A* **2018**, *6*, 9604–9612. <https://doi.org/10.1039/C8TA03501F>
- (37) Boldyreva, A. G.; Akbulatov, A. F.; Elnaggar, M.; Luchkin, S. Y.; Danilov, A. V.; Zhidkov, I. S.; Yamilova, O. R.; Fedotov, Y. S.; Bredikhin, S. I.; Kurmaev, E. Z.; et al. Impact of Charge Transport Layers on the Photochemical Stability of MAPbI<sub>3</sub> in Thin Films and Perovskite Solar Cells. *Sustain. Energy Fuels* **2019**, *3*, 2705–2716. <https://doi.org/10.1039/c9se00493a>
- (38) Leijtens, T.; Eperon, G. E.; Noel, N. K.; Habisreutinger, S. N.; Petrozza, A.; Snaith, H. J. Stability of Metal Halide Perovskite Solar Cells. *Adv. Energy Mater.* **2015**, *5*, 1500963. <https://doi.org/10.1002/aenm.201500963>
- (39) Ouyang, Y.; Li, Y.; Zhu, P.; Li, Q.; Gao, Y.; Tong, J.; Shi, L.; Zhou, Q.; Ling, C.; Chen, Q.; et al. Photo-Oxidative Degradation of Methylammonium Lead Iodide Perovskite: Mechanism and Protection. *J. Mater. Chem. A* **2019**, *7* (5), 2275–2282. <https://doi.org/10.1039/c8ta12193a>

- (40) Leijtens, T.; Eperon, G. E.; Pathak, S.; Abate, A.; Lee, M. M.; Snaith, H. J. Overcoming Ultraviolet Light Instability of Sensitized TiO<sub>2</sub> with Meso-Superstructured Organometal Tri-Halide Perovskite Solar Cells. *Nat. Commun.* **2013**, *4*, 1–8. <https://doi.org/10.1038/ncomms3885>
- (41) Khenkin, M. V.; Katz, E. A.; Visoly-fisher, I. Bias-Dependent Degradation of Various Solar Cells : Lessons for Stability of Perovskite Photovoltaics. *Energy Environ. Sci.* **2019**, *12*, 550–558. <https://doi.org/10.1039/c8ee03475c>
- (42) Luchkin, S. Y.; Akbulatov, A. F.; Frolova, L. A.; Griffin, M. P.; Dolocan, A.; Gearba, R.; Vanden Bout, D. A.; Troshin, P. A.; Stevenson, K. J. Reversible and Irreversible Electric Field Induced Morphological and Interfacial Transformations of Hybrid Lead Iodide Perovskites. *ACS Appl. Mater. Interfaces* **2017**, *9* (39), 33478–33483. <https://doi.org/10.1021/acsami.7b01960>
- (43) Akbulatov, A. F.; Frolova, L. A.; Dremova, N. N.; Zhidkov, I.; Martynenko, V. M.; Tsarev, S. A.; Luchkin, S. Y.; Kurmaev, E. Z.; Aldoshin, S. M.; Stevenson, K. J.; et al. Light or Heat: What Is Killing Lead Halide Perovskites under Solar Cell Operation Conditions? *J. Phys. Chem. Lett.* **2019**, 333–339. <https://doi.org/10.1021/acs.jpcllett.9b03308>
- (44) Dawood, R. I.; Forty, A. J.; Tubbs, M. R. The photodecomposition of lead iodide. *Proc. R. Soc. London, Ser. A* **1965**, *284*, 272–288 <https://royalsocietypublishing.org/doi/10.1098/rspa.1965.0063>
- (45) Brunetti, B.; Cavallo, C.; Cicciole, A.; Gigli, G.; Latini, A. On the Thermal and Thermodynamic (In)Stability of Methylammonium Lead Halide Perovskites. *Sci. Rep.* **2017**, *7*, 46867. <https://doi.org/10.1038/srep46867>
- (46) Latini, A.; Gigli, G.; Cicciole, A. A Study on the Nature of the Thermal Decomposition of Methylammonium Lead Iodide Perovskite, CH<sub>3</sub>NH<sub>3</sub>PbI<sub>3</sub>: An Attempt to Rationalise Contradictory Experimental Results. *Sustain. Energy Fuels* **2017**, *1* (6), 1351–1357. <https://doi.org/10.1039/c7se00114b>
- (47) Li, J.; Dong, Q.; Li, N.; Wang, L. Direct Evidence of Ion Diffusion for the Silver-Electrode- Induced Thermal Degradation of Inverted Perovskite Solar Cells. *Adv. Energy Mater.* **2017**, 1602922. <https://doi.org/10.1002/aenm.201602922>
- (48) Lee, H.; Lee, C. Analysis of Ion-Diffusion-Induced Interface Degradation in Inverted Perovskite Solar Cells via Restoration of the Ag Electrode. *Adv. Energy Mater.* **2017**, *6* (11), 1702197
- (49) Turren-Curuz, S.-H.; Hagfeldt, A.; Saliba, M. Methylammonium-Free, High-Performance, and Stable Perovskite Solar Cells on a Planar Architecture. *Science (80-. )*. **2018**, *362* (6413), 449–453 <https://doi.org/10.1126/science.aat3583>
- (50) Chen, J.; Cai, X.; Yang, D.; Song, D.; Wang, J.; Jiang, J.; Ma, A.; Lv, S.; Hu, M. Z.; Ni, C. Recent Progress in Stabilizing Hybrid Perovskites for Solar Cell Applications. *J. Power Sources* **2017**, *355*, 98–133. <https://doi.org/10.1016/j.jpowsour.2017.04.025>
- (51) Akbulatov, A. F.; Frolova, L. A.; Griffin, M. P.; Gearba, I. R.; Dolocan, A.; Bout, D. A. Vanden; Tsarev, S.; Katz, E. A.; Shestakov, A. F.; Stevenson, K. J.; et al. Effect of Electron-Transport Material on Light-Induced Degradation of Inverted Planar Junction Perovskite Solar Cells. *Adv. Energy Mater.* **2017**, *7*, 1700476. <https://doi.org/10.1002/aenm.201700476>
- (52) Rivkin, B.; Fassel, P.; Sun, Q.; Taylor, A.; Chen, Z.; Rivkin, B.; Fassel, P.; Sun, Q.; Taylor, A.; Chen, Z. Effect of Ion Migration-Induced Electrode Degradation on the Operational Stability of Perovskite Solar

Cells To Cite This Version : *ACS Omega* **2018**, *3*, 10042–10047.

<https://doi.org/10.1021/acsomega.8b01626>

- (53) Jung, H. J.; Kim, D.; Kim, S.; Park, J.; Dravid, V. P. Stability of Halide Perovskite Solar Cell Devices : In Situ Observation of Oxygen Diffusion under Biasing. *Adv. Energy Mater.* **2018**, *30*, 1802769. <https://doi.org/10.1002/adma.201802769>
- (54) Ito, S.; Tanaka, S.; Manabe, K.; Nishino, H. Effects of Surface Blocking Layer of Sb<sub>2</sub>S<sub>3</sub> on Nanocrystalline TiO<sub>2</sub> for CH<sub>3</sub>NH<sub>3</sub>PbI<sub>3</sub> Perovskite Solar Cells. *J. Phys. Chem. C* **2014**, *118*, 16995–17000
- (55) Malinauskas, T.; Tomkute-Luksiene, D.; Sens, R.; Daskeviciene, M.; Send, R.; Wonneberger, H.; Jankauskas, V.; Bruder I.; Getautis, V. Enhancing Thermal Stability and Lifetime of Solid- State Dye-Sensitized Solar Cells via Molecular Engineering of the Hole Transporting Material Spiro- OMeTAD. *Appl. Mater. interfaces* **2015**, *7*, 11107–11116. <https://doi.org/10.1021/am5090385>
- (56) Carrillo, J.; Guerrero, A.; Rahimnejad, S.; Almora, O.; Zarazua, I.; Mas-marza, E.; Bisquert, J.; Garcia-belmonte, G. Ionic Reactivity at Contacts and Aging of Methylammonium Lead Triiodide Perovskite Solar Cells. *Adv. Energy Mater.* **2016**, *6*, 1502246. <https://doi.org/10.1002/aenm.201502246>
- (57) Jena, A. K.; Numata, Y.; Ikegami, M.; Miyasaka, T. Role of Spiro-OMeTAD in Performance Deterioration of Perovskite Solar Cells at High Temperature and Reuse of the Perovskite Films to Avoid Pb-Waste. *J. Mater. Chem. A Materials Chem. A* **2018**, *6*, 2219. <https://doi.org/10.1039/C7TA07674F>
- (58) Ko, Y.; Kim, Y.; Lee, C.; Kim, Y.; Jun, Y. Investigation of Hole-Transporting Poly ( Triarylamine ) (PTAA ) on Aggregation and Charge Transport for Hysteresis-Less Scalable Planar Perovskite Solar Cells. *Appl. Mater. interfaces* **2018**, *10* (14), 11633–11641. <https://doi.org/10.1021/acсами.7b18745>
- (59) Luo, J. Xia, H. Yang, L. Chen, Z. Wan, F. Han, H. A. Malik, X. Zhu, C. J. Toward High-Efficiency, Hysteresis-Less, Stable Perovskite Solar Cells: Unusual Doping of a Hole- Transporting Material Using a Fluorine-Containing Hydrophobic Lewis Acid. *Energy Environ. Sci.* **2018**, *11* (8), 2035. <https://doi.org/10.1039/c8ee00036k>
- (60) Niu, G.; Li, W.; Li, J.; Wang, L. Progress of Interface Engineering in Perovskite Solar Cells. *Sci. China Mater.* **2016**, No. 59, 728–742. <https://doi.org/10.1007/s40843-016-5094-6>
- (61) Reza, K. M.; Mabrouk, S.; Qiao, Q. A Review on Tailoring PEDOT:PSS Layer for Improved Performance of Perovskite Solar Cells. *Proc. Nat. Res. Soc.* **2018**, *2* (02004), 1–14. DOI:10.11605/j.pnrs.201802004
- (62) Kim, J. H.; Liang, P. W.; Williams, S. T.; Cho, N.; Chueh, C. C.; Glaz, M. S.; Ginger, D. S.; Jen, A. K. Y. High-Performance and Environmentally Stable Planar Heterojunction Perovskite Solar Cells Based on a Solution-Processed Copper-Doped Nickel Oxide Hole-Transporting Layer. *Adv. Mater.* **2015**, *27* (4), 695–701. <https://doi.org/10.1002/adma.201404189>
- (63) Meng, Y.; Hu, Z.; Ai, N.; Jiang, Z.; Wang, J.; Peng, J.; Cao, Y. Improving the Stability of Bulk Heterojunction Solar Cells by Incorporating PH-Neutral PEDOT:PSS as the Hole Transport Layer. *ACS Appl. Mater. Interfaces* **2014**, *6* (7), 5122–5129. <https://doi.org/10.1021/am500336s>
- (64) Huang, D.; Goh, T.; Kong, J.; Zheng, Y.; Zhao, S.; Xu, Z.; Taylor, A. D. Perovskite Solar Cells with a DMSO-Treated PEDOT:PSS Hole Transport Layer Exhibit Higher Photovoltaic Performance and Enhanced Durability. *Nanoscale* **2017**, *9* (12), 4236–4243. <https://doi.org/10.1039/c6nr08375g>
- (65) Kim, Y. H.; Sachse, C.; MacHala, M. L.; May, C.; Müller-Meskamp, L.; Leo, K. Highly Conductive

- PEDOT:PSS Electrode with Optimized Solvent and Thermal Post-Treatment for ITO-Free Organic Solar Cells. *Adv. Funct. Mater.* **2011**, *21* (6), 1076–1081. <https://doi.org/10.1002/adfm.201002290>
- (66) Lee, D. Y.; Na, S. I.; Kim, S. S. Graphene Oxide/PEDOT:PSS Composite Hole Transport Layer for Efficient and Stable Planar Heterojunction Perovskite Solar Cells. *Nanoscale* **2016**, *8* (3), 1513–1522. <https://doi.org/10.1039/c5nr05271h>
- (67) Huang, X.; Guo, H.; Yang, J.; Wang, K.; Niu, X.; Liu, X. Moderately Reduced Graphene Oxide/PEDOT:PSS as Hole Transport Layer to Fabricate Efficient Perovskite Hybrid Solar Cells. *Org. Electron. physics, Mater. Appl.* **2016**, *39*, 288–295. <https://doi.org/10.1016/j.orgel.2016.10.013>
- (68) Huang, X.; Wang, K.; Yi, C.; Meng, T.; Gong, X. Efficient Perovskite Hybrid Solar Cells by Highly Electrical Conductive PEDOT:PSS Hole Transport Layer. *Adv. Energy Mater.* **2016**, *6* (3), 1–8. <https://doi.org/10.1002/aenm.201501773>
- (69) Irwin, M. D.; Buchholz, B. D.; Hains, A. W.; Chang, R. P.; Marks, T. J. P-Type Semiconducting Nickel Oxide as an Efficiency-Enhancing Anode Interfacial Layer in Polymer Bulk-Heterojunction Solar Cells. *Proc. Natl. Acad. Sci. U. S. A.* **2007**, *105* (8), 2783–2787. <https://doi.org/10.1073/pnas.0711990105>
- (70) Yue, S.; Liu, K.; Xu, R.; Li, M.; Azam, M.; Ren, K.; Liu, J.; Sun, Y.; Wang, Z.; Cao, D.; et al. Efficacious Engineering on Charge Extraction for Realizing Highly Efficient Perovskite Solar Cells. *Energy Environ. Sci.* **2017**, *10* (12), 2570–2578. <https://doi.org/10.1039/c7ee02685d>
- (71) Chen, W.; Liu, F.-Z.; Feng, X.-Y.; Djurišić, A. B.; Chan, W. K.; He, Z.-B. Perovskite Solar Cells: Cesium Doped NiO<sub>x</sub> as an Efficient Hole Extraction Layer for Inverted Planar Perovskite Solar Cells. *Adv. Energy Mater.* **2017**, *7* (19), 2017. <https://doi.org/10.1002/aenm.201770109>
- (72) Zhang, H.; Cheng, J.; Lin, F.; He, H.; Mao, J.; Wong, K. S.; Jen, A. K. Y.; Choy, W. C. H. Pinhole-Free and Surface-Nanostructured NiO<sub>x</sub> Film by Room-Temperature Solution Process for High-Performance Flexible Perovskite Solar Cells with Good Stability and Reproducibility. *ACS Nano* **2016**, *10* (1), 1503–1511. <https://doi.org/10.1021/acs.nano.5b07043>
- (73) Sajid, S.; Elseman, A. M.; Huang, H.; Ji, J.; Dou, S.; Jiang, H.; Liu, X.; Wei, D.; Cui, P.; Li, M. Breakthroughs in NiO<sub>x</sub>-HTMs towards Stable, Low-Cost and Efficient Perovskite Solar Cells. *Nano Energy* **2018**, *51*, 408–424. <https://doi.org/10.1016/j.nanoen.2018.06.082>
- (74) Jeng, J. Y.; Chen, K. C.; Chiang, T. Y.; Lin, P. Y.; Tsai, T. Da; Chang, Y. C.; Guo, T. F.; Chen, P.; Wen, T. C.; Hsu, Y. J. Nickel Oxide Electrode Interlayer in CH<sub>3</sub>NH<sub>3</sub>PbI<sub>3</sub> Perovskite/PCBM Planar-Heterojunction Hybrid Solar Cells. *Adv. Mater.* **2014**, *26* (24), 4107–4113. <https://doi.org/10.1002/adma.201306217>
- (75) Wang, K. C.; Shen, P. S.; Li, M. H.; Chen, S.; Lin, M. W.; Chen, P.; Guo, T. F. Low-Temperature Sputtered Nickel Oxide Compact Thin Film as Effective Electron Blocking Layer for Mesoscopic NiO/CH<sub>3</sub>NH<sub>3</sub>PbI<sub>3</sub> Perovskite Heterojunction Solar Cells. *ACS Appl. Mater. Interfaces* **2014**, *6* (15), 11851–11858. <https://doi.org/10.1021/am503610u>
- (76) Seo, S.; Jeong, S.; Park, H.; Shin, H.; Park, N. G. Atomic Layer Deposition for Efficient and Stable Perovskite Solar Cells. *Chem. Commun.* **2019**, *55* (17), 2403–2416. <https://doi.org/10.1039/c8cc09578g>
- (77) Yin, X.; Que, M.; Xing, Y.; Que, W. High Efficiency Hysteresis-Less Inverted Planar Heterojunction Perovskite Solar Cells with a Solution-Derived NiO<sub>x</sub>hole Contact Layer. *J. Mater. Chem. A* **2015**, *3* (48),

- 24495–24503. <https://doi.org/10.1039/c5ta08193a>
- (78) You, J.; Meng, L.; Song, T. Bin; Guo, T. F.; Chang, W. H.; Hong, Z.; Chen, H.; Zhou, H.; Chen, Q.; Liu, Y.; et al. Improved Air Stability of Perovskite Solar Cells via Solution-Processed Metal Oxide Transport Layers. *Nat. Nanotechnol.* **2016**, *11* (1), 75–81. <https://doi.org/10.1038/nnano.2015.230>
- (79) Zhao, Q.; Wu, R.; Zhang, Z.; Xiong, J.; He, Z.; Fan, B.; Dai, Z.; Yang, B.; Xue, X.; Cai, P.; et al. Achieving Efficient Inverted Planar Perovskite Solar Cells with Nondoped PTAA as a Hole Transport Layer. *Org. Electron. physics, Mater. Appl.* **2019**, *71*, 106–112. <https://doi.org/10.1016/j.orgel.2019.05.019>
- (80) Fan, B.; He, Z.; Xiong, J.; Zhao, Q.; Dai, Z.; Zhang, Z.; Xue, X.; Yang, J.; Yang, B.; Zhang, J. Facile Precursor Stoichiometry Engineering for Efficient Inverted Perovskite Solar Cells without Any Dopants. *Org. Electron.* **2019**, *75*, 105396. <https://doi.org/10.1016/j.orgel.2019.105396>
- (81) Tsarev, S.; Yakushchenko, I. K.; Luchkin, S. Yu.; Kuznetsov, P. M.; Timerbulatov, R. S.; Dremova, N. N.; Frolova, L. A.; Stevenson, K. J.; Troshin, P. A. A New Polytriarylamine Derivative for Dopant-Free High-Efficiency Perovskite Solar Cells. *Sustain. Energy Fuels* **2019**, *3* (10), 2627–2632. <https://doi.org/10.1039/c9se00448c>
- (82) Yakushchenko, I. K.; Kaplunov, M. G.; Eđmov, O. N.; Belov, M. Y.; Shamaev, S. N. Polytriphenylamine Derivatives as Materials for Hole Transporting Layers in Electroluminescent Devices. *Phys. Chem. Chem. Phys.* **1999**, *1*, 1783–1785. <https://doi.org/10.1039/A808613C>
- (83) Xu, C.; Liu, Z.; Lee, E. C. High-Performance Metal Oxide-Free Inverted Perovskite Solar Cells Using Poly(Bis(4-Phenyl)(2,4,6-Trimethylphenyl)Amine) as the Hole Transport Layer. *J. Mater. Chem. C* **2018**, *6* (26), 6975–6981. <https://doi.org/10.1039/C8TC02241K>
- (84) Jošt, M.; Bertram, T.; Koushik, D.; Marquez, J. A.; Verheijen, M. A.; Heinemann, M. D.; Köhnen, E.; Al-Ashouri, A.; Braunger, S.; Lang, F.; et al. 21.6%-Efficient Monolithic Perovskite/Cu(In,Ga)Se<sub>2</sub> Tandem Solar Cells with Thin Conformal Hole Transport Layers for Integration on Rough Bottom Cell Surfaces. *ACS Energy Lett.* **2019**, *4* (2), 583–590. <https://doi.org/10.1021/acsenerylett.9b00135>
- (85) Du, Y.; Xin, C.; Huang, W.; Shi, B.; Ding, Y.; Wei, C.; Zhao, Y.; Li, Y.; Zhang, X. Polymeric Surface Modification of NiO<sub>x</sub>-Based Inverted Planar Perovskite Solar Cells with Enhanced Performance. *ACS Sustain. Chem. Eng.* **2018**, *6* (12), 16806–16812. <https://doi.org/10.1021/acssuschemeng.8b04078>
- (86) Cooley, W.; Janda, R. J. Handbook of Space-Radiation Effects on Solar-Cell Power Systems. *NASA SP-3003* **1963**. ISBN-10: 1495378020
- (87) Holmes-Siedle, A. Testing Solar Cells in Space. *Nature* **1979**, *278* (5704), 503–504. <https://doi.org/10.1038/278503a0>
- (88) Anspaugh, B. E.; Downing, R. G. Radiation Effects in Silicon and Gallium Arsenide Solar Cells Using Isotropic and Normally Incident Radiation. In *Conference Record of the IEEE Photovoltaic Specialists Conference*; 1984; pp 23–30. <https://ntrs.nasa.gov/search.jsp?R=19840026722>
- (89) Wie, C. R.; Tombrello, T. A.; Vreeland, T.; Zhu, Z.; Burns, G.; Dacol, F. H.; Heights, Y. Radiation Defect-Induced Lattice Contraction of InP. *Mat. Res. Soc. Symp. Proc.* **1987**, *74* (100), 517–522. DOI: <https://doi.org/10.1557/PROC-74-517>
- (90) Cowan, V. M.; Morath, C. P.; Hubbs, J. E.; Myers, S.; Plis, E.; Krishna, S. Radiation Tolerance

- Characterization of Dual Band InAs/GaSb Type-II Strain-Layer Superlattice PBP Detectors Using 63 MeV Protons. *Appl. Phys. Lett.* **2012**, *101* (25). <https://doi.org/10.1063/1.4772543>
- (91) Messenger, S. R.; Summers, G. P.; Burke, E. A.; Walters, R. J.; Xapsos, M. A. Modeling Solar Cell Degradation in Space: A Comparison of the NRL Displacement Damage Dose and the JPL Equivalent Fluence Approaches. *Prog. Photovoltaics Res. Appl.* **2001**, *9* (2), 103–121. <https://doi.org/10.1002/pip.357>
- (92) Mbarki, M.; Sun, G. C.; Bourgoïn, J. C. Prediction of Solar Cell Degradation in Space from the Electron – Proton. *Semicond. Sci. Technol.* **2004**, *19*, 1081–1085. <https://doi.org/10.1088/0268-1242/19/9/002>
- (93) Makhm, S.; Sun, G. C.; Bourgoïn, J. C. Solar Energy Materials & Solar Cells Modelling of Solar Cell Degradation in Space. *Sol. Energy Mater. Sol. Cells* **2010**, *94* (6), 971–978. <https://doi.org/10.1016/j.solmat.2010.01.026>
- (94) Daly, E.J, Hilgers, A. Drolshagen, G. Evans, H. D. Space Environment Analysis: Experience and Trends. *ESA 1996 Symp. Environ. Model. Space-based Appl. Noordwijk, Netherlands, Sept. 18-20, 1996.* <http://adsabs.harvard.edu/full/1996ESASP.392...15D>
- (95) Waddel, R. C. Radiation Damage Shielding of Solar Cells on a Synchronous Spacecraft. *NASA Tech. note 1968.* <https://ntrs.nasa.gov/archive/nasa/casi.ntrs.nasa.gov/19680016264.pdf>
- (96) Gao X.; Yang S.; Feng Z. *High Efficiency Solar Cells*; Springer US, 2014. ISBN 978-3-319-01988-8
- (97) Kerslake, T. W.; Gustafson, E. D. On-Orbit Performance Degradation of the International Space Station P6 Photovoltaic Arrays. In *1st International Energy Conversion Engineering Conference IECEC*; 2003; pp 1–6. <https://doi.org/10.2514/6.2003-5999>
- (98) Miyazawa, Y.; Ikegami, M.; Chen, H. W.; Ohshima, T.; Imaizumi, M.; Hirose, K.; Miyasaka, T. Tolerance of Perovskite Solar Cell to High-Energy Particle Irradiations in Space Environment. *iScience* **2018**, *2*, 148–155. <https://doi.org/10.1016/j.isci.2018.03.020>
- (99) Sumita, T.; Imaizumi, M.; Matsuda, S.; Ohshima, T.; Ohi, A.; Itoh, H. Proton Radiation Analysis of Multi-Junction Space Solar Cells. *Nucl. Instruments Methods Phys. Res. Sect. B Beam Interact. with Mater. Atoms* **2003**, *206*, 448–451. [https://doi.org/10.1016/S0168-583X\(03\)00791-2](https://doi.org/10.1016/S0168-583X(03)00791-2)
- (100) Lang, F.; Nickel, N. H.; Bundesmann, J.; Seidel, S.; Denker, A.; Albrecht, S.; Brus, V. V.; Rappich, J.; Rech, B.; Landi, G.; et al. Radiation Hardness and Self-Healing of Perovskite Solar Cells. *Adv. Mater.* **2016**, *28* (39), 8726–8731. <https://doi.org/10.1002/adma.201603326>
- (101) Lang, F.; Jošt, M.; Bundesmann, J.; Denker, A.; Albrecht, S.; Landi, G.; Neitzert, H. C.; Rappich, J.; Nickel, N. H. Efficient Minority Carrier Detrapping Mediating the Radiation Hardness of Triple-Cation Perovskite Solar Cells under Proton Irradiation. *Energy Environ. Sci.* **2019**, *12* (5), 1634–1647. <https://doi.org/10.1039/c9ee00077a>
- (102) Yang, S.; Xu, Z.; Xue, S.; Kandlakunta, P.; Cao, L.; Huang, J. Organohalide Lead Perovskites: More Stable than Glass under Gamma-Ray Radiation. *Adv. Mater.* **2019**, *31* (4), 1–7. <https://doi.org/10.1002/adma.201805547>
- (103) Bartusiak, M. F.; Becher, J. Proton-Induced Coloring of Multicomponent Glasses. *Appl. Opt.* **1979**, *18* (19), 3342. <https://doi.org/10.1364/ao.18.003342>
- (104) Yang, K.; Huang, K.; Li, X.; Zheng, S.; Hou, P.; Wang, J.; Guo, H.; Song, H.; Li, B.; Li, H.; et al. Radiation Tolerance of Perovskite Solar Cells under Gamma Ray. *Org. Electron. physics, Mater. Appl.*

- 2019**, *71*, 79–84. <https://doi.org/10.1016/j.orgel.2019.05.008>
- (105) Kim, H.; Seo, J.; Park, N. Material and Device Stability in Perovskite Solar Cells. *Chem.Sus.Chem.* **2016**, *9*, 2528–2540. <https://doi.org/10.1002/cssc.201600915>
- (106) Ruess, R.; Benfer, F.; Bçcher, F.; Stumpp, M.; Schlettwein, D. Stabilization of Organic – Inorganic Perovskite Layers by Partial Substitution of Iodide by Bromide in Methylammonium Lead Iodide. *ChemPhysChem* **2016**, *17* (10), 1505–1511. <https://doi.org/10.1002/cphc.201501168>
- (107) Reese, M. O.; Gevorgyan, S. A.; Jørgensen, M.; Bundgaard, E.; Kurtz, S. R.; Ginley, S.; Olson, D. C.; Lloyd, M. T.; Morvillo, P.; Katz, E. A.; et al. Solar Energy Materials & Solar Cells Consensus Stability Testing Protocols for Organic Photovoltaic Materials and Devices. **2011**, *95*, 1253–1267. <https://doi.org/10.1016/j.solmat.2011.01.036>
- (108) Khenkin, M. V.; Katz, E. A.; Abate, A.; Bardizza, G.; Berry, J. J.; Brabec, C.; Brunetti, F.; Bulović, V.; Burlingame, Q.; Carlo, A. Di; et al. Consensus Statement for Stability Assessment and Reporting for Perovskite Photovoltaics Based on ISOS Procedures. *Nat. Energy* **2020**, *5* (January). <https://doi.org/10.1038/s41560-019-0529-5>
- (109) Li, X.; Bi, D.; Yi, C.; Décoppet, J.-D.; Luo, J.; Zakeeruddin, S. M.; Hagfeldt, A.; Grätzel, M. A Vacuum Flash-Assisted Solution Process for High-Efficiency Large-Area Perovskite Solar Cells. *Science (80-. )*. **2016**, *353* (6294), 58–62. <https://doi.org/10.1126/science.aaf8060>
- (110) Malinkiewicz, O.; Yella, A.; Lee, Y. H.; Graetzel, M.; Nazeeruddin, M. K.; Bolink, H. J. Perovskite Solar Cells Employing Organic Charge-Transport Layers. *Nat.photonics* **2014**, *8*, 128–132. <https://doi.org/10.1038/nphoton.2013.341>
- (111) Liang, P.; Chueh, C.; Williams, S. T.; Jen, A. K. Roles of Fullerene-Based Interlayers in Enhancing the Performance of Organometal Perovskite Thin-Film Solar Cells. *Adv. Energy Mater.* **2015**, *5*, 1402321. <https://doi.org/10.1002/aenm.201402321>
- (112) Park, S.; Wang, D. H. Alignment of Cascaded Band-Gap via PCBM / ZnO Hybrid Interlayers for Efficient Perovskite Photovoltaic Cells. *Macromol. Res.* **2018**, *26*, 1598–5032. <https://doi.org/10.1007/s13233-018-6086-0>
- (113) Li, S.; Liu, W.; Li, C. Z.; Liu, F.; Zhang, Y.; Shi, M.; Chen, H.; Russell, T. P. A Simple Perylene Diimide Derivative with a Highly Twisted Geometry as an Electron Acceptor for Efficient Organic Solar Cells. *J. Mater. Chem. A* **2016**, *4* (27), 10659–10665. <https://doi.org/10.1039/c6ta04232e>
- (114) Zhao, J.; Li, Y.; Lin, H.; Liu, Y.; Jiang, K.; Mu, C.; Ma, Lai, L.; Hu, H.; Yu, D.; Yan, H. High-Efficiency Non-Fullerene Organic Solar Cells Enabled by a Difluorobenzothiadiazole-Based Donor Polymer Combined with a Properly Matched Small Molecule Acceptor. *Energy Environ. Sci.* **2015**, *8*, 520–525. <https://doi.org/10.1039/C4EE02990A>
- (115) Rundel, K.; Maniam, S.; Deshmukh, K.; Gann, E.; McNeill, C. R. Naphthalene Diimide-Based Small Molecule Acceptors for Organic Solar Cells †. *J. Mater. Chem. A* **2017**, *5*, 12266–12277. <https://doi.org/10.1039/C7TA02749D>
- (116) Liu, Y.; Zhang, L.; Lee, H.; Wang, H. W.; Santala, A.; Liu, F.; Diao, Y.; Briseno, A. L.; Russell, T. P. NDI-Based Small Molecule as Promising Nonfullerene Acceptor for Solution-Processed Organic Photovoltaics. *Adv. Energy Mater.* **2015**, *5*, 2–9. <https://doi.org/10.1002/aenm.201500195>

- (117) Jiang, J.; Jin, Z.; Lei, J.; Wang, Q.; Zhang, J. . G. F. . L. S. ITIC Surface Modification to Achieve Synergistic Electron Transport Layer Enhancement for Planar-Type Perovskite Solar Cells with Efficiency Exceeding 20%. *J. Mater. Chem. A* **2017**, *5*, 9514–9522. <https://doi.org/10.1039/C7TA01636K>
- (118) Chiang, C.; Wu, C. Film Grain-Size Related Long-Term Stability of Inverted Perovskite Solar Cells. *Chem.Sus.Chem.* **2016**, *9*, 2666–2672. <https://doi.org/10.1002/cssc.201600887>
- (119) Azat F. Akbulatov, Lyubov A. Frolova, Sergey A. Tsarev, Ivan Zhidkov, Sergey Yu. Luchkin, Ernst Z. Kurmaev, Keith J. Stevenson, S. M. A. and P. A. T. Film Deposition Techniques Impact Defect Density and Photostability of MAPbI3 Perovskite Films. *Submitted*.
- (120) Gurina, G. I.; Evtushenko, V. D.; Kobyakov A. Y.; Koshkin, V. M. Intercalation and Photolysis of Pbl 2 Crystals. *Theor. Exp. Chem* **1986**, *21* (6), 718–719. <https://doi.org/10.1007/BF00945156>
- (121) Ceratti, D. R.; Rakita, Y.; Cremonesi, L.; Tenne, R.; Kalchenko, V.; Elbaum, M.; Oron, D.; Potenza, M. A. C.; Hodes, G.; Cahen, D. Self-Healing Inside APbBr3Halide Perovskite Crystals. *Adv. Mater.* **2018**, *30*, 1706273. <https://doi.org/10.1002/adma.201706273>
- (122) Niu, T.; Lu, J.; Munir, R.; Li, J.; Barrit, D.; Zhang, X.; Hu, H.; Yang, Z.; Amassian, A.; Zhao, K.; et al. Stable High-Performance Perovskite Solar Cells via Grain Boundary Passivation. *Adv. Mater.* **2018**, *30* (16), 1–11. <https://doi.org/10.1002/adma.201706576>
- (123) Frolova, L. A.; Piven, N. P.; Susarova, D. K.; Akkuratov, A. V; Babenko, S. D.; Troshin, P. A. ESR Spectroscopy for Monitoring the Photochemical and Thermal Degradation of Conjugated Polymers Used as Electron Donor Materials in Organic Bulk Heterojunction Solar Cells. *Chem. Commun.* **2015**, *51*, 2242–2244. <https://doi.org/10.1039/C4CC08146C>
- (124) Koushik, D.; Verhees, W. J. H.; Kuang, Y.; Veenstra, S.; Zhang, D.; Verheijen, M. A.; Creatore, M.; Schropp, R. E. I. High-Efficiency Humidity-Stable Planar Perovskite Solar Cells Based on Atomic Layer Architecture. *Energy Environ. Sci.* **2017**, *10*, 91–100. <https://doi.org/10.1039/c6ee02687g>
- (125) Hoke, E. T.; Slotcavage, D. J.; Dohner, E. R.; Bowring, A. R.; Karunadasa, H. I.; McGehee, M. D. Reversible Photo-Induced Trap Formation in Mixed-Halide Hybrid Perovskites for Photovoltaics. *Chem. Sci.* **2015**, *6*, 613–617. <https://doi.org/10.1039/c4sc03141e>
- (126) Yang, X.; Yan, X.; Wang, W.; Zhu, X.; Li, H.; Ma, W.; Sheng, C. Light Induced Metastable Modification of Optical Properties in CH3 NH3PbI(3-x)Brx Perovskite Films : Two-Step Mechanism. *Org. Electron.* **2016**, *34*, 79–83. <https://doi.org/10.1016/j.orgel.2016.04.02>
- (127) Brennan, M. C.; Draguta, S.; Kamat, P. V; Kuno, M. Light-Induced Anion Phase Segregation in Mixed Halide Perovskites. *ACS Energy Lett.* **2017**, *3*, 204–213. <https://doi.org/10.1021/acsenergylett.7b01151>
- (128) Guo, D.; Garmaroudi, Z. A.; Abdi-jalebi, M.; Stranks, S. D.; Savenije, T. J. Reversible Removal of Intermixed Shallow. *ACS Energy Lett.* **2019**, *4*, 2360–2367. <https://doi.org/10.1021/acsenergylett.9b01726>
- (129) Westbrook, R. J. E.; Sanchez-Molina, D. I.; Manuel Marin-Beloqui, D. J.; Bronstein, D. H.; Haque, D. S. A. Effect of Interfacial Energetics on Charge Transfer from Lead Halide Perovskite to Organic Hole Conductors. *J. Phys. Chem. C* **2018**, *122* (2), 1326–1332. <https://doi.org/10.1021/acs.jpcc.7b09178>
- (130) Misra, R. K.; Aharon, S.; Li, B.; Mogilyansky, D.; Visoly-fisher, I.; Etgar, L.; Katz, E. A.; Ram, G. Temperature- and Component-Dependent Degradation of 2 Perovskite Photovoltaic Materials under Concentrated Sunlight 1. *J. Phys. Chem. Lett.* **2014**, *6*, 326–330. <https://doi.org/10.1021/jz502642b>

- (131) Brus, V. V.; Lang, F.; Bundesmann, J.; Seidel, S.; Denker, A.; Rech, B.; Landi, G.; Neitzert, H. C.; Rappich, J.; Nickel, N. H. Defect Dynamics in Proton Irradiated CH<sub>3</sub>NH<sub>3</sub>PbI<sub>3</sub> Perovskite Solar Cells. *Adv. Electron. Mater.* **2017**, *3* (2). <https://doi.org/10.1002/aelm.201600438>
- (132) Barker, A. J.; Sadhanala, A.; Deschler, F.; Gandini, M.; Senanayak, S. P.; Pearce, P. M.; Mosconi, E.; Pearson, A. J.; Wu, Y.; Ram, A.; et al. Defect-Assisted Photoinduced Halide Segregation in Mixed-Halide Perovskite Thin Films. *ACS Energy Lett.* **2017**, *2* (6), 1416–1424. <https://doi.org/10.1021/acsenergylett.7b00282>
- (133) Unger, E. L.; Kegelmann, L.; Suchan, K.; Sörell, D.; Korte, L.; Albrecht, S. Roadmap and Roadblocks for the Band Gap Tunability of Metal Halide Perovskites. *J. Mater. Chem. A* **2017**, *5* (23), 11401–11409. <https://doi.org/10.1039/c7ta00404d>
- (134) Chiba, T.; Kido, J. Lead Halide Perovskite Quantum Dots for Light-Emitting Devices. *J. Mater. Chem. C* **2018**, *6* (44), 11868–11877. <https://doi.org/10.1039/c8tc03561j>
- (135) Wang, H. C.; Bao, Z.; Tsai, H. Y.; Tang, A. C.; Liu, R. S. Perovskite Quantum Dots and Their Application in Light-Emitting Diodes. *Small* **2018**, *14* (1), 1–23. <https://doi.org/10.1002/sml.201702433>
- (136) Heumueller, T.; Burke, T. M.; Mateker, W. R.; Sachs-Quintana, I. T.; Vandewal, K.; Brabec, C. J.; McGehee, M. D. Disorder-Induced Open-Circuit Voltage Losses in Organic Solar Cells during Photoinduced Burn-In. *Adv. Energy Mater.* **2015**, *5* (14), 1–8. <https://doi.org/10.1002/aenm.201500111>
- (137) Cowan, S. R.; Leong, W. L.; Banerji, N.; Dennler, G.; Heeger, A. J. Identifying a Threshold Impurity Level for Organic Solar Cells: Enhanced First-Order Recombination via Well-Defined PC84BM Traps in Organic Bulk Heterojunction Solar Cells. *Adv. Funct. Mater.* **2011**, *21* (16), 3083–3092. <https://doi.org/10.1002/adfm.201100514>
- (138) Braun, T. Nuclear and Radiation Chemical Approaches to Fullerene Science; *Springer US: Dordrecht*, **2000**. ISBN 978-94-015-9419-6
- (139) Schulz, P.; Tjepelt, J. O.; Christians, J. A.; Levine, I.; Edri, E.; Sanehira, E. M.; Hodes, G.; Cahen, D.; Kahn, A. High-Work-Function Molybdenum Oxide Hole Extraction Contacts in Hybrid Organic-Inorganic Perovskite Solar Cells. *ACS Appl. Mater. Interfaces* **2016**, *8* (46), 31491–31499. <https://doi.org/10.1021/acsami.6b10898>
- (140) Náfrádi, G.; Horváth, E.; Kollár, M.; Horváth, A.; Andričević, P.; Sienkiewicz, A.; Forró, L.; Náfrádi, B. Radiation Detection and Energy Conversion in Nuclear Reactor Environments by Hybrid Photovoltaic Perovskites. *Energy Convers. Manag.* **2020**, *205*, 112423. <https://doi.org/10.1016/j.enconman.2019.112423>
- (141) Li, W.; Liu, J.; Bai, F. Q.; Zhang, H. X.; Prezhdo, O. V. Hole Trapping by Iodine Interstitial Defects Decreases Free Carrier Losses in Perovskite Solar Cells: A Time-Domain Ab Initio Study. *ACS Energy Lett.* **2017**, *2* (6), 1270–1278. <https://doi.org/10.1021/acsenergylett.7b00183>
- (142) Walsh, A.; Scanlon, D. O.; Chen, S.; Gong, X. G.; Wei, S. H. Self-Regulation Mechanism for Charged Point Defects in Hybrid Halide Perovskites. *Angew. Chemie - Int. Ed.* **2015**, *54* (6), 1791–1794. <https://doi.org/10.1002/anie.201409740>
- (143) Yang, J. H.; Yin, W. J.; Park, J. S.; Wei, S. H. Self-Regulation of Charged Defect Compensation and Formation Energy Pinning in Semiconductors. *Sci. Rep.* **2015**, *5*, 1–10. <https://doi.org/10.1038/srep16977>

- (144) Peng, J.; Wu, Y.; Ye, W.; Jacobs, D. A.; Shen, H.; Fu, X.; Wan, Y.; Duong, T.; Wu, N.; Barugkin, C.; et al. Interface Passivation Using Ultrathin Polymer-Fullerene Films for High-Efficiency Perovskite Solar Cells with Negligible Hysteresis. *Energy Environ. Sci.* **2017**, *10* (8), 1792–1800.  
<https://doi.org/10.1039/c7ee01096f>
- (145) Huang, K.; Yang, K.; Li, H.; Zheng, S.; Wang, J.; Guo, H.; Peng, Y.; Zhong, X.; Yang, J. Gamma-Ray Radiation on Flexible Perovskite Solar Cells (Unpublished). *ACS Appl. Energy Mater.* **2020**.